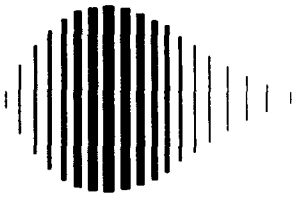

**NATIONAL CENTER FOR EARTHQUAKE ENGINEERING RESEARCH**

State University of New York at Buffalo

# Shake Table Test of a 1/8 Scale Three-Story Lightly Reinforced Concrete Building

by

A. G. El-Attar, R. N. White and P. Gergely

Department of Structural Engineering
School of Civil and Environmental Engineering
Cornell University
Ithaca, New York 14853-3501

Technical Report NCEER-91-0018

February 28, 1991

This research was conducted at Cornell University and was partially supported by the National Science Foundation under Grant No. ECE 86-07591.

# NOTICE

This report was prepared by Cornell University as a result of research sponsored by the National Center for Earthquake Engineering Research (NCEER). Neither NCEER, associates of NCEER, its sponsors, Cornell University, nor any person acting on their behalf:

a. makes any warranty, express or implied, with respect to the use of any information, apparatus, method, or process disclosed in this report or that such use may not infringe upon privately owned rights; or

b. assumes any liabilities of whatsoever kind with respect to the use of, or for damages resulting from the use of, any information, apparatus, method or process disclosed in this report.

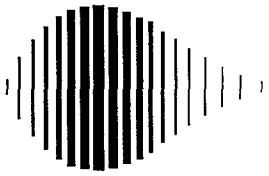

# Shake Table Test of a 1/8 Scale Three-Story Lightly Reinforced Concrete Building

by

A.G. El-Attar[1], R.N. White[2] and P. Gergely[3]

February 28, 1991

Technical Report NCEER-91-0018

NCEER Project Number 89-1001B

NSF Master Contract Number ECE 86-07591

1 Instructor, Cairo University, Cairo, Egypt; former Graduate Research Assistant, School of Civil and Environmental Engineering, Cornell University
2 James A. Friend Family Professor, School of Civil and Environmental Engineering, Cornell University
3 Professor, School of Civil and Environmental Engineering, Cornell University

NATIONAL CENTER FOR EARTHQUAKE ENGINEERING RESEARCH
State University of New York at Buffalo
Red Jacket Quadrangle, Buffalo, NY 14261

## PREFACE

The National Center for Earthquake Engineering Research (NCEER) is devoted to the expansion and dissemination of knowledge about earthquakes, the improvement of earthquake-resistant design, and the implementation of seismic hazard mitigation procedures to minimize loss of lives and property. The emphasis is on structures and lifelines that are found in zones of moderate to high seismicity throughout the United States.

NCEER's research is being carried out in an integrated and coordinated manner following a structured program. The current research program comprises four main areas:

- Existing and New Structures
- Secondary and Protective Systems
- Lifeline Systems
- Disaster Research and Planning

This technical report pertains to Program 1, Existing and New Structures, and more specifically to system response investigations.

The long term goal of research in Existing and New Structures is to develop seismic hazard mitigation procedures through rational probabilistic risk assessment for damage or collapse of structures, mainly existing buildings, in regions of moderate to high seismicity. The work relies on improved definitions of seismicity and site response, experimental and analytical evaluations of systems response, and more accurate assessment of risk factors. This technology will be incorporated in expert systems tools and improved code formats for existing and new structures. Methods of retrofit will also be developed. When this work is completed, it should be possible to characterize and quantify societal impact of seismic risk in various geographical regions and large municipalities. Toward this goal, the program has been divided into five components, as shown in the figure below:

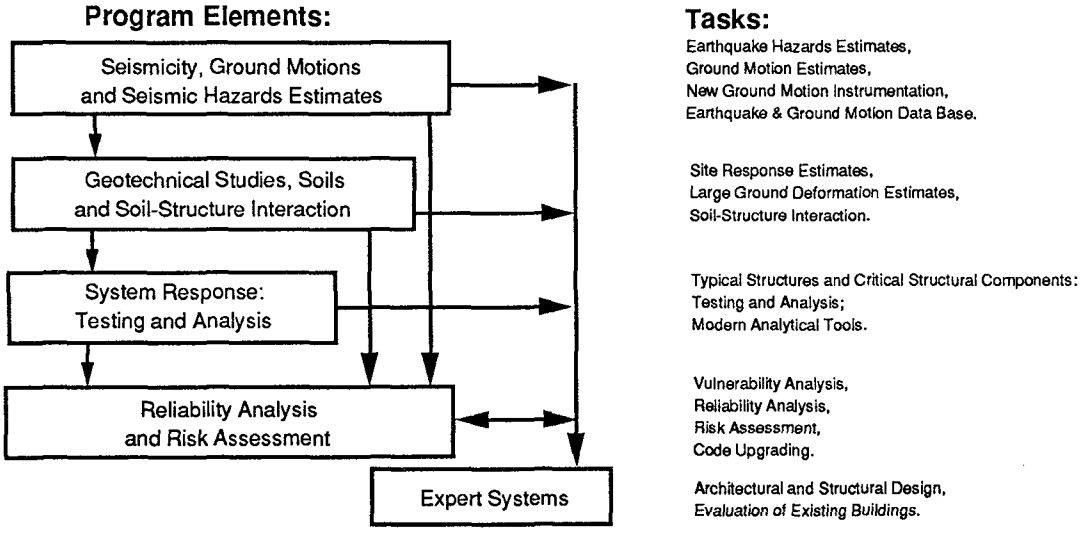

System response investigations constitute one of the important areas of research in Existing and New Structures. Current research activities include the following:

1. Testing and analysis of lightly reinforced concrete structures, and other structural components common in the eastern United States such as semi-rigid connections and flexible diaphragms.
2. Development of modern, dynamic analysis tools.
3. Investigation of innovative computing techniques that include the use of interactive computer graphics, advanced engineering workstations and supercomputing.

The ultimate goal of projects in this area is to provide an estimate of the seismic hazard of existing buildings which were not designed for earthquakes and to provide information on typical weak structural systems, such as lightly reinforced concrete elements and steel frames with semi-rigid connections. An additional goal of these projects is the development of modern analytical tools for the nonlinear dynamic analysis of complex structures.

*The greatest effort in the Existing and New Structures area concentrated on the evaluation and response-prediction of existing "weak" buildings that are common in regions of low seismicity. Most of these lightly reinforced concrete buildings and steel buildings with semi-rigid connections were not designed for seismic forces and many not even for wind loading. The coordinated research program on concrete buildings has included full-scale tests of frame joint regions, flat-plate structures, and shake-table tests of frames at various scales. These tests were done at Cornell University, University at Buffalo, and Rice University. One of the main goals of this effort has been the development of analytical tools for the complete nonlinear analysis of such structures so that realistic estimates of their expected response can be made to aid practicing engineers and researchers in the risk/reliability research area.*

*This report summarizes a series of shaking-table tests on a three-story concrete frame structure. The structure is very flexible and reached 2.63% story drifts during the Taft earthquake scaled to 0.35g maximum ground acceleration. The P-delta effect increased column shears by as much as 27%. The column axial forces had a strong effect on the relative column shear forces. The structure collapsed during ground motion scaled to 0.8g acceleration.*

## ABSTRACT

A 1/8 scale 3-story one bay by three-bay office building was tested on the Cornell University shake table. The structure was designed solely for gravity loads without regard to any kind of lateral loads (wind or earthquakes). The reinforcement details were based on typical reinforced concrete frame structures constructed in the Central and Eastern United States since the early 1900's, and characterized by (a) low reinforcement ratio in the columns, (b) discontinuous positive moment beam reinforcement at the columns, (c) little or no joint confinement, and (d) lap splices located immediately above the floor level. The model was tested using the time-compressed Taft 1952 S69E at different amplitudes. Auxiliary tests such as static loading test and free-vibration test were performed before and after each seismic test to study the changes in the model building properties.

Test results indicated that this type of building will experience very large deformations associated with a considerable stiffness degradation during a moderate earthquake. A significant P-$\Delta$ effect was recorded during all seismic tests due to the high flexibility of lightly reinforced concrete structures. Although the non-seismic reinforcement details may form a potential source of damage for lightly reinforced concrete buildings, it was found experimentally that they are not enough to cause a complete failure mechanism. The model failure occurred outside the joint region, indicating that the lack of joint confinement was the primary source of damage. Also, the location and details of the column lap splices did not cause a serious problem in the model test.

Both experimental and analytical results indicated that the inclusion of the slab contributions to the beam flexural strength is a vital step in the assessment of the performance of lightly reinforced concrete structures during earthquakes since it has the potential of altering the relatively ductile strong column-weak beam mechanism to the more brittle soft-story mechanism.

## ACKNOWLEDGEMENTS

The authors would like to express their appreciation to the assistance provided by Tim Bond, Manager of the George Winter Laboratory, and extend thanks to Jack Powers for manufacturing and instrumenting the load cells. The effort of Paul Jones and Glenn Darling of the Civil Engineering department machine shop throughout this work is also deeply appreciated.

Thanks are also extended to the many Civil Engineering students who helped with the experimental work. In particular, the authors acknowledge Adam Hoffman, Rebecca Frein, and William Druc for their invaluable help.

## TABLE OF CONTENTS

## LIST OF ILLUSTRATIONS

## LIST OF TABLES

# CHAPTER 1

# INTRODUCTION

## 1.1 Introduction

Recent seismic studies and the historical records indicate that damaging earthquakes can occur in the Central and Eastern United States where thousands of reinforced concrete buildings constructed since early 1900's were designed and detailed to resist primarily gravity loads. This fact was addressed in the 1982 NRC report [13] stating that, "In future earthquakes, the major causes of injury and loss of life will almost certainly be the collapse of older structures that were designed and built before building codes were developed". Experimental evidence is indeed required for a better understanding of the behavior of this type of building detail and for the development of more reliable analytical tools to predict their damage potential. Based on both experimental and analytical information, risk assessment can be conducted for lightly reinforced concrete buildings existing in different seismic zones.

The study presented here is part of a comprehensive research effort conducted by the National Center of Earthquake Engineering (NCEER) on the damage assessment and performance evaluation of non-seismically detailed buildings during earthquakes. The current work presents results of a 1/8 scale lightly reinforced

concrete 3-story office building tested on the shake table of Cornell University . The building was designed and detailed to reflect the common design and practice features of the Central and Eastern United States during the period of 1950 to 1970. Test results are evaluated and compared to the numerical results to investigate the reliability of available analytical tools in predicting the response of this kind of building.

## 1.2 Objectives and scope

### 1.2.1 Objectives

The major objectives of the current research work include:

1. Identify typical reinforcement details of lightly reinforced concrete buildings constructed in the Central and Eastern United States prior to the 1970's.

2. Investigate the performance of lightly reinforced concrete buildings during earthquakes through a program of testing small-scale structures on the shake table of Cornell University .

3. Evaluate the reliability of one of the recently developed analytical modeling techniques to predict the response of these buildings.

### 1.2.2 Scope

The overall plan of the current research is presented in figure 1.1. This report focuses only on the last two phases of the research work, where a 1/8 scale 3-story buildings was tested on the shake table, and numerical analysis was performed to compare the experimental and the analytical results.

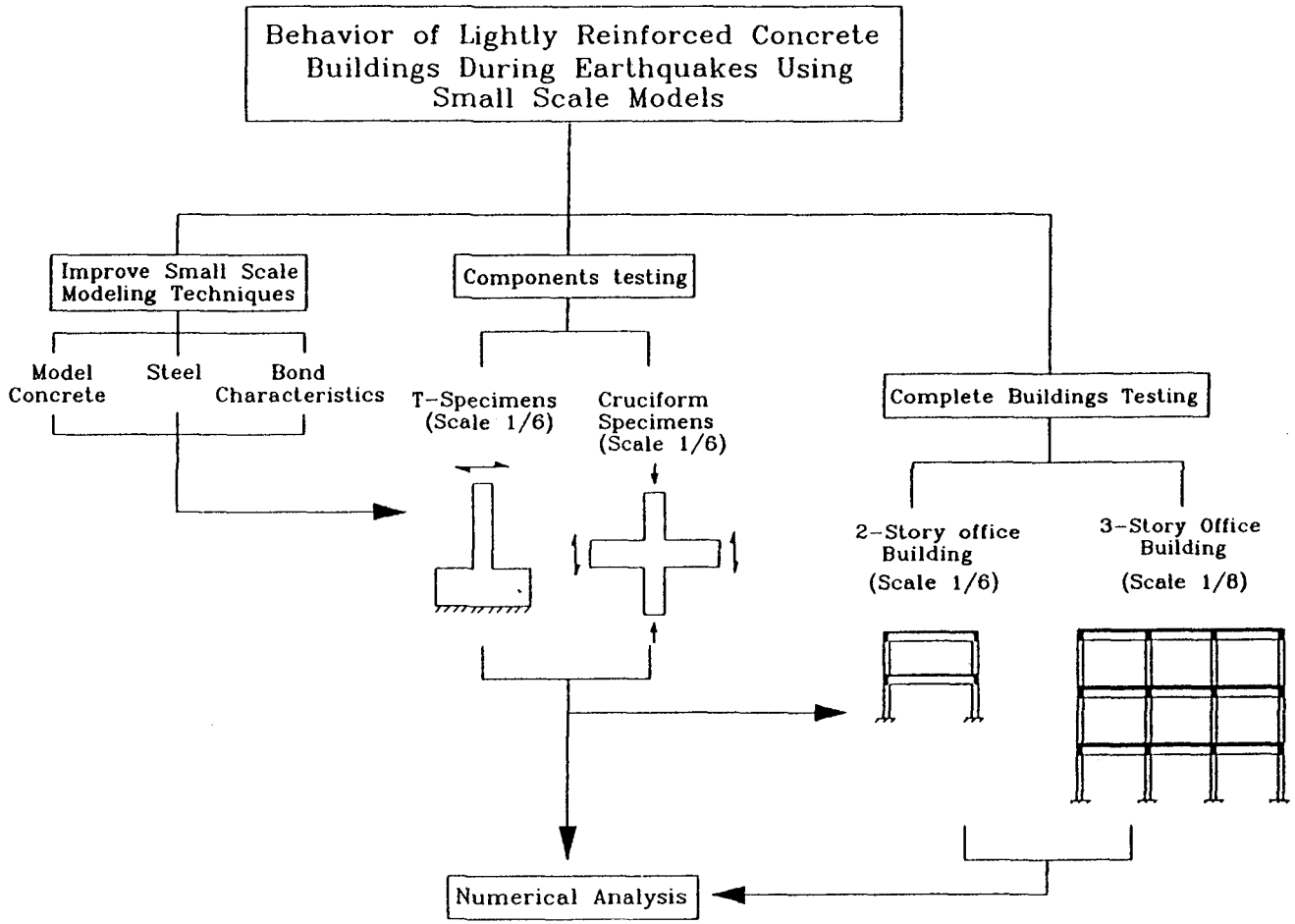


Figure 1.1: Flow Chart of The Research Program.

Chapter 2 describes the experimental program. A full description of the test structure is given in section 2.1 including design, material properties, reinforcement details, and fabrication techniques. The testing procedures, including the static test, free vibration test, and the simulated seismic test are presented in section 2.2.

Chapter 3 includes a summary of the 3-story building test results. The discussion of the test results includes many topics regarding both the overall building response and specific member performance during seismic tests.

In Chapter 4, a summary of the analytical model used in the program IDARC is introduced, followed by a summary of the numerical analysis results of the model building. Comparison between the experimental and the analytical results is also provided in this chapter.

Chapter 5 includes an evaluation of lightly reinforced concrete building performance during earthquakes. Special attention is paid to the impact of the design philosophy of those structures on their seismic behavior. Experimental evidence is provided when appropriate to support the evaluation.

Chapter 6 contains a summary, the conclusions of the present work, and recommendations for future research.

Appendix A introduces the design of the 3-story office building modeled in the current study. Appendix B describes the load-cells used for the 3-story model column instrumentation. This includes mechanical and electronic design, and fabrication and installation of the load cells.

# CHAPTER 2

# EXPERIMENTAL PROGRAM

The first part of this chapter describes the test structure, its design and fabrication, mechanical properties, materials, and the load set-up and instrumentation. The second part deals with the test procedure including static, free-vibration, and simulated-seismic tests.

## 2.1 Test structure

The test structure was a 1/8 scale, 3-story, one-bay by three-bay office building. The building was designed and detailed to resist gravity loads only, with no consideration to any kind of lateral forces due to wind or earthquakes. No walls or infills were included in the selected building. Details of the prototype building design are provided in appendix A of this report.

### 2.1.1 3-Story building model

#### Model design

The general layout of the 3-story building is shown in figure 2.1. The model structure represented only one bay with two side quarter bays of the prototype structure (an inflection point to inflection point cut). The model was designed according to the similitude requirements provided in table 2.1. Geometric dimensions of the

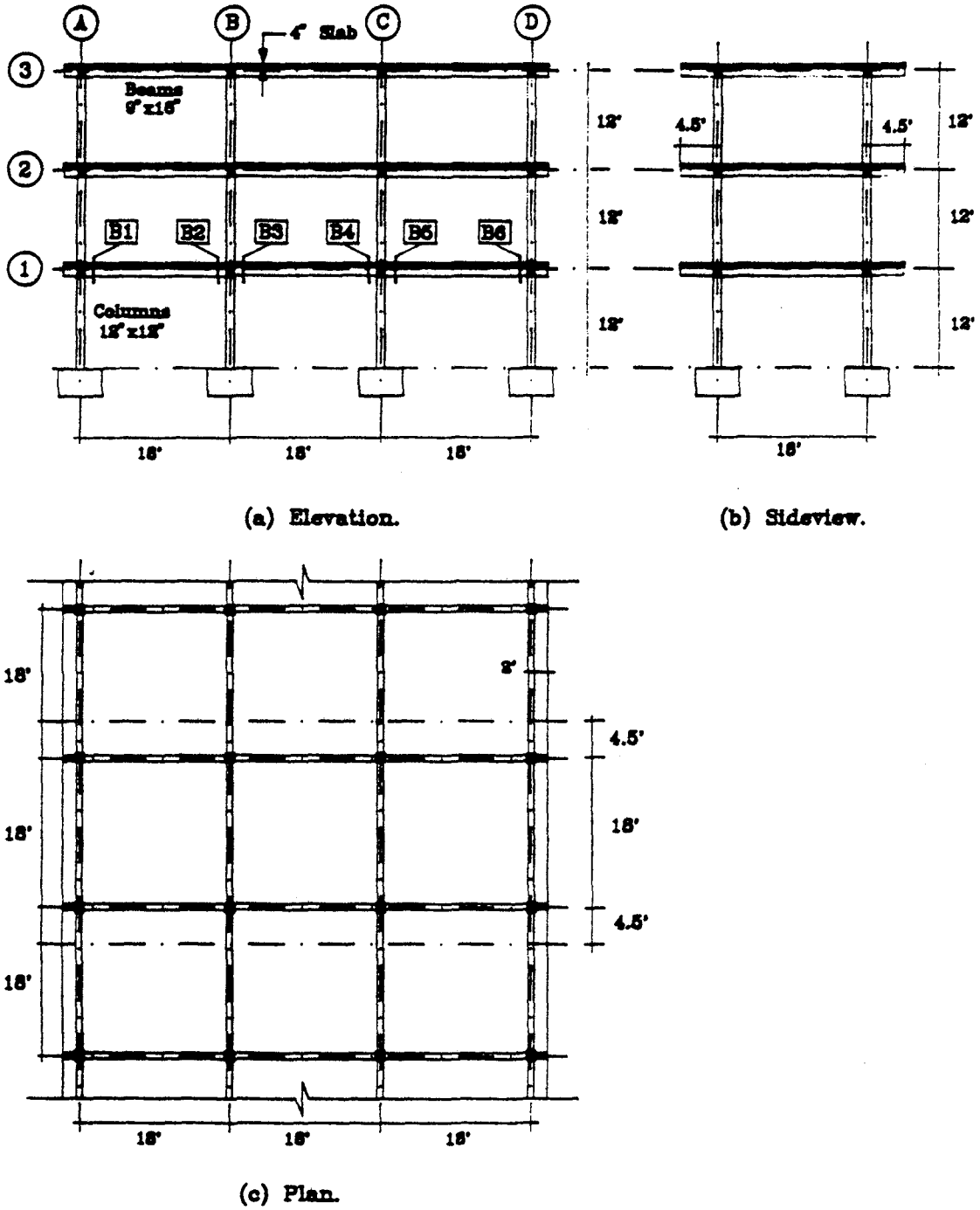


Figure 2.1: General Layout of The 3-Story Building.

Table 2.1: Similitude Requirements For The 3-Story Model Building

| Quantity | Symbol | Dimension | Scale Factor | Used Scale Factor |
|---|---|---|---|---|
| Linear dimension | $L$ | $L$ | $S_L$ | 8 |
| Displacement | $\delta$ | $L$ | $S_L$ | 8 |
| Angular displacement | $\theta$ | – | $S_\theta$ | 1 |
| Time | $T$ | $T$ | $\sqrt{S_t}$ | 2.83 |
| Frequency | $f$ | $T^{-1}$ | $\frac{1}{S_t}$ | 0.35 |
| Velocity | $V$ | $LT^{-1}$ | $\frac{S_L}{S_t}$ | 2.83 |
| Acceleration | $a$ | $LT^{-1}$ | $\frac{S_L}{S_t^2}$ | 1 |
| Energy | $E$ | $FL$ | $S_L^3$ | 512 |
| Area of reinforcement | $A_r$ | $L^2$ | $S_L^2$ | 64 |
| Concrete stress | $f_c$ | $FL^{-2}$ | $S_f$ | 1 |
| Steel stress | $f_s$ | $FL^{-2}$ | $S_f$ | 1 |
| Concrete strain | $\epsilon_{cu}$ | – | $S_\epsilon$ | 1 |
| Steel strain | $\epsilon_s$ | – | $S_\epsilon$ | 1 |
| Concrete modulus | $E_c$ | $FL^{-2}$ | $S_f$ | 1 |
| Steel modulus | $E_s$ | $FL^{-2}$ | $S_f$ | 1 |
| Mass density | $\rho$ | $FL^{-3}$ | $\frac{1}{S_L}$ | – |
| Concentrated load | $Q$ | $F$ | $S_L^2$ | 64 |
| Line Load | $W$ | $FL^{-1}$ | $S_L$ | 8 |
| Pressure | $q$ | $FL^{-2}$ | $S_f$ | 1 |
| Moment | $M$ | $FL$ | $S_L^3$ | 512 |

model were obtained by directly scaling the prototype dimension by the scale factor $S_l$= 8.

The model reinforcement areas were obtained according to the similitude requirements (table 2.1) as follows:

$$A_m = \frac{A_p}{S_l^2} = \frac{A_p}{64} = 0.0156 A_p \tag{2.1}$$

Where $A_m$ = tensile stress area of the model reinforcement, $A_p$ = prototype reinforcement area, and $S_l$ = length scale factor.

After the selection of the model bar sizes, the yield stress of each bar size was modified to account for any differences between the required and the selected bar areas in order to correctly scale the bar yield force. The model reinforcement yield stress then became:

$$f_{ym} = f_{ym_{calculated}} \times \frac{A_{m_{required}}}{A_{m_{chosen}}} \tag{2.2}$$

Where $f_{ym}$ = yield stress of the model reinforcement.

The heat-treatment process was then carried out separately for each bar size to achieve the required yield stress according to equation (2.2).

## Model Materials

(a) Model concrete:

The microconcrete used in the 3-story building model model was based on the results of a previous study conducted at Cornell University on improving the modeling techniques of small scale concrete structures [9]. In this study special atten-

tion was paid to producing a new microconcrete with high stiffness and low tensile strength. This microconcrete mix was slightly modified to produce a lower compressive strength $f_c^{'}$ between 3.5 and 4.0 ksi (commonly used prior to the 1970's), and to provide a highly workable mix (to suit the small scale model). Only the main properties of the selected microconcrete will be presented in the following paragraphs.

The microconcrete mix ratio was ( Water : Cement : Model sand (Sm): Model aggregates (Am)= 0.95 : 1 : 3.6 : 2.4 ); where model sand was defined as particles that pass a #8 sieve and were retained on #200 sieve, and model aggregates were defined as particles that pass #6 sieve and were retained on #8 sieve. Figure 2.2 illustrates the grading curve for the aggregates. Type III cement was used since it has more rapid curing than type I cement. Superplastisizer EUCON 537 was added by the ratio of 1% of the cement weight to increase the mix workability. The stress-strain curve of the microconcrete is shown in figure 2.3.

(b) Model reinforcement:

It has been shown in reference [9] that the use of threaded rods as model reinforcement provides (a) nearly perfect modeling of low level flexural cycles, (b) correct ultimate strength even after severe loading, and (c) an acceptable cracking behavior through the different stages of loading. It was also reported [9] that cold forming of the threaded rods significantly increases the yield strength, and a heat-treatment process was essential to reduce the yield strength to the required level (around 40 ksi in the present case), and to produce an adequate yield plateau. A full account of the heat-treatment technique adopted in the current work can be

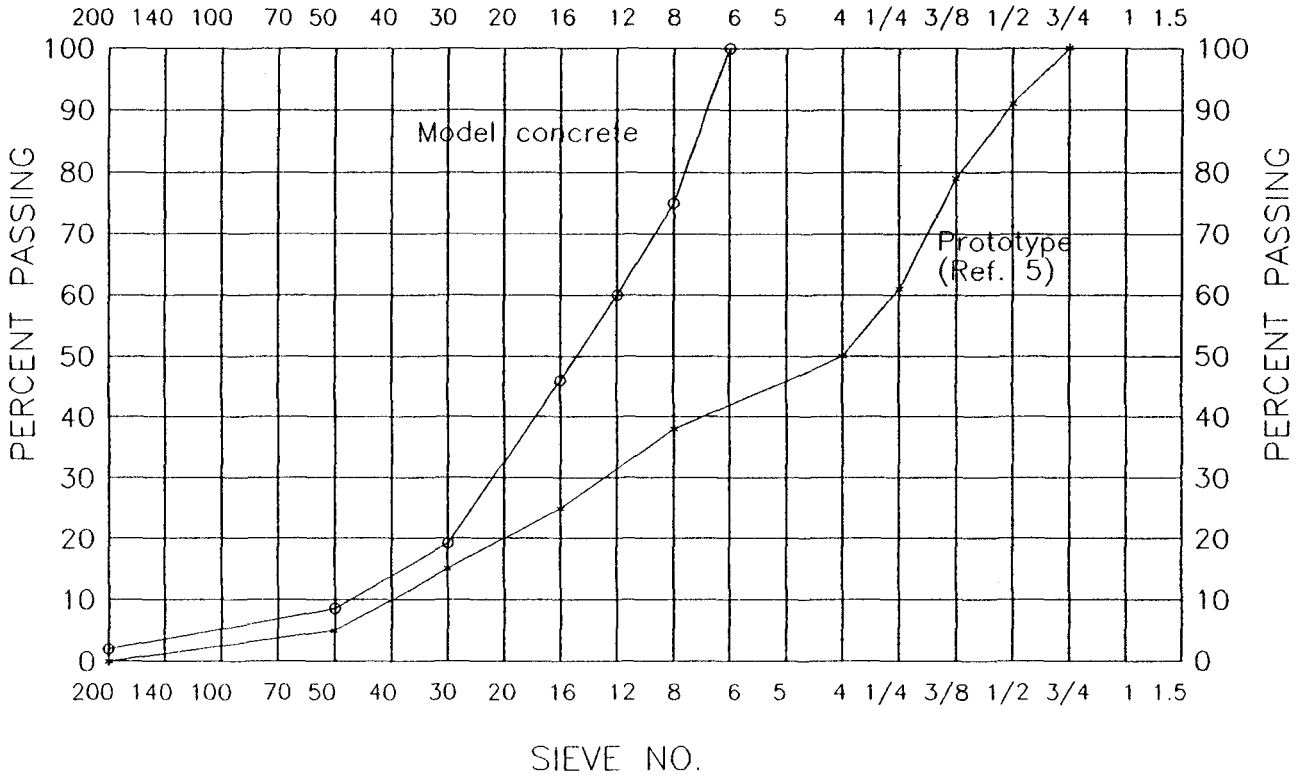


Figure 2.2. Model Concrete Aggregate Grading.

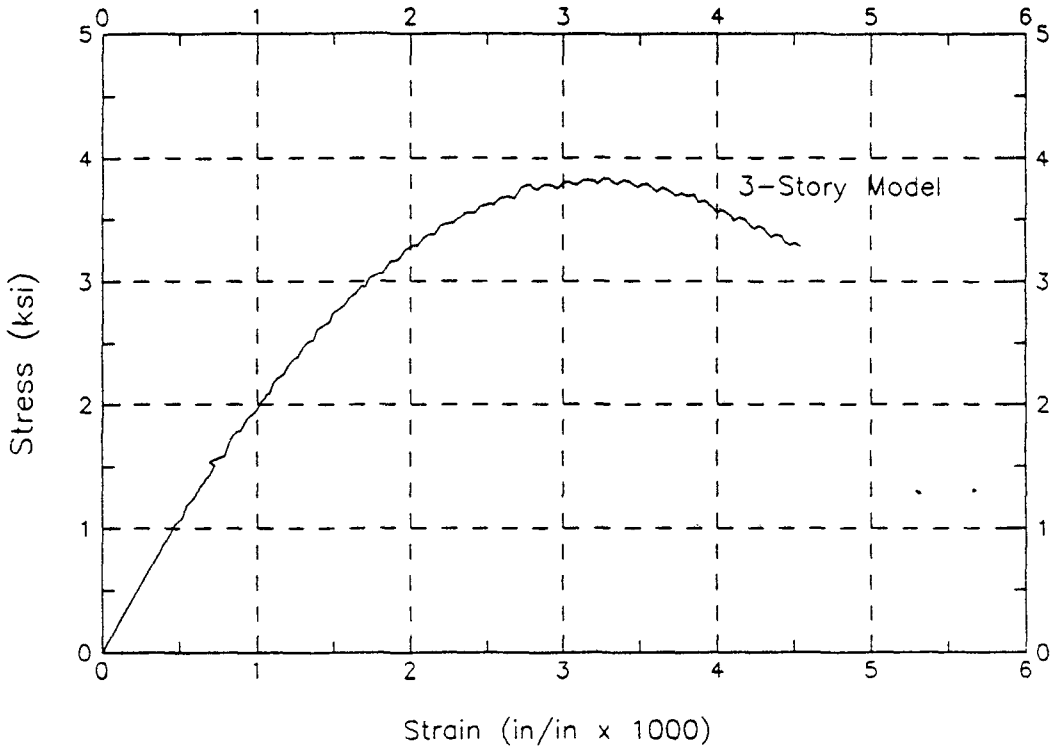


Figure 2.3. Microconcrete Stress–Strain Curve.

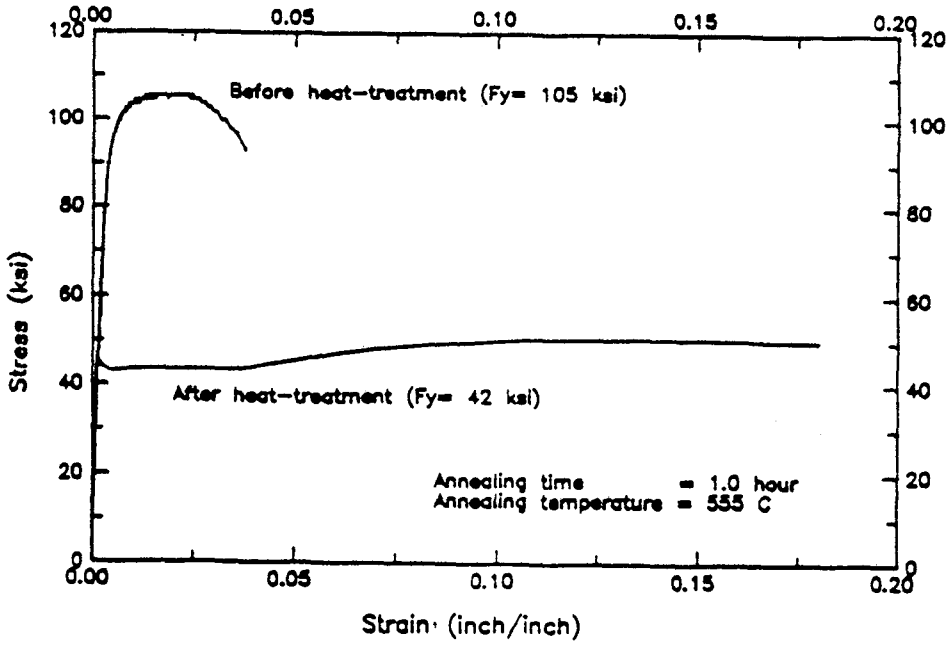


Figure 2.4: Stress-Strain Curves of Original Versus Heat-Treated Model Reinforcement (Size 6-32).

found in references [7] and [9]. A typical model reinforcement stress-strain curves before and after the heat-treatment is shown in figure 2.4.

### Details and fabrication of the model structure.

Realistic reinforcement details that reflected construction practices during the 1950 to 1970 period were adopted. Special attention was paid to critical details such as the beam-column joints and column lap splices. Figure 2.5 shows an interior and an exterior non-seismically detailed joints. The non-seismically detailed joints are characterized by (a) discontinuous bottom beam reinforcement with a very short embedment length (6"), (b) no beam or joint confinement except for several stirrups at a spacing of 3" (usually) located at 3" below the beam bottom face, (c) no joint reinforcement (column stirrups do not continue through the joint length), (d) lap splice is designed as a compression splice (short splice) and located immediately above the beam top face, and (e) no special confinement was required for the lap splice. The reinforcement details of the main frame in the direction of motion are shown in figure 2.6.

As a result of reviewing several designs and reinforcement details performed prior to 1970, an empirical splice length of 24 bar diameter was used. The fabrication procedure of the model building was designed to resemble as closely as possible the construction steps of full scale buildings. The adopted technique is summarized in reference [5].

### Load set-up and model instrumentation

(a) Load set-up

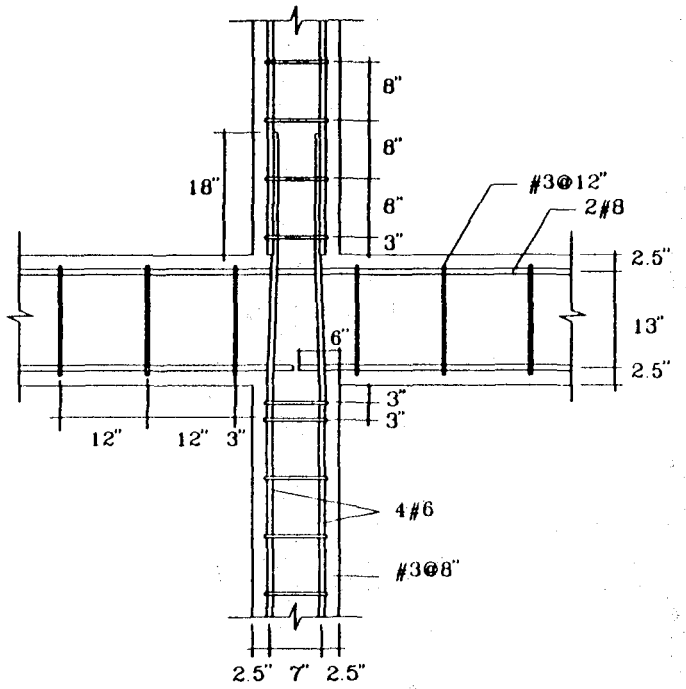


(a) Interior Joint.

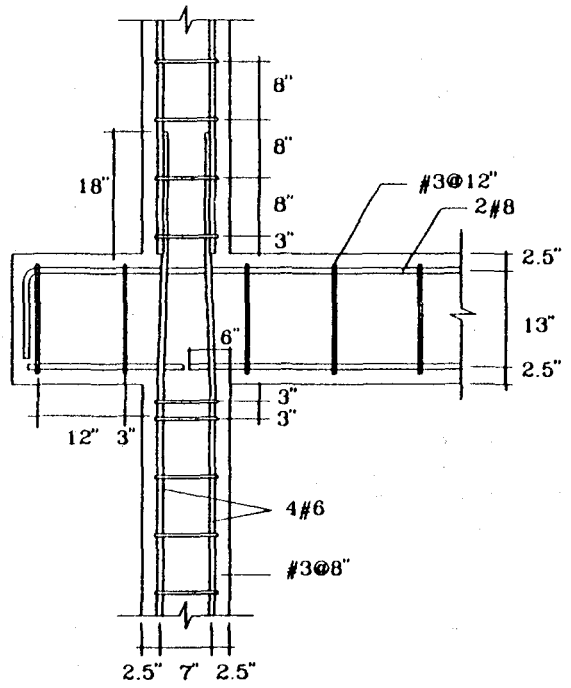


(b) Exterior Joint.

Figure 2.5: Beam-Column Joint Details of The Prototype 3-Story Model Building.

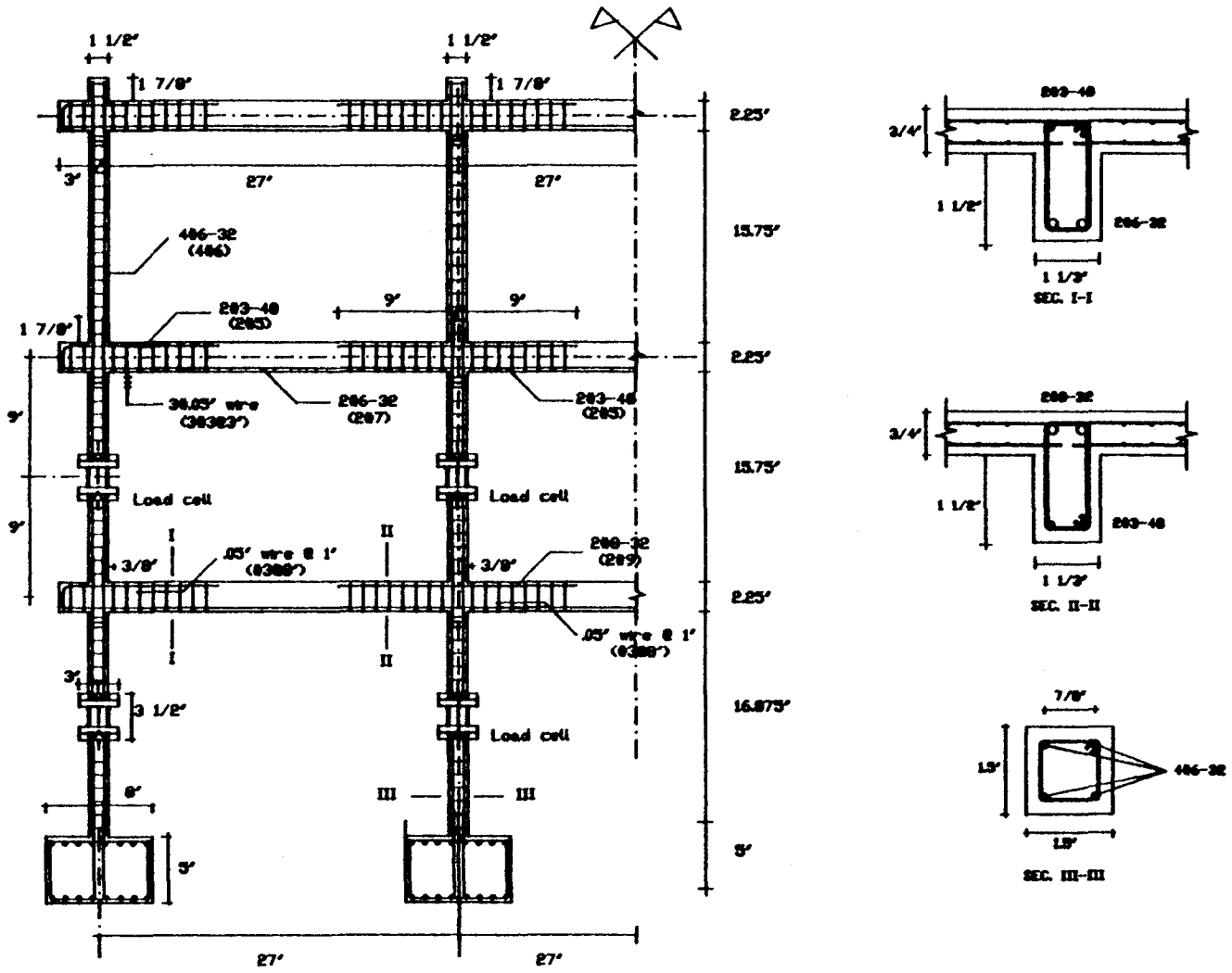


Figure 2.6: Reinforcement Details of The 3-Story Model (Prototype) Building.

Additional masses were used to simulate the dead weight of the prototype building according to the similitude requirements in table 2.1. For each story, the added masses were computed as follows:

$$M_m = \frac{M_p}{S_l^2} - M_{m_{O.W}} \tag{2.3}$$

Where $M_m$ = additional mass to be added on the model first story, $M_p$ = prototype single story dead load, and $M_{m_{O.W}}$ = own weight of the model floor.

4" × 4" × 2" lead blocks with an average weight of 12.6 lbs. were used to simulate the prototype building dead loads. These masses were mounted directly on the floor slab for more realistic representation of the load transfer from the slab to the beams and finally to the columns. The mounting technique was designed so that (a) the center of mass of the added blocks coincided with the slab mid-thickness, and (b) the increase in the slab stiffness due to the presence of the lead blocks is minimum. This was done by mounting an equal number of blocks above and below the floor slab as shown in figure 2.7. The blocks were connected together using 0.5" diameter steel bolts running through 0.75" holes in the slabs. A set of 1.5" diameter, 0.125" thick steel washers were installed between the lead blocks and the slab to avoid direct contact and consequently minimize the slab stiffening. More masses were used near the floor beams for better simulation of wall loads.

(b) Model instrumentation

The model displacements were measured using linear displacement transducer (MTS Temposonic [12]) at two points 25" apart at each floor level (figure 2.7). This set-up also captures any rotational motion of the model during vibration.

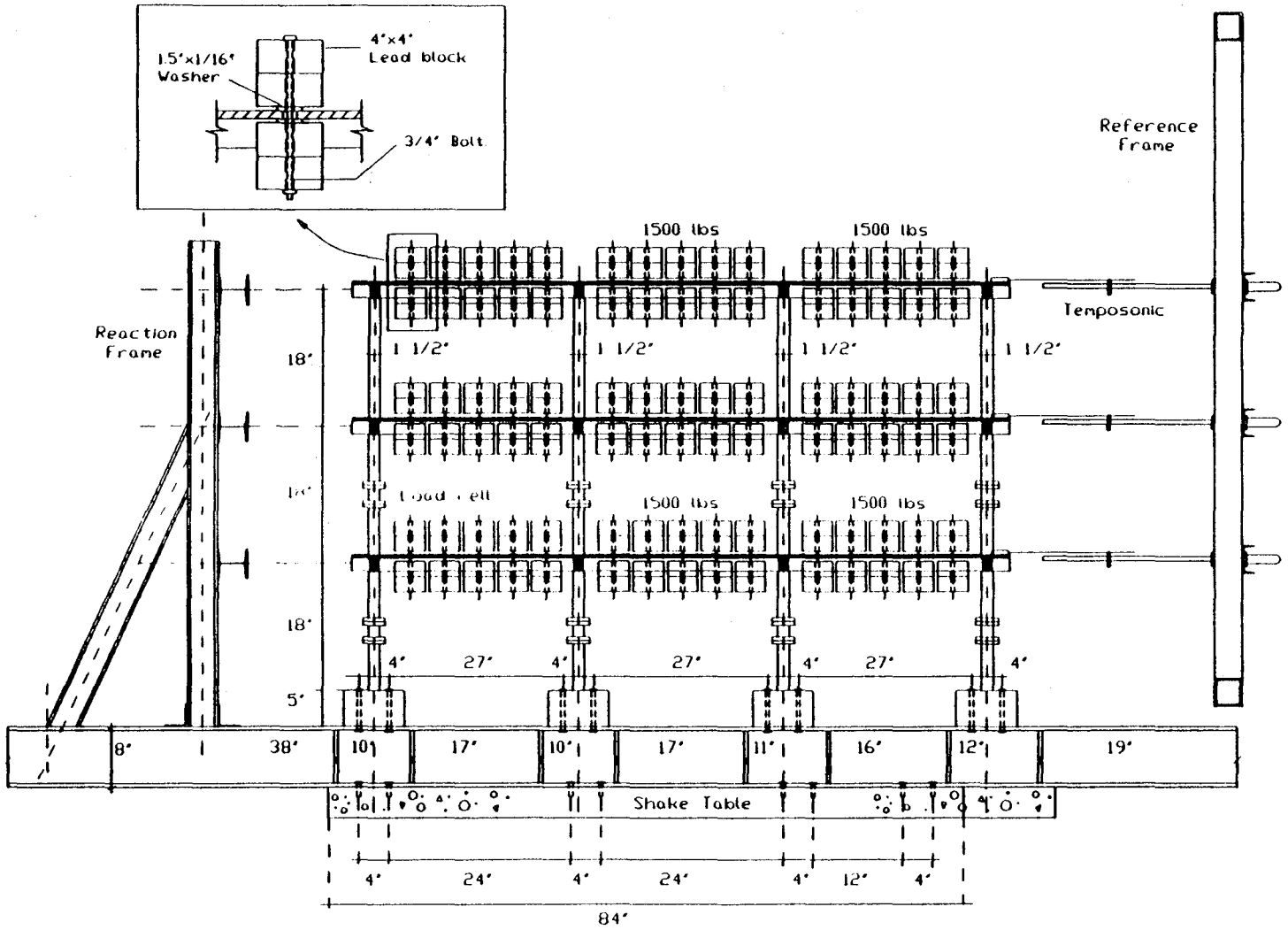


(a) Loads -- magnitudes and locations

Fig. 2.7: Load Set-Up for the 3-Story Building Model

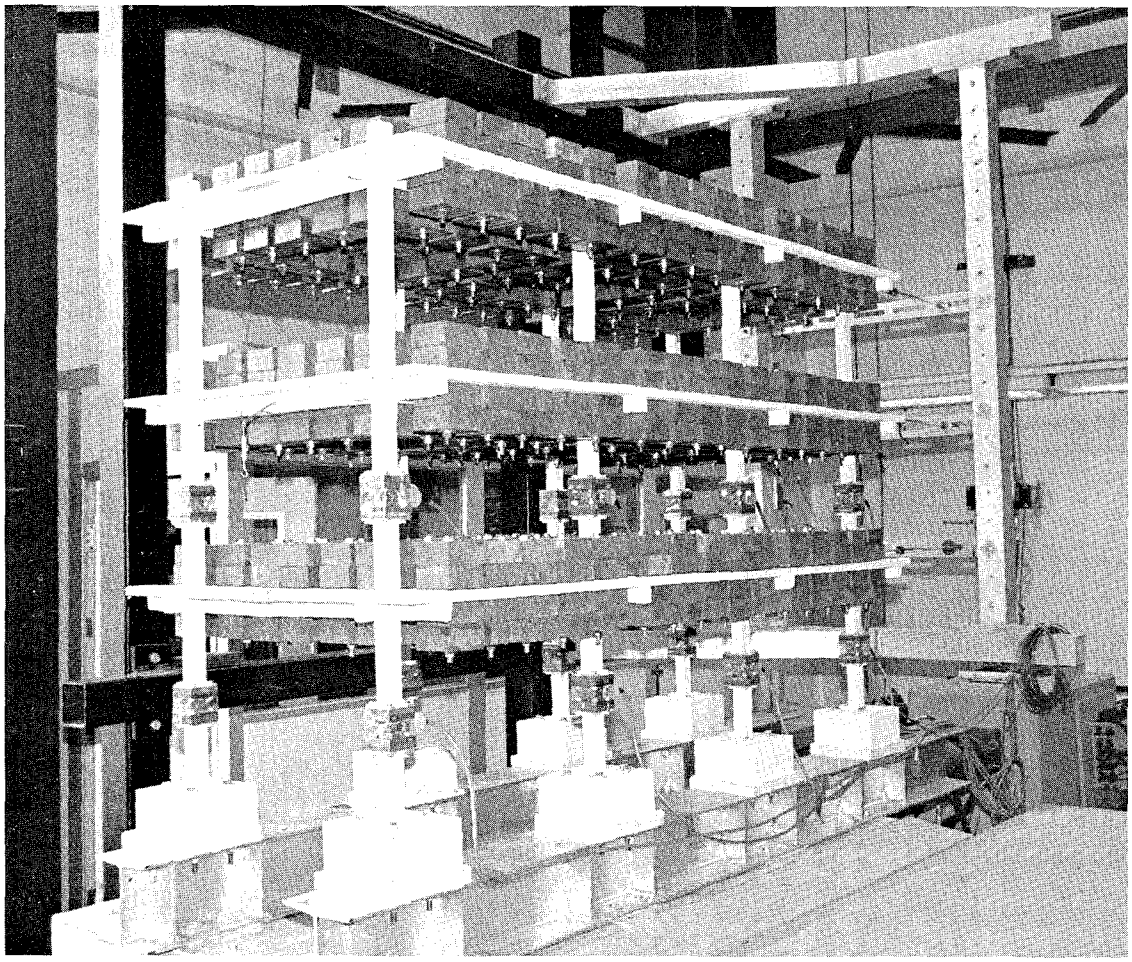

(b) Loads on the model structure

Fig. 2.7 (continued)

More information about these devices can be found in [12]. The table acceleration along with the floor accelerations were measured using ENDEVECO piezoresistive accelerometers model 7265. A full account of the theory of operation, performance characteristics, and electronics of these accelerometers can be found in [6].

The model columns were instrumented with specially manufactured load cells at their mid heights as shown in figure 2.6. Active load cells were installed at the mid heights of the first and second story columns of one frame. Dummy cells were used for the other frame to maintain symmetry of the model stiffness. The load cells, being capable of sensing axial force, bending moments, and shearing force, reduced the first story of the model structure to a statically determinate sub-assemblage. The time-history of the straining actions on critical sections in the first story beams and columns could be measured due to the presence of these cells. A full account on the mechanical and electronic design of the load cells along with their calibration and installation schemes are provided in details in appendix B.

## 2.2 Test procedure

### 2.2.1 Introduction

The model structure was subjected to a series of tests to evaluate its performance before, during, and after earthquakes of different magnitudes. The general behavior of the models was studied through the following parameters: (a) base shear, (b) inter-story shear, (c) inter-story drift (time history), (d) flexibility matrix coefficients, (e) natural frequencies, (f) damping ratios (assuming viscous damping model), and (g) cracking behavior and visual damage.

Since the 3-story building model was instrumented with load cells in the first and the second story columns, it was possible to examine the response time-history of particular members in the structure and evaluate their performance. The following additional parameters were investigated: (a) column axial force, (b) top and bottom column moments, (c) column shearing force, (d) beam moments (for the first story only).

Three types of tests were conducted to study these parameters: (a) flexibility matrix determination test (static test), (b) free vibration test, (c) simulated earthquake tests (seismic test).

The first two tests were carried out before and after each seismic test to evaluate the changes in structural properties from the seismic test. The third test consisted of applying the time scaled Taft S69E 1952 earthquake component to the model structure at different amplitudes until significant damage was observed. The techniques used to perform these tests are discussed in detail in the following sections.

### 2.2.2 Static flexibility matrix determination

Figure 2.8 shows the load set-up used to determine the static flexibility matrix coefficients of the 3-story building . A static concentrated load was applied at each floor level using a 1000 lb capacity manual jack. The applied load was measured using a 1000 lb capacity load cell, and the model displacements were measured using 4 Temposonics (2 at each floor level). The load was applied in four increments of 50 lbs each. The flexibility matrix coefficients were computed at each load increment and finally all four values were averaged to obtain a $3 \times 3$ symmetric matrix. A

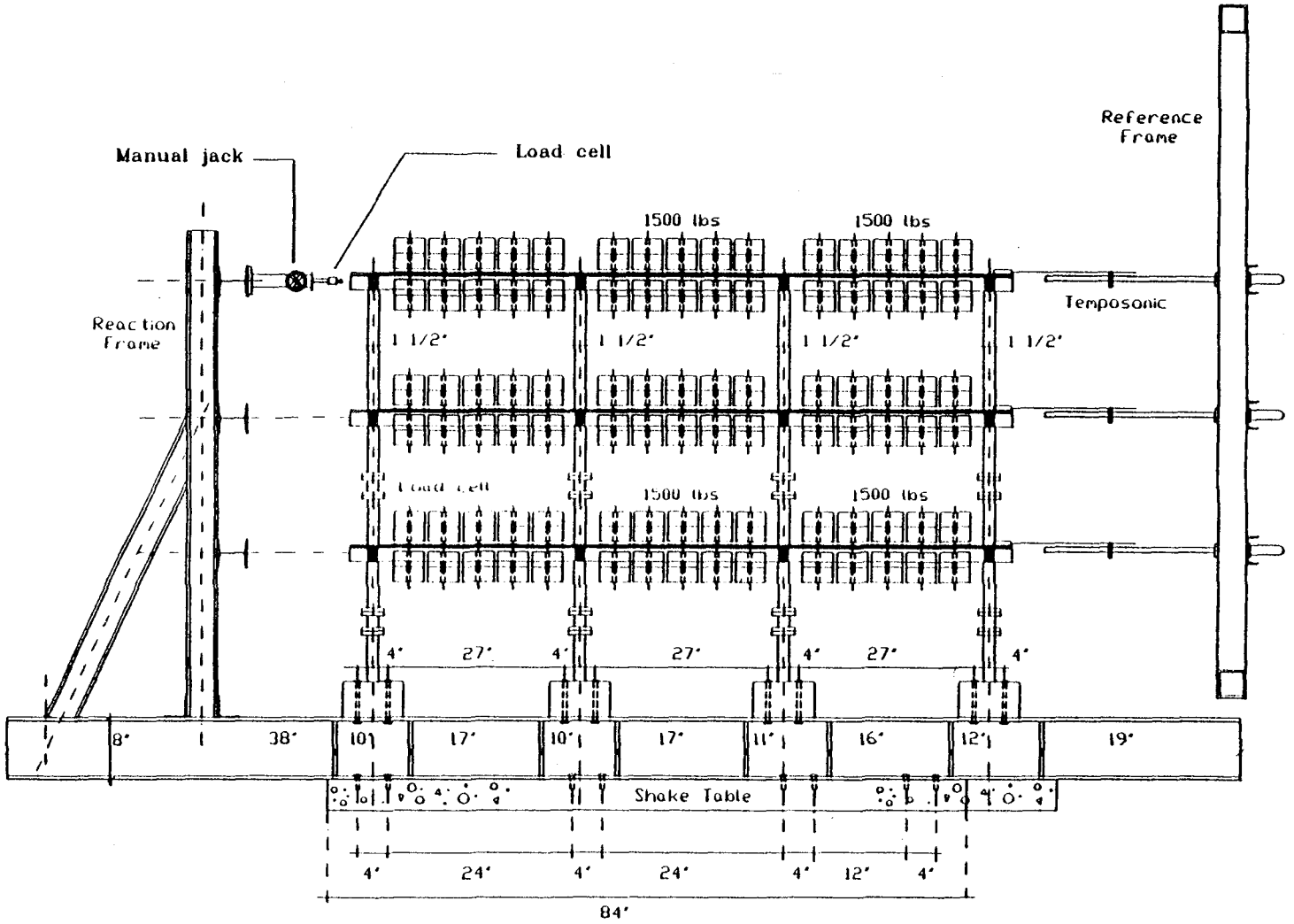


Figure 2.8: 3-Story Building Static Test Load Set-Up.

similar procedure was used for the 2-story model to obtain a $2 \times 2$ flexibility matrix.

The obtained flexibility matrix along with the mass matrix were used to compute the eigenvalues (natural frequencies) of the system using equation 2.4. These frequencies were compared with those obtained from the free vibration test to check the validity of the two tests.

$$[M] \times \{q\} = \frac{1}{\omega^2} \times [F] \times \{q\} \tag{2.4}$$

Where $[M]$ = measured mass matrix, $[F]$ = measured flexibility matrix, $\{q\}$ = eigen vector(s), and $\omega$ = circular frequency.

### 2.2.3 Free vibration test

Figure 2.9 shows the load set-up used for the free vibration test of the 3-story model. The model structure was pulled back (displaced) by 0.05 inches at the second floor level using a steel wire. The wire was then suddenly released (cut) and the structure was allowed to vibrate freely. Accelerations and displacements were measured at each floor level until the structure motion damped out. A typical data gathering time was about 20 seconds.

The gathered data (figure 2.10.a) was used to compute the natural frequencies of the model using a Fast Fourier Transform algorithm (FFT) (figure 2.10.b). Knowing the natural frequencies of the model, the same data was band-pass filtered to isolate the response corresponding to each vibration mode (figures 2.10.c through 2.10.e). These separated motions were again used to obtain the damping ratios of each mode using the well known "Logarithmic Decrement" technique, assuming a viscous damping model.

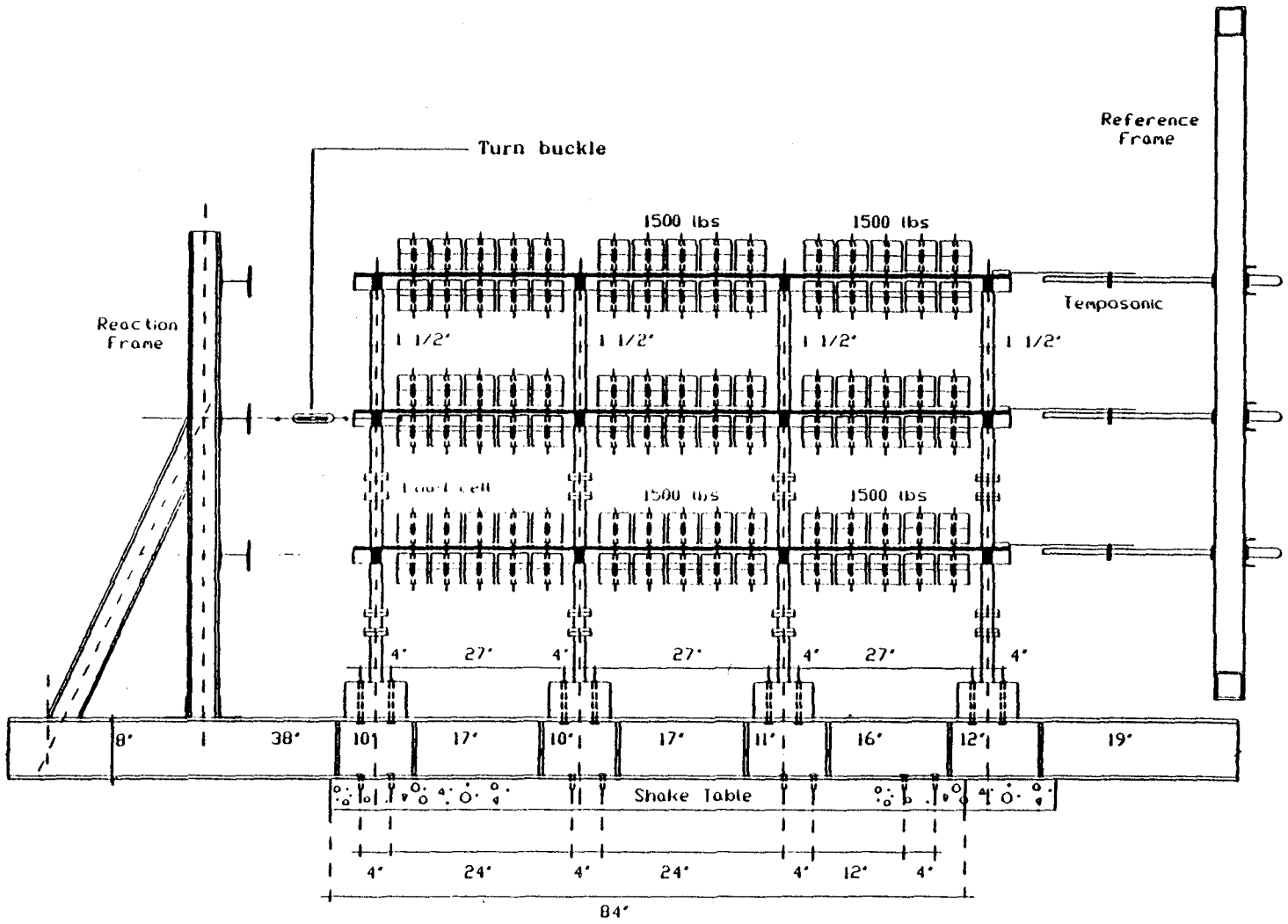


Figure 2.9: 3-Story Building Free Vibration Test Load Set-Up.

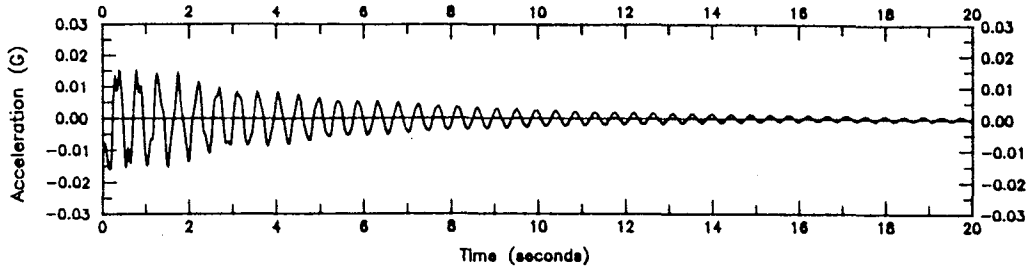


(a) Third Floor Acceleration (Free Vibration Test FV2)

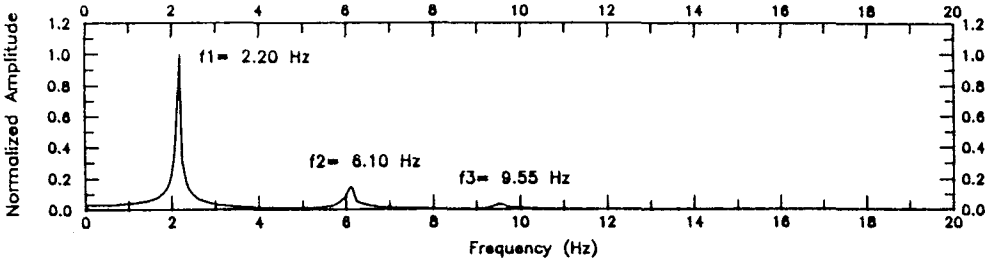


(b) Power Spectrum of The Third Floor Acceleration
(Free Vibration Test FV2)

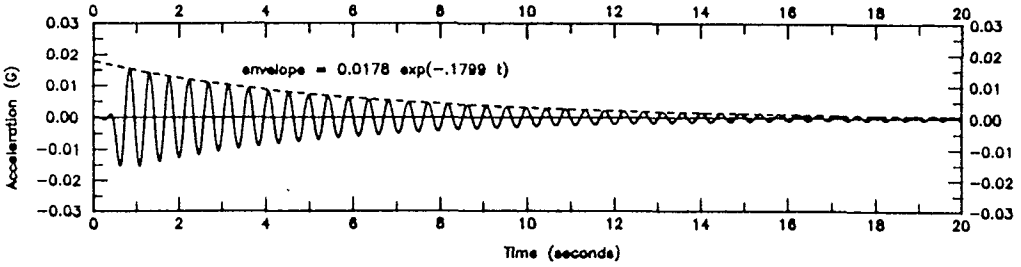


(c) Third Floor Acceleration After Low-Pass Filtering at 3 Hz
(Free Vibration Test FV2)

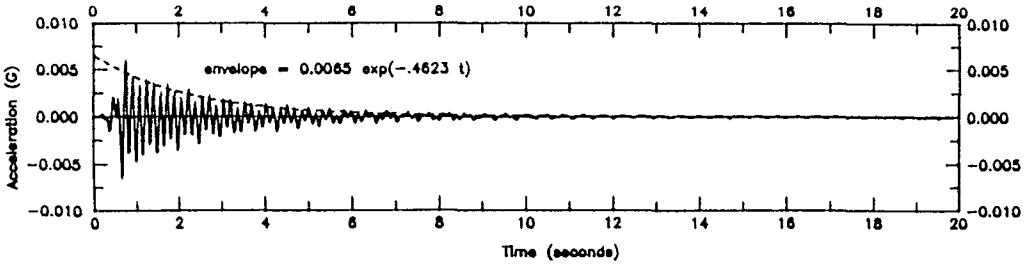


(d) Third Floor Acceleration After Band-Pass Filtering at 4-8 Hz
(Free Vibration Test FV2)

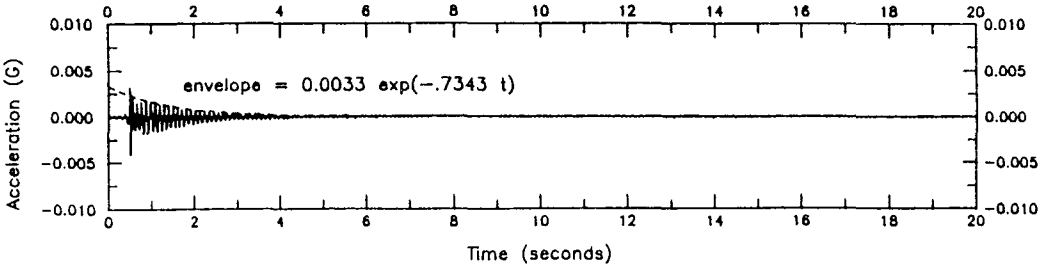


(e) Third Floor Acceleration After High-Pass Filtering at 8 Hz
(Free Vibration Test FV2)

Figure 2.10: Sample Results of The 3-Story Building Free Vibration Test.

The third story acceleration data was used to evaluate both the natural frequencies and the damping ratios of the 3-story model structure after every seismic test. A curve fitting algorithm was then used to obtain the logarithmic curve that best fits the envelope of the acceleration trace within the concerned range. The viscous damping ratio for both modes were directly obtained from the fitted curve equation (figures 2.10.c, d, e).

### 2.2.4 Simulated earthquake tests

The first 25 seconds of the Taft S69E 1952 earthquake (figure 2.11) were applied to the model structure at different amplitudes to evaluate its performance under seismic excitation. The used record was time-compressed by a factor of $S_t = \sqrt{S_l}$ to satisfy the similitude requirements. This resulted in the shift of the response spectrum curve shown in figure 2.12. Although the active seismic excitation time was about 10 seconds (after time compression), the model responses were recorded for 30 seconds to capture the free vibration response after the earthquake.

The magnitude of the earthquake was defined as the maximum ground acceleration applied to the model building. Although the shake table was "prequalified" using similar loading conditions to those of the reinforced concrete model, it was still difficult to reproduce a certain earthquake with specific maximum amplitude during the actual test. This was due to the fact that the transfer function of the shake table was determined using a linear elastic structure while the actual reinforced concrete model was highly non-linear.

All seismic tests were video taped for later, slow motion display. This was found to be useful in reviewing and visually comparing different tests.

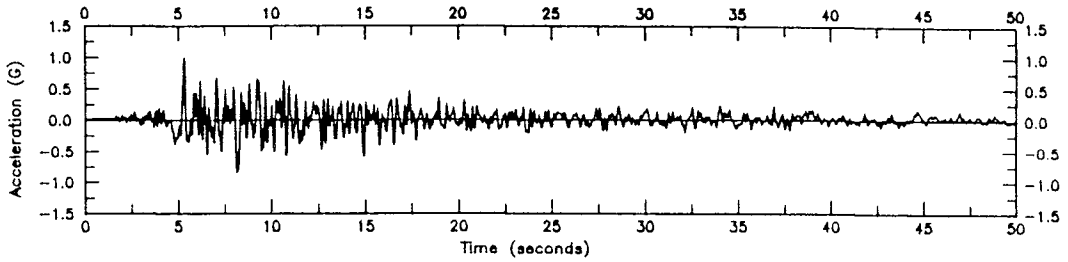


(a) Normalized Original Taft 1952 S69E Earthquake.

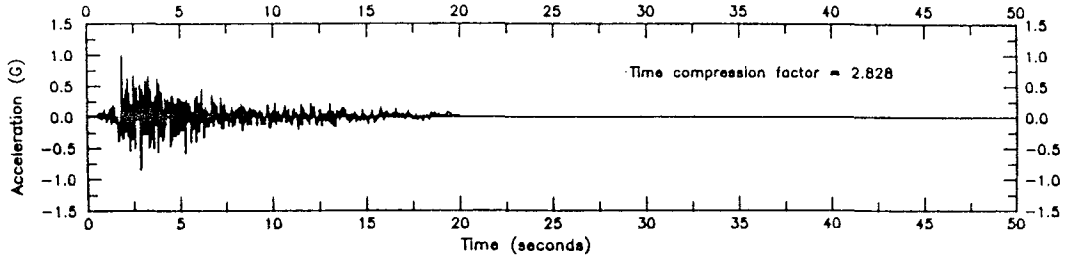


(b) Normalized Time-Compressed Taft 1952 S69E Earthquake.
(Used for The 3-Story Model Test).

Figure 2.11: Original Versus Time-Compressed Taft 1952 S69E Earthquake.

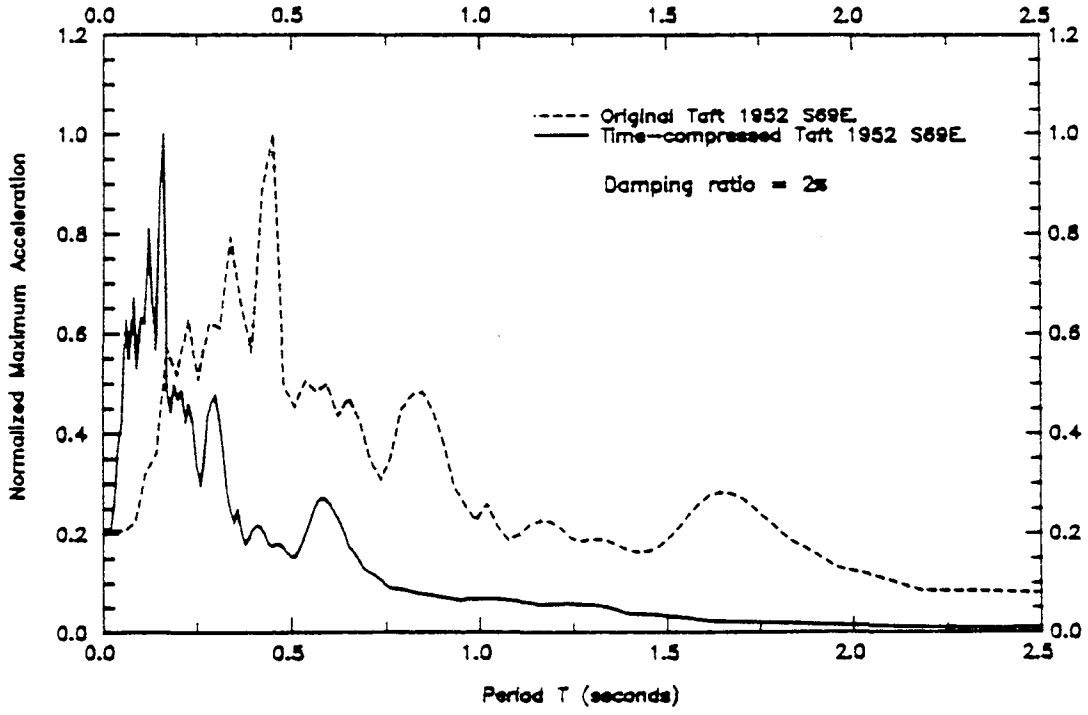


Figure 2.12: Effect of Time-Compression on Response Spectrum.

# CHAPTER 3

# TEST RESULTS

## 3.1 Introduction

Results of the 3-story building test including static, free-vibration, and simulated earthquake tests are presented and discussed in this chapter. For each seismic test, the global response of the model (in terms of story displacements, story shears, etc.) will be introduced first, followed by an evaluation of the performance of specific elements (beams, columns, and joints) during the test. Experimental results presented in this chapter will be compared with the analytical results in chapter 4.

## 3.2 Test program

The model structure was subjected to four simulated earthquake tests using the time-compressed Taft S69E 1952 accelerogram at increasing amplitudes. Each seismic test was preceded and followed by a static test and a free-vibration test to evaluate the changes of the model properties. The intensity of the seismic tests were based on the approximate damage indices of different members provided by program IDARC in addition to the experience gained from the 2-story building test. The four seismic runs were as follows:

- The first run represented a low amplitude earthquake with a peak table acceleration of 0.05 g (where g is the ground acceleration). This run was

intended to study the elastic behavior of the model and to verify that the data acquisition system and the table control devices were functioning properly.

- The second run represented a moderate earthquake with a peak table acceleration of 0.18 g (the peak ground acceleration of the original Taft S69E 1952 earthquake was 0.16 g). Clearly the objective of this run was to evaluate the response of a non-seismically detailed building subjected to a realistic ground motion that might occur in the Central or Eastern United States.

- The third run simulated a strong earthquake with a peak table acceleration of 0.35 g. The purpose of this run was to evaluate the response of the already damaged structure to a high amplitude earthquake (maximum ground acceleration of El-Centro 1940 earthquake was 0.35 g).

- The final run applied to the model was of a very high intensity (0.8 g), and was intended to investigate the failure mechanism of the structure rather than to investigate the model performance.

Results of each of these runs will be presented in detail in the following sections.

## 3.3 Initial properties of the model

Static reactions of the first and the second story columns were obtained from the changes in the load cell readings due to the addition of the lead blocks. It can be seen from table 3.1 that the measured reactions were in good agreement with those obtained using linear elastic analysis. The additional straining actions on

Table 3.1: Computed Versus Measured Static Reactions Due to Lead Blocks Load.

| Column | Axial Force (kips) | | Shear Force (kips) | |
|---|---|---|---|---|
| | Calculated | Measured | Calculated | Measured |
| 1-A | 1.01 | — | 0.02 | — |
| 1-B | 2.51 | 2.53 | 0.00 | — |
| 1-C | 2.51 | 2.48 | 0.00 | 0.00 |
| 1-D | 1.01 | 1.01 | 0.02 | 0.02 |
| 2-A | 0.67 | 0.67 | 0.04 | 0.05 |
| 2-B | 1.67 | 1.78 | 0.01 | 0.00 |
| 2-C | 1.67 | — | 0.01 | 0.00 |
| 2-D | 0.67 | 0.80 | 0.04 | 0.06 |

Table 3.2: Variation of The 3-Story Model Natural Frequencies and Damping Ratios

| Test | Natural Frequencies (Hertz) | | | Damping Ratios (% of Critical Damping) | | |
|---|---|---|---|---|---|---|
| | $f_1$ | $f_2$ | $f_2$ | $\zeta_1$ | $\zeta_2$ | $\zeta_3$ |
| Unloaded Model | 6.60 | 19.80 | 31.60 | — | — | — |
| Loaded Model | 2.20 | 6.10 | 9.55 | 1.30 | 1.20 | 1.20 |
| Taft 0.05 g | 2.20 | 6.00 | 9.50 | 1.30 | 1.20 | 1.20 |
| Taft 0.18 g | 1.80 | 4.90 | 7.65 | 2.74 | 2.25 | 1.52 |
| Taft 0.35 g | 1.65 | 4.50 | 6.95 | 2.76 | 2.25 | — |

the columns due to the floor's own weight (which formed only 4.2 % of the total load) were estimated using elastic analysis.

Both free-vibration and static tests were performed before and after the addition of the lead blocks. It can be observed from table 3.2 that the fundamental frequency of the model corresponding to its first mode of vibration decreased from 6.6 Hz to 2.2 Hz (67% decease) due to the existence of the additional masses. Similar reductions were observed for the second and the third modes (69% and 70% respectively).

Damping ratios obtained assuming a viscous damping model and using the logarithmic decrement technique (explained in chapter 2) are presented in table 3.2 for all three modes of vibration. The low damping ratios recorded for the loaded structure indicates that few cracks were developed in the model at this stage. For later runs these figures increased significantly.

The flexibility matrix coefficients were significantly reduced due to the addition of the lead blocks indicating an increase in the model stiffness. This stiffening could be attributed to (a) the stiffening of the floor slab due to mounting the lead blocks, and (b) the closing of shrinkage and construction joints cracks in columns. Inspection of the flexibility coefficients provided in table 3.3 indicates that reductions of 57%, 55%, and 44% were recorded for $f_{11}$, $f_{22}$, and $f_{33}$ respectively. The trend of the reduction suggests that lower columns which were subjected to higher axial forces showed higher increase in their stiffness than upper ones, emphasizing the role of the second factor cited above.

Table 3.3: Variation of Flexibility Matrix Coefficients

| Test | Flexibility Coefficient $in/lb \times 10^{-5}$ | | | | | |
|---|---|---|---|---|---|---|
| | $f_{11}$ | $f_{12}$ | $f_{13}$ | $f_{22}$ | $f_{23}$ | $f_{33}$ |
| Unloaded Model | 18.06 | 18.62 | 19.54 | 34.82 | 34.90 | 52.39 |
| Loaded Model | 7.80 | 8.39 | 9.40 | 18.14 | 19.44 | 29.28 |
| Taft 0.18 g | — | — | — | — | — | — |
| Taft 0.35 g | 13.98 | 14.41 | 15.27 | 29.64 | 30.68 | 48.49 |

## 3.4 Run Taft 0.05 g

### 3.4.1 Global response

The time-history of the story displacements and story shears during run Taft 0.05 g are shown in figures 3.1 and 3.2 respectively. It can be observed from both figures that all 3 stories were moving in phase, indicating the domination of the first mode of vibration. Damping ratios recorded during this run were low compared to those obtained in subsequent runs (table 3.2). As the free-vibration test was conducted after this run, no significant changes in the natural frequencies of the model were detected. It was concluded that the model was acting as an under-damped, elastic, single degree of freedom system during this run.

Mode shapes and story shears at the time of maximum base shear are shown in figure 3.3 for all seismic tests. The maximum top-story drift during the present run was only 0.13% of the total height, while the maximum base shear represented 2.3% of the total vertical loads. Second and third story shears were 63% and 32%

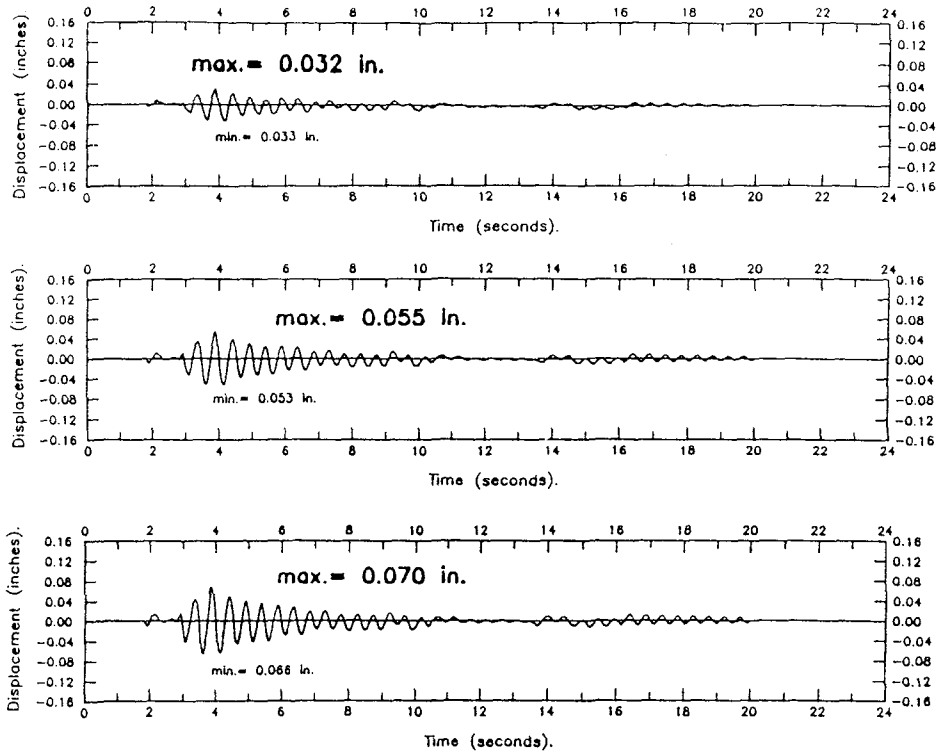


(a) First Story

(b) Second Story

(c) Third Story

Figure 3.1: **Story Displacements (Run Taft 0.05-G).**

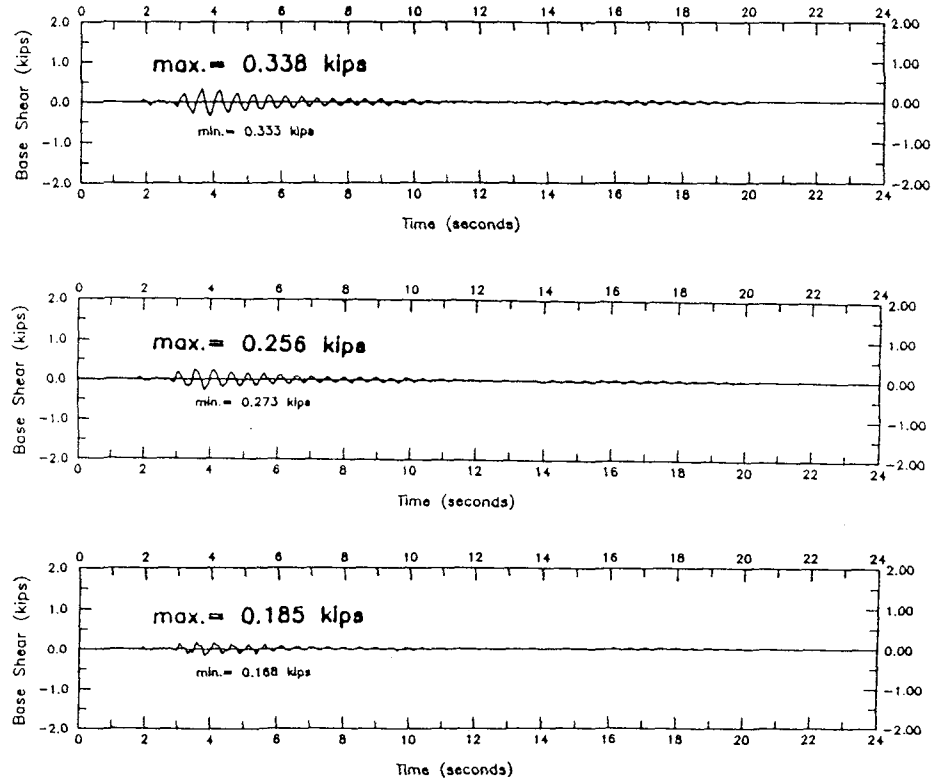


(a) Base Shear

(b) Second Story

(c) Third Story

Figure 3.2: **Story Shears (Run Taft 0.05-G).**

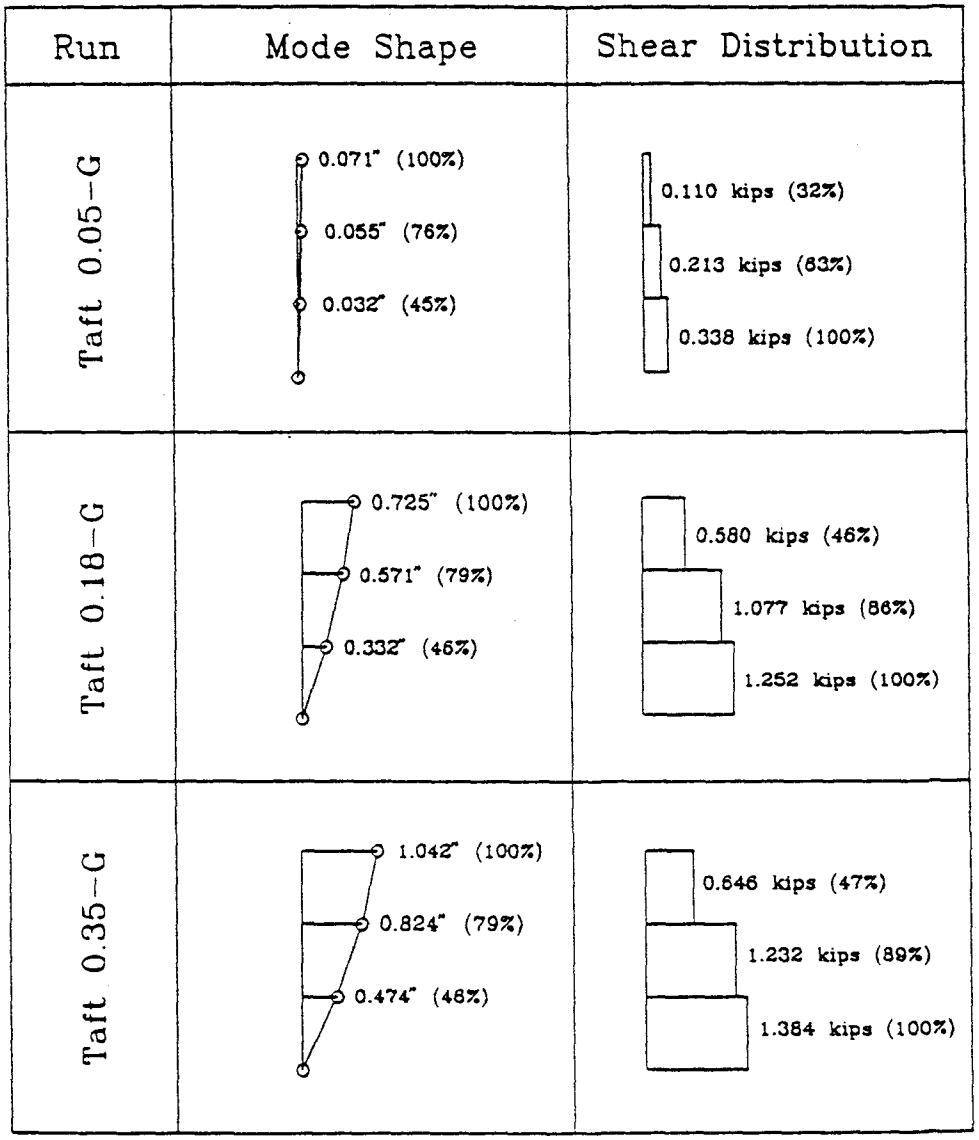


Figure 3.3: Mode Shapes and Shear Distribution at The Maximum Base Shear.

of the maximum base shear respectively.

Story shears are plotted against the inter-story drift in figures 3.4.a through 3.4.c corresponding to the first, the second, and the third stories respectively. These curves provide a general idea of the hysteretic response of individual stories along with their average stiffness during the seismic run. Integration of these curves provides an approximate means of comparing the energy dissipated by each story. It can be seen that for all three stories the behavior was nearly linear, with relatively close stiffness of the top and bottom stories and a slightly higher stiffness of the middle story (as expected from the elastic analysis). Negligible energy was dissipated by all stories during this run as would be expected from a linear elastic system.

### 3.4.2 Local response

The time-histories of the column shears are shown in figures 3.5 and 3.6 for the bottom and the second stories respectively. It can be observed from both figures that identical columns (exterior or interior) experienced nearly equal shearing forces during this run. However, the story shears was not equally shared between exterior and interior columns as shown in table 3.4. For the first story, the average interior columns shear was about 1.92 times that of the exterior columns. This figure was reduced to 1.54 times the exterior column shears for the second story interior columns.

Story shears obtained from the acceleration measurements were in good agreement with those obtained from the load cell measurements for both the bottom and the second stories (figure 3.7). The good correlation between both measurements

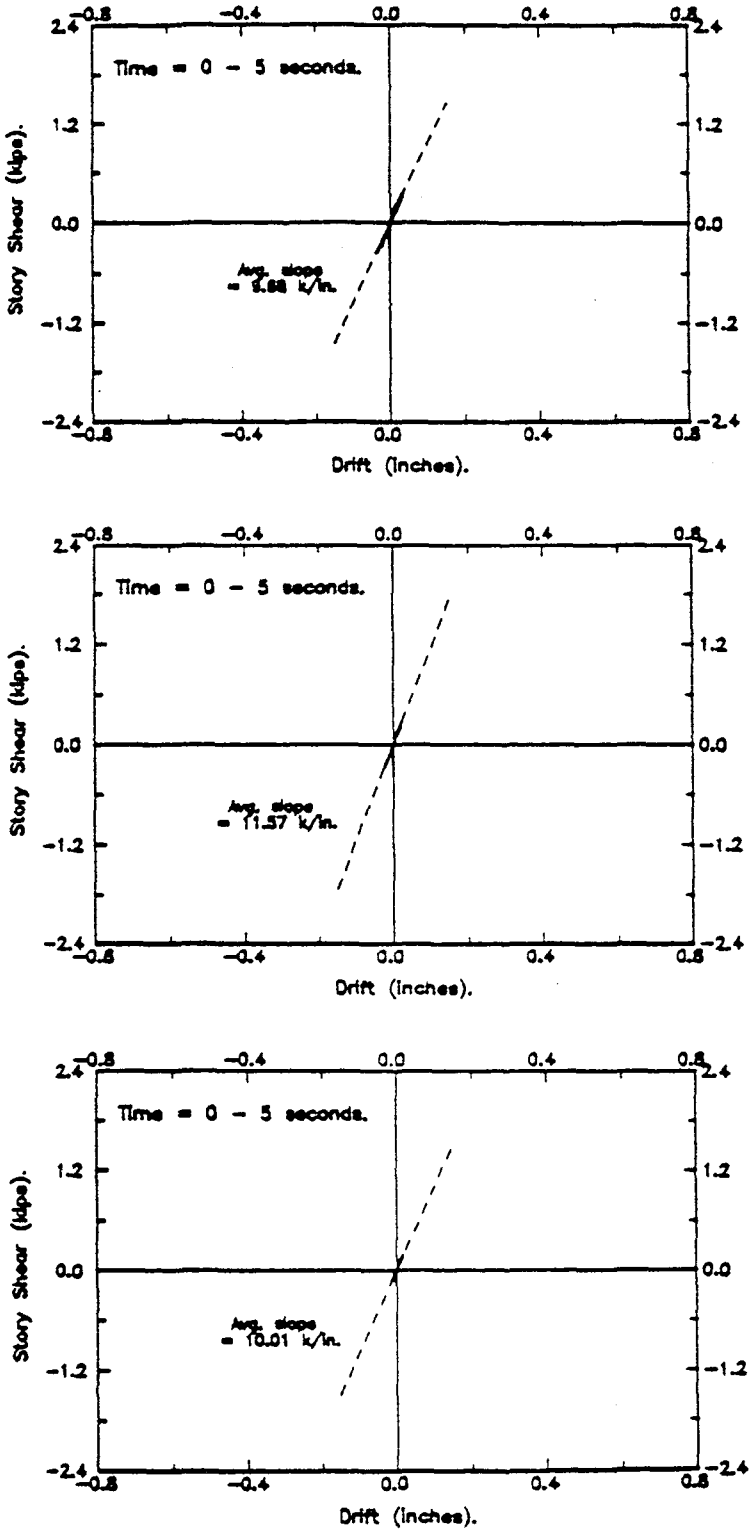


Figure 3.4: Story Shear Versus Inter-Story Drift Hysteresis Curves (Run Taft 0.05-G).

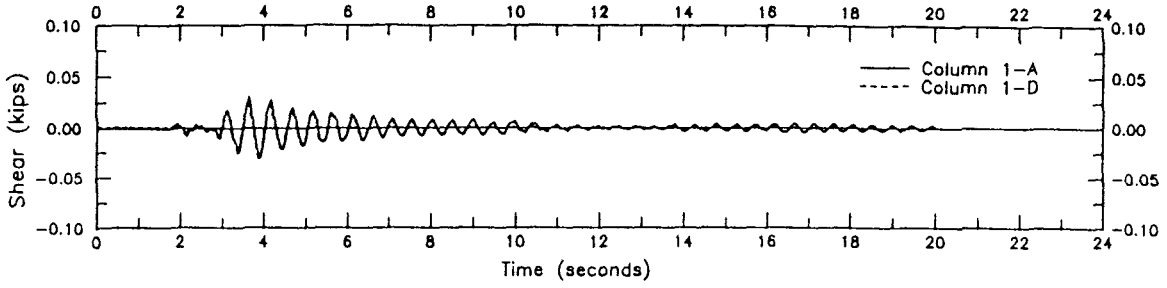


(a) Shear Force in Exterior Columns (1-A) and (1-D).

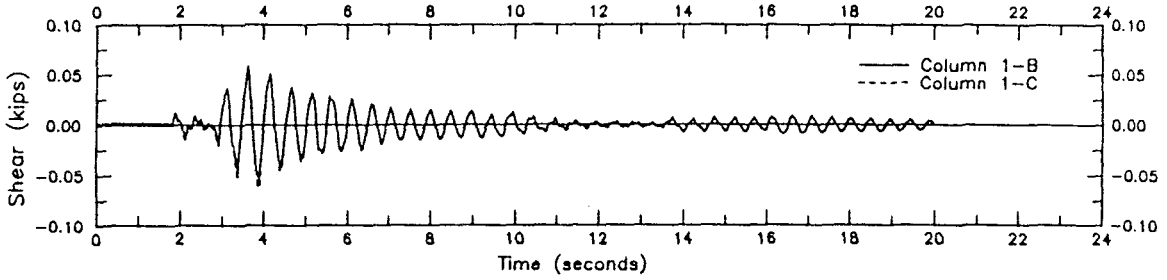


(b) Shear Force in Interior Columns (1-B) and (1-C).

Figure 3.5: **First Story Columns Shear (Run Taft 0.05-G).**

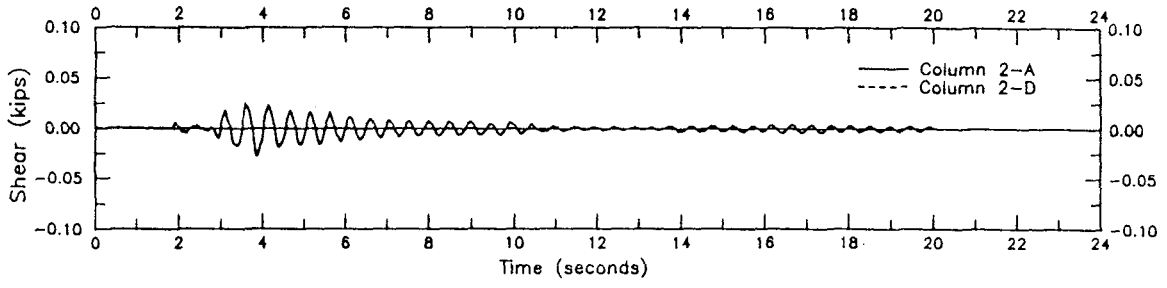


(a) Shear Force in Exterior Columns (2-A) and (2-D).

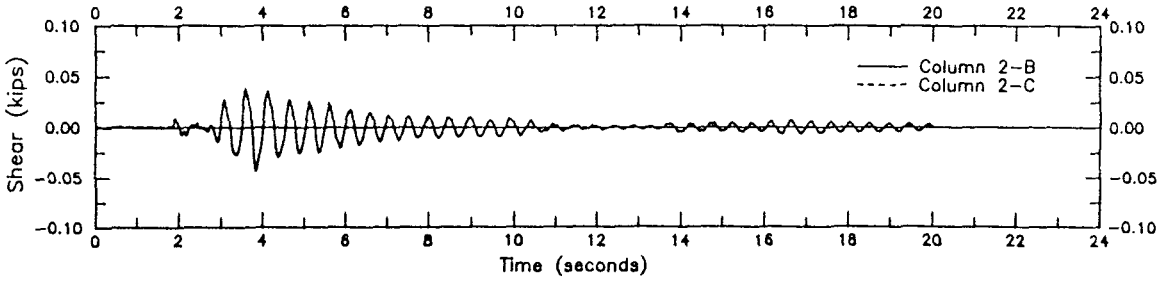


(b) Shear Force in Interior Columns (2-B) and (2-C).

Figure 3.6: **Second Story Columns Shear (Run Taft 0.05-G).**

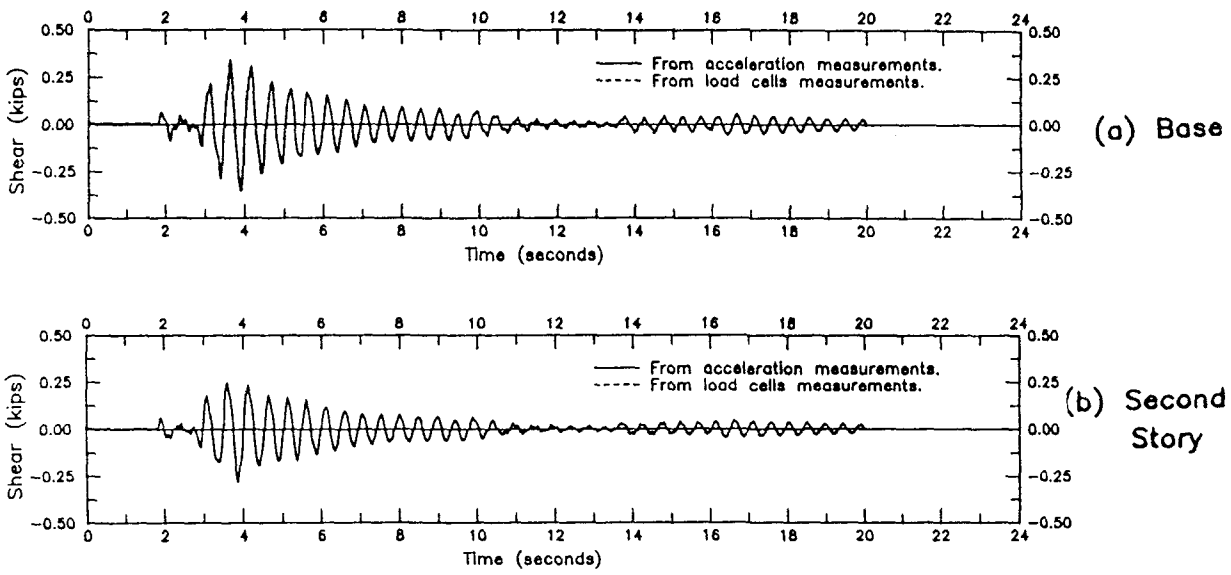


Figure 3.7: Story Shears Based on Acceleration Measurements Versus Story Shears Based on Load Cell Measurements.

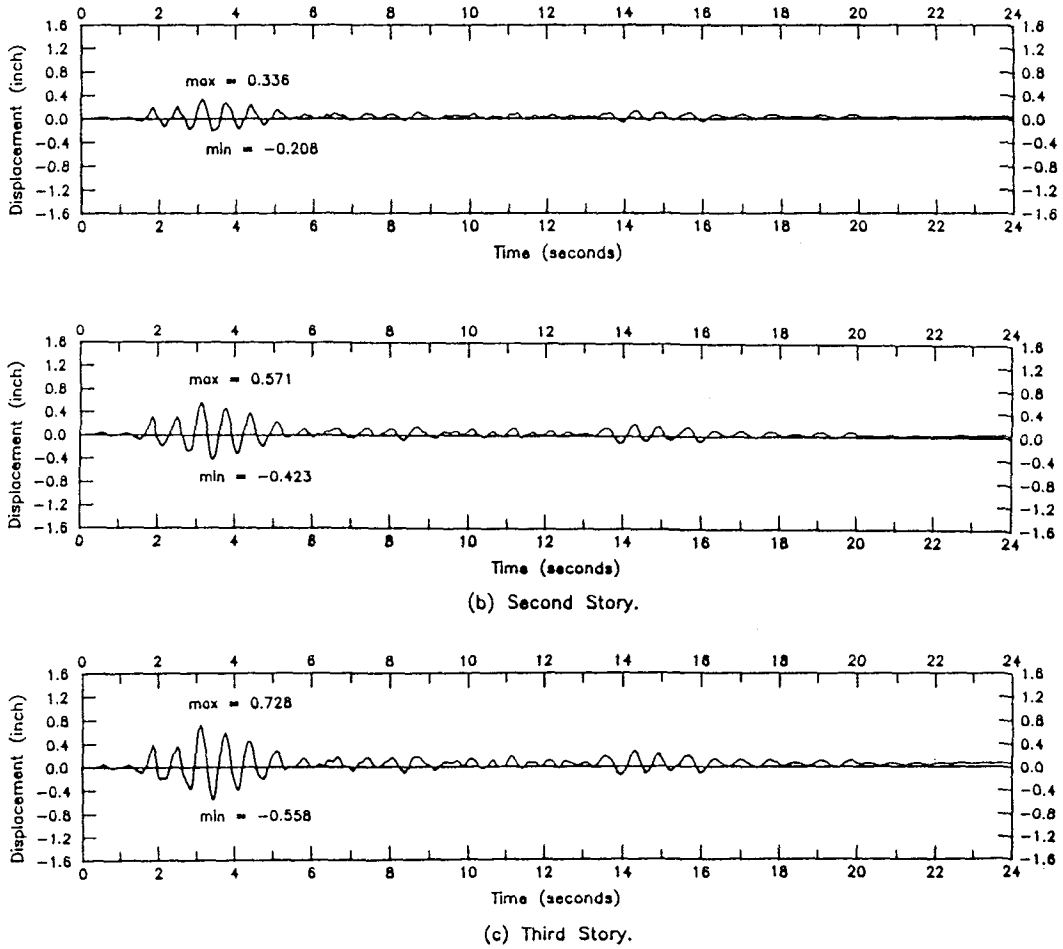


Figure 3.8: Story Displacements (Run Taft 0.18-G).

Table 3.4: Ratio of Internal to External Column Shear

| Test | $\frac{\textit{Average Internal Column Shear}}{\textit{Average External Column Shear}}$ | |
|---|---|---|
| | First Story | Second Story |
| Taft 0.05 g | 1.919 | 1.537 |
| Taft 0.18 g | 1.780 | 1.574 |
| Taft 0.35 g | 1.920 | 1.510 |

indicates that the two devices were functioning properly, and the load cells were accurately aligned with the direction of motion. It will be shown in subsequent runs that, as the model deformations increase, the P-$\Delta$ effect will disturb this agreement between the load-cells and the acceleration based story shears.

All structural components (columns, beams, and joints) were well below their yield point during this run. Although a few hair cracks were observed in the joint region, no significant changes in the model natural frequencies were detected after this run indicating that the model was still in the elastic range. In discussing the subsequent runs, more attention will be given to the local response of the aforementioned structural components as they approach higher stages of loading.

## 3.5 Run Taft 0.18-G

### 3.5.1 Global response

#### Model deformation

Story displacements during this run are presented in figures 3.8.a through 3.8.c for the first, second, and third stories respectively. It can be seen that the model

Table 3.5: Maximum Deformations During Seismic Tests

| Test | Maximum Story Displacement (inches) | | | Maximum Inter-Story Drift % | | |
|---|---|---|---|---|---|---|
| | $1^{st}$ Story | $2^{nd}$ Story | $3^{rd}$ Story | $1^{st}$ Story | $2^{nd}$ Story | $3^{rd}$ Story |
| Taft 0.05 g | 0.033 | 0.055 | 0.070 | 0.18 | 0.13 | 0.10 |
| Taft 0.18 g | 0.336 | 0.571 | 0.728 | 1.87 | 1.35 | 1.02 |
| Taft 0.35 g | 0.474 | 0.824 | 1.024 | 2.63 | 1.96 | 1.55 |

deformations during this run were much higher than those recorded during the previous run for all stories, with a maximum top story displacement of 0.728" (1.3% drift) which is about 10 times that of run Taft 0.05 g. Similar figures are found for the first and the second stories (table 3.5). Despite the much higher model flexibility, the mode shape at the moment of maximum base shear was very close to that of run Taft 0.05 g (figure 3.3), indicating that the model response was still dominated by its first mode of vibration. The same conclusion can be reached by inspecting the story displacements time-history, where it can be observed that all stories were moving in phase, with their peak values occurring at the same time.

Most of the model deformation occurred during the first 4 seconds of the seismic test as shown in figure 3.8. This observation suggests a significant change in the model properties during that period, especially its damping ratios. As the free-vibration test was carried out after this run (table 3.2), it was found that the damping ratio corresponding to the first mode of vibration increased from 1.3% to

Table 3.6: Maximum Story Shears During Seismic Tests

| Test | Maximum Story Shear (kips) | | |
|---|---|---|---|
| | $1^{st}$ Story | $2^{nd}$ Story | $3^{rd}$ Story |
| Taft 0.05 g | 0.338 | 0.273 | 0.185 |
| Taft 0.18 g | 1.252 | 1.110 | 0.816 |
| Taft 0.35 g | 1.384 | 1.297 | 1.063 |

2.74%, and the fundamental frequency of the model decreased from 2.2 Hz to 1.8 Hz during this run.

### Story shears

Figure 3.9 shows the time history of the story shears recorded during this run. The base shear showed a maximum value of 1.252 kips (8.34% of the model weight), while the second and the third stories showed maximum values of 1.134 kips and 0.816 kips respectively (table 3.6). It was observed during this run that, relative to the base shear, the second and third stories were subjected to a higher shearing force than that of the previous run. Figure 3.3 indicates that at the moment of maximum base shear, the second and the third stories were subjected to 86% and 46% of the maximum base shear, in contrast to 63% and 32% recorded for run Taft 0.05 g. Since the mode shape at the maximum base shear was almost the same for both runs (figure 3.3), it was concluded that the relative increase in the top two stories shear results from the softening (stiffness degradation) of the first story.

As previously observed for the story displacements, most of the story shears

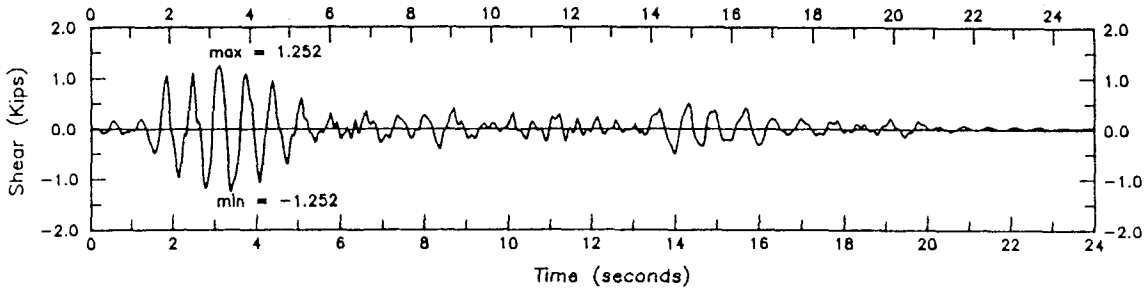


(a) Base Shear.

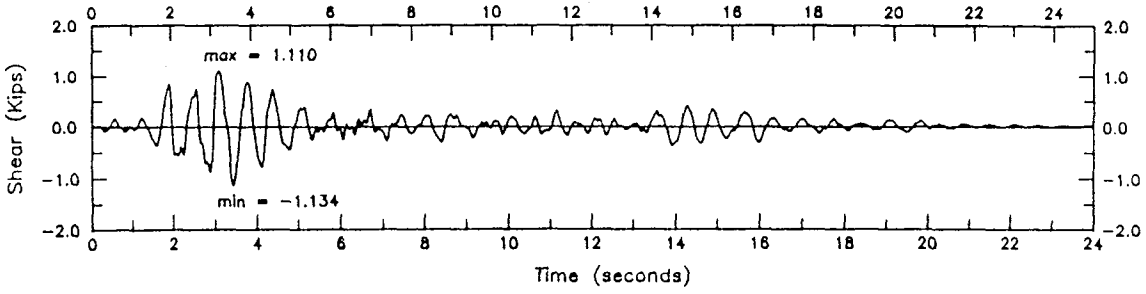


(b) Second Story.

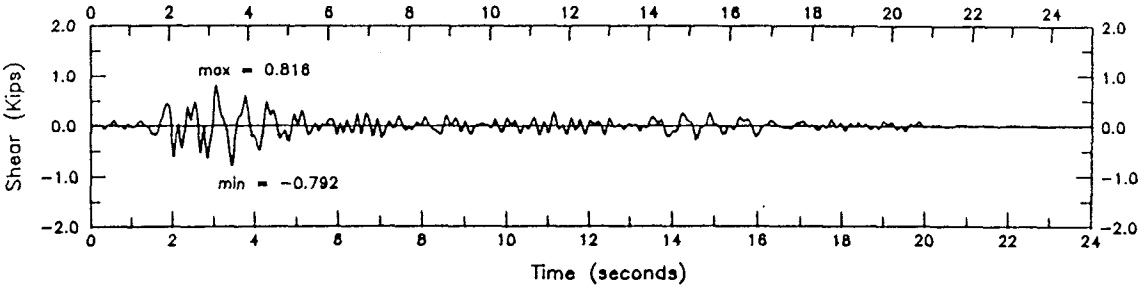


(c) Third Story.

Figure 3.9: Story Shears (Run Taft 0.18-G).

occurred during the first 4 seconds of the seismic test. The low shear force levels recorded for the rest of the test reflect the fact that both the model natural frequencies and damping ratios changed significantly.

### Story Stiffness and energy dissipation

Story shears are plotted against inter-story drifts in figures 3.10.a through 3.10.c for the first, second and third stories respectively. Initial and average story stiffness were obtained by performing a linear regression of the first 150 points and all points of the hysteresis loop respectively. The large differences between the initial and the average story stiffness indicate the strong non-linear effects produced by the 0.18 g run. Despite the differences in their initial stiffness, all three stories had almost the same average stiffness during this run, as stiffness values of 4.83, 5.16, and 4.95 kips/in were recorded for the first, second and third stories respectively (table 3.7). These values represented stiffness reductions of 50%, 55%, and 50% for the first, second and third stories respectively, as compared to those of the previous run.

Integration of the hysteresis loops of figure 3.10 can provide a rough estimation of the energy dissipated by each story. The integration results are shown in figure 3.11.a and 3.11.b, where it can be seen that most of the energy (85%) was dissipated during the first five seconds of the seismic test. The first, second, and third stories dissipated 54%, 33%, and 13% of the total energy respectively, emphasizing the fact that the first story was subjected to the most structural damage during this run.

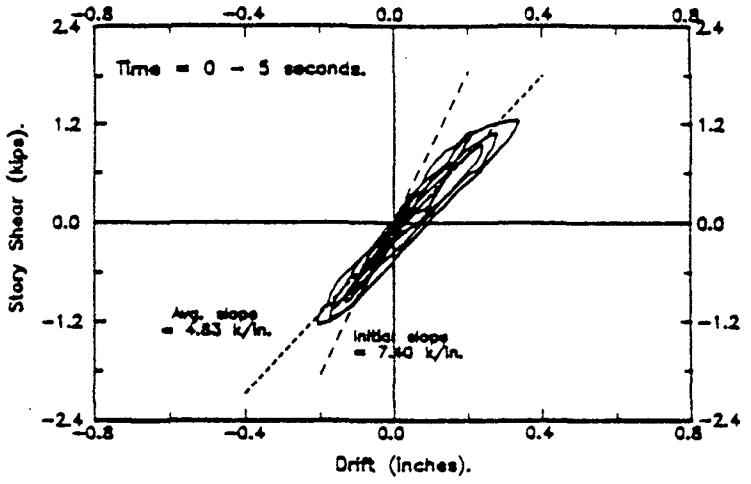


(a) First Story.

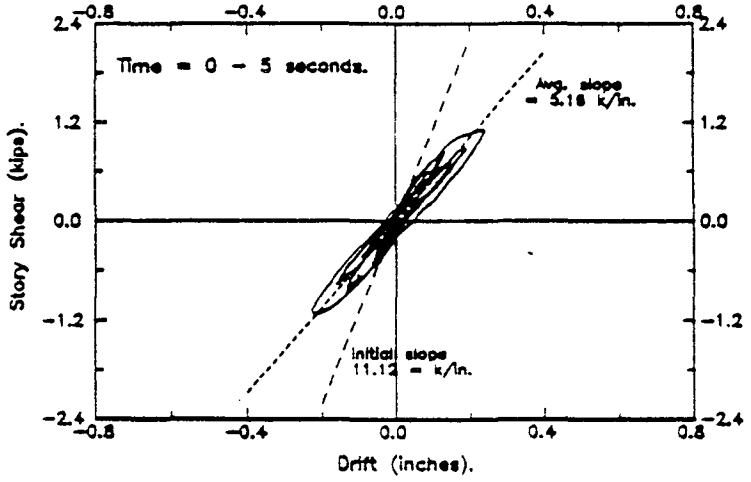


(b) Second Story.

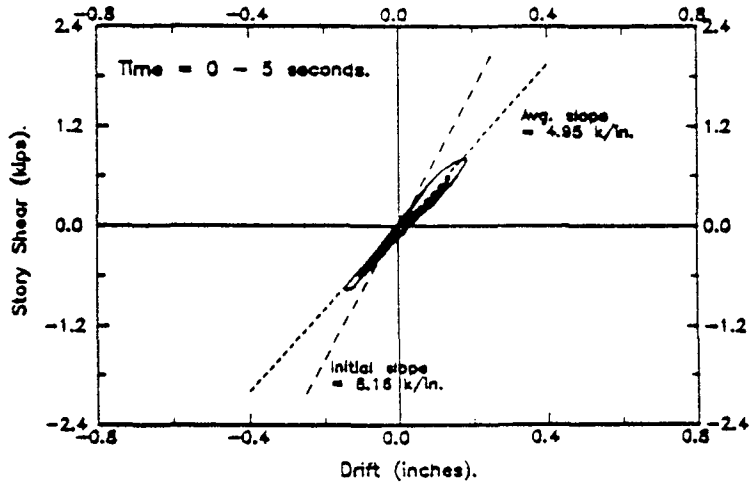


(c) Third Story.

Figure 3.10: Story Shear Versus Inter-Story Drift Hysteresis Curves (Run Taft 0.18-G).

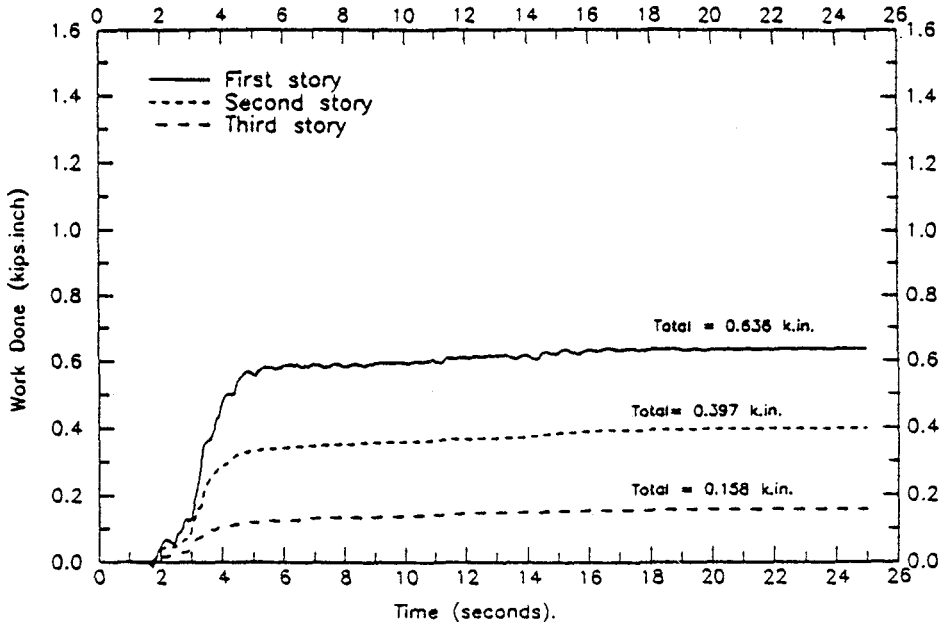


(a) Energy Dissipated by Each Story.

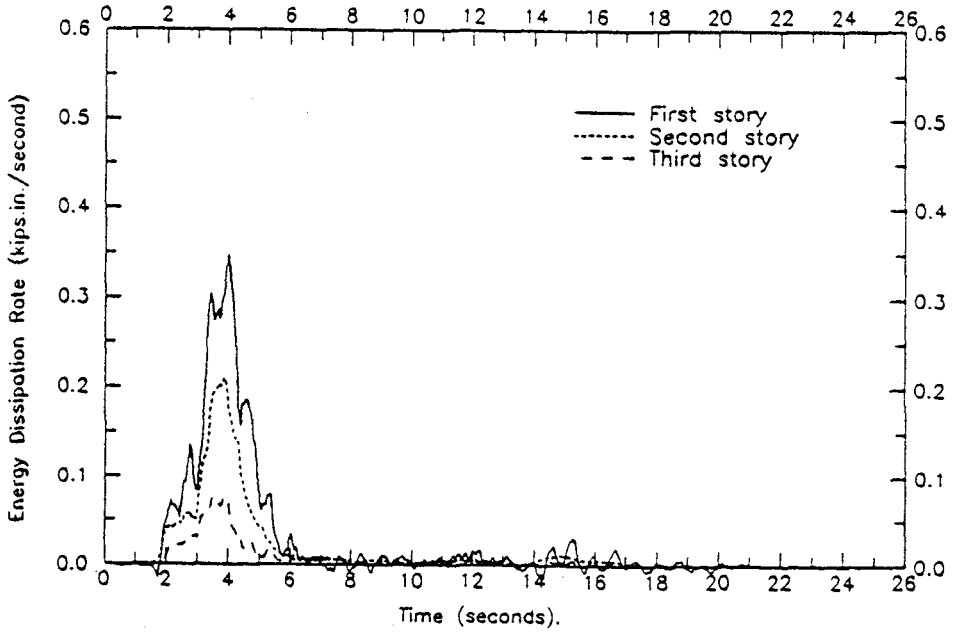


(b) Change of Energy Dissipation Rate With Time.

**Figure 3.11: Energy Dissipation (Run Taft 0.18-G).**

Table 3.7: Average Story Stiffness During Seismic Tests

| Test | Average Story Stiffness (kips/inch) | | |
|---|---|---|---|
| | $1^{st}$ Story | $2^{nd}$ Story | $3^{rd}$ Story |
| Taft 0.05 g | 9.68 | 11.57 | 10.01 |
| Taft 0.18 g | 4.83 | 5.16 | 4.95 |
| Taft 0.35 g | 4.12 | 3.91 | 4.11 |

### 3.5.2 Local response

#### Columns

The shear force time-histories of the first and the second story columns are shown in figures 3.12 and 3.13 respectively. Both figures indicate that symmetric columns displayed essentially the same shearing forces during the seismic test. For the first story, the ratio of internal to external columns maximum shearing force was reduced from 1.92 (recorded for run Taft 0.05 g) to 1.78 for the present run, indicating a relative reduction in interior column stiffness. No change in this ratio was detected for the second story during this run.

Unlike the previous run, the maximum base shear obtained by summing the column shears was 27% larger than that derived from the acceleration measurements. The difference was mainly attributed to the large P-$\Delta$ effect associated with testing the bare frame without infill walls. The maximum first story column shear force estimated by calculating the component of the building weight acting in the perpendicular direction to the columns axes and adding it to the story shears

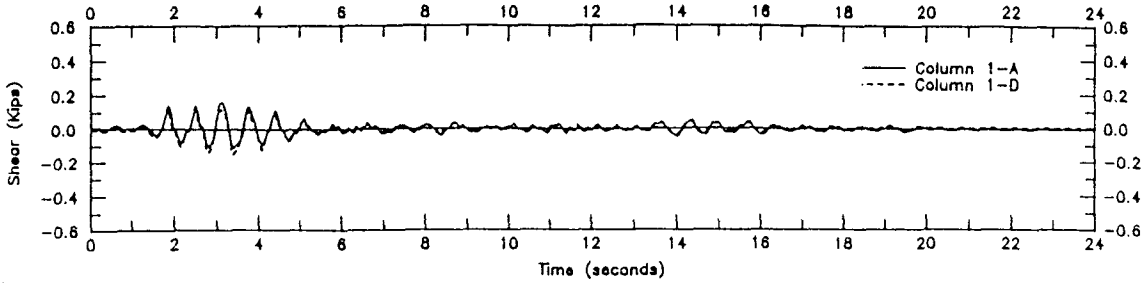


(a) Exterior Columns.

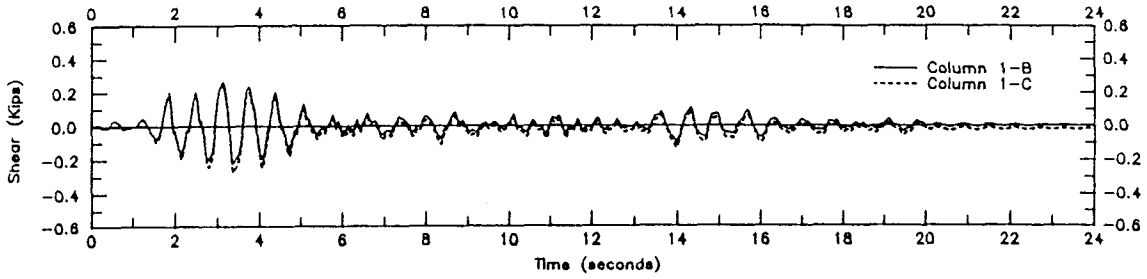


(b) Interior Columns.

Figure 3.12: First Story Columns Shear (Run Taft 0.18-G).

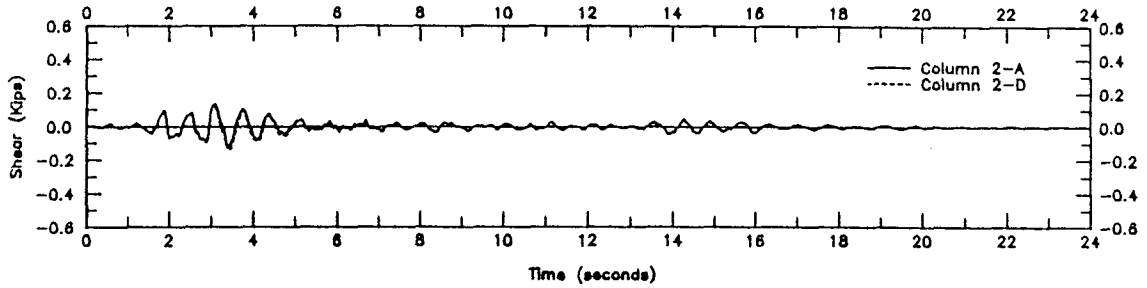


(a) Exterior Columns.

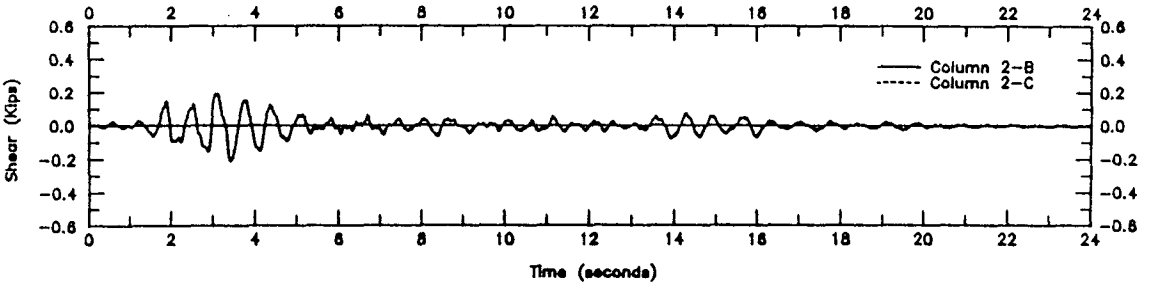


(b) Interior Columns.

Figure 3.13: Second Story Columns Shear (Run Taft 0.18-G).

obtained from the acceleration measurements (figure 3.14). The discrepancy between the load cell and the story acceleration shears was reduced to 4% according to these calculations.

Column shears are plotted against inter-story drifts in figures 3.15 and 3.16 for the first and the second story columns respectively. It can be seen that the response of all columns showed significant non-linearities. The first story columns hysteresis loops were not symmetric due to the non-symmetric table excitation, and to the continuously changing model properties. However, symmetric hysteresis curves were obtained for the second story columns as they were subjected to a nearly harmonic motion. Relatively flat portions of the hysteretic curves corresponding to onset of yielding were detected for all first and second story columns except columns 1-B, 2-B, and 2-C.

The average slopes of the hysteresis loops indicate the large difference in stiffness between interior and exterior columns, emphasizing the contribution of the column axial force to its shear capacity (more discussion on this issue is provided in section 5.3.2). It was also observed that exterior column hysteresis loops have different slopes for positive and negative drifts, reflecting the fact that their axial forces were highly affected by the over-turning moments. This phenomenon was not observed for the interior columns, since the change in their axial forces due to over-turning moment effects was insignificant.

The moment-normal force interaction curves for two first story columns are shown in figures 3.17 and 3.18. Cracking and yield surfaces based on static properties of concrete and steel are also presented on the same plot for each column.

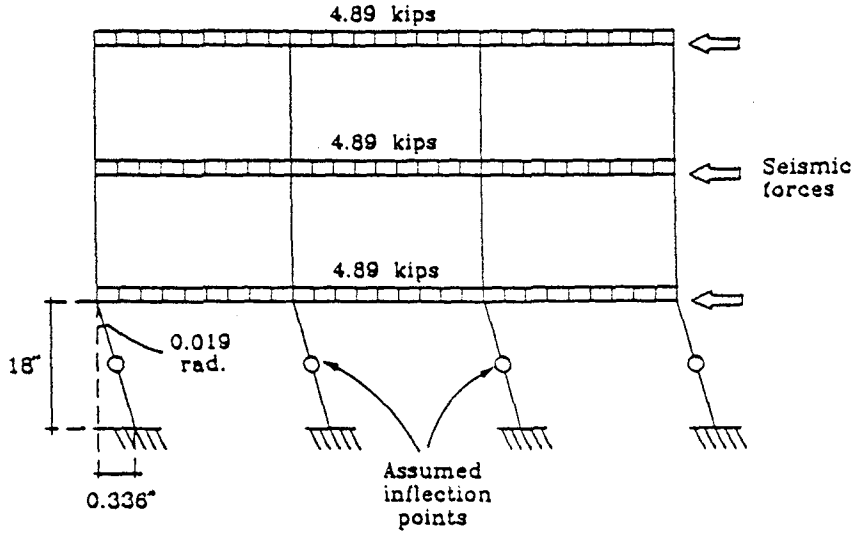


(a) Idealized Model Deformations.

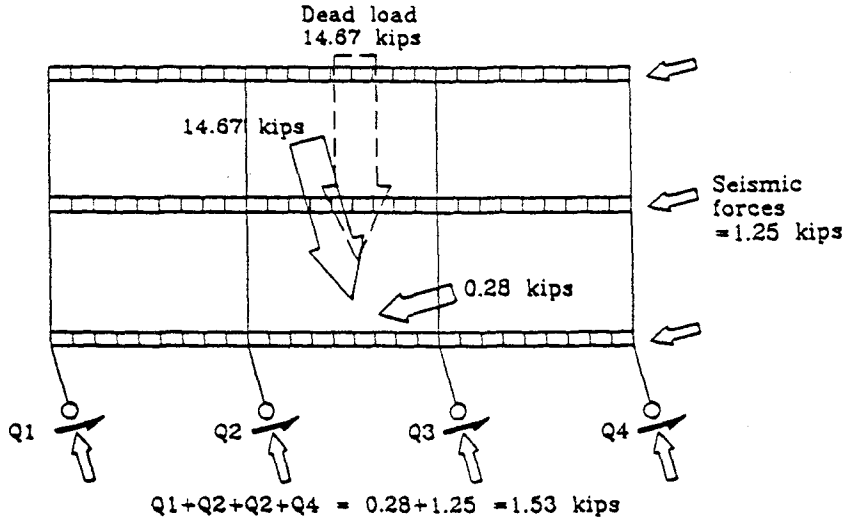


(b) Column Shear Forces.

Figure 3.14: Simplified Computation of The P-$\Delta$ Effect on The Frist Story Columns (Run Taft 0.18-G).

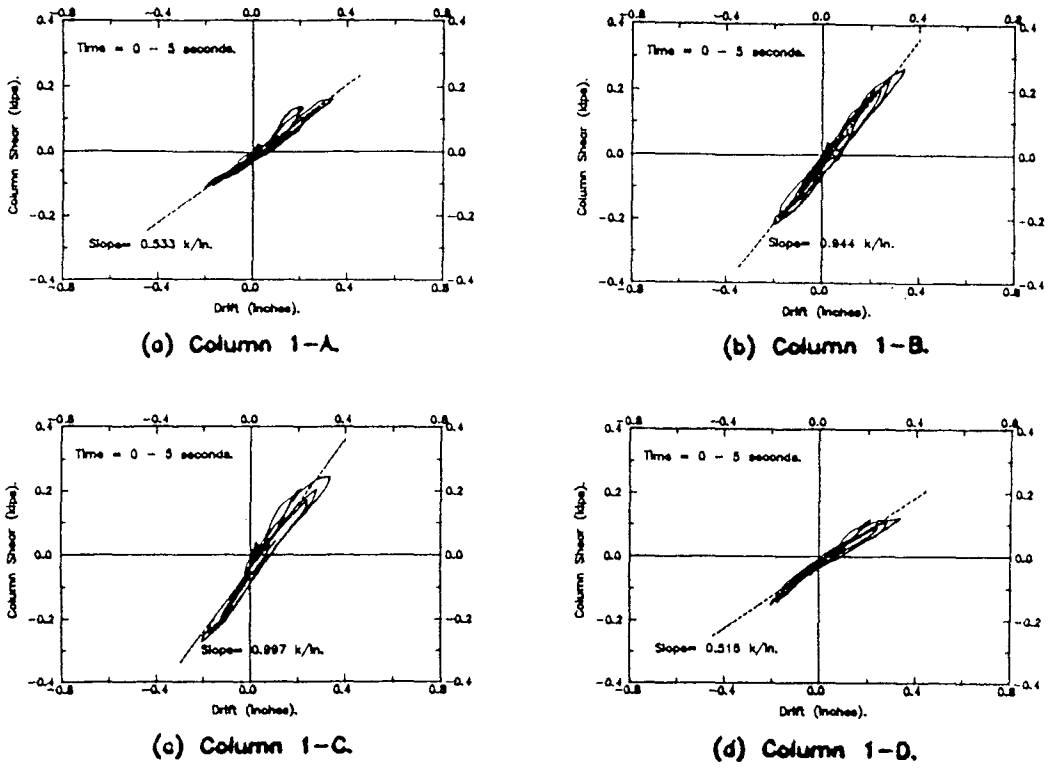


Figure 3.15: First Story Shear-Drift Hysteresis Curves (Run Taft 0.18-G).

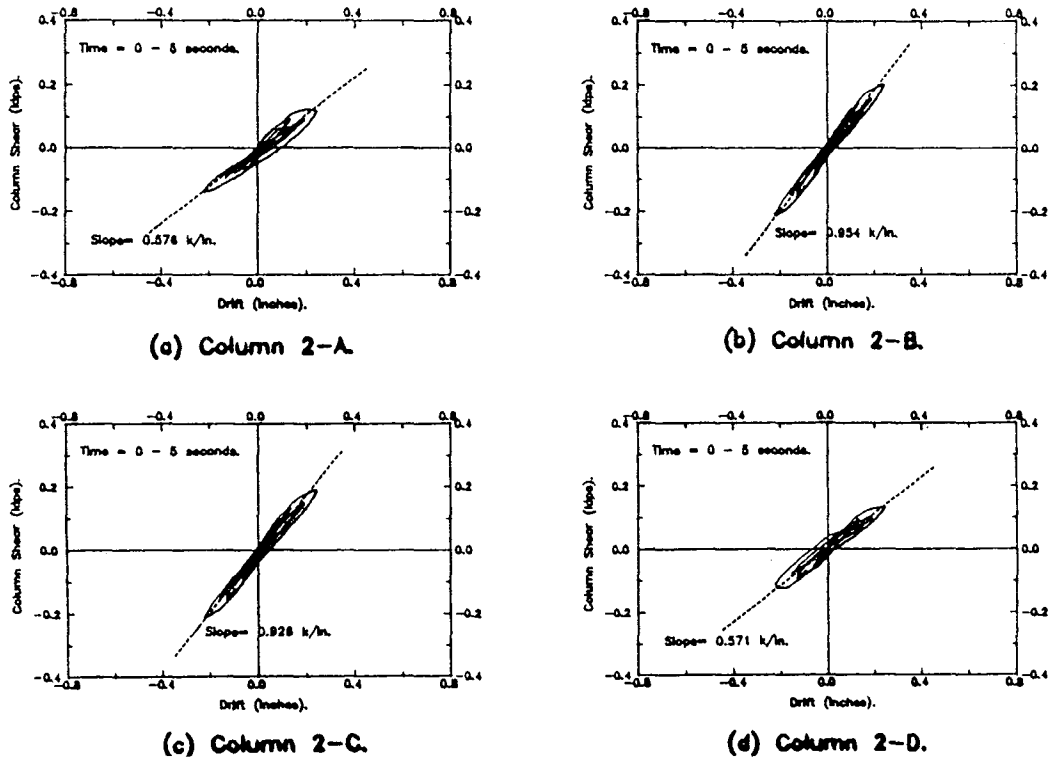


Figure 3.16: Second Story Shear-Drift Hysteresis Curves (Run Taft 0.18-G).

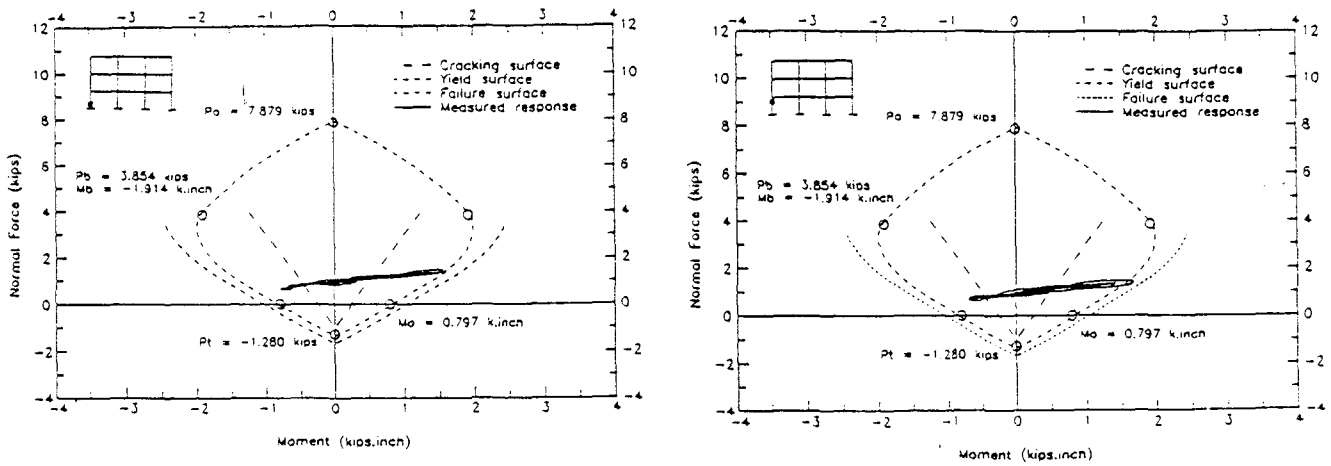


(a) Bottom Section. (b) Top Section.

Figure 3.17: Moment-Normal Force Response of Column 1-A (Run Taft 0.18-G).

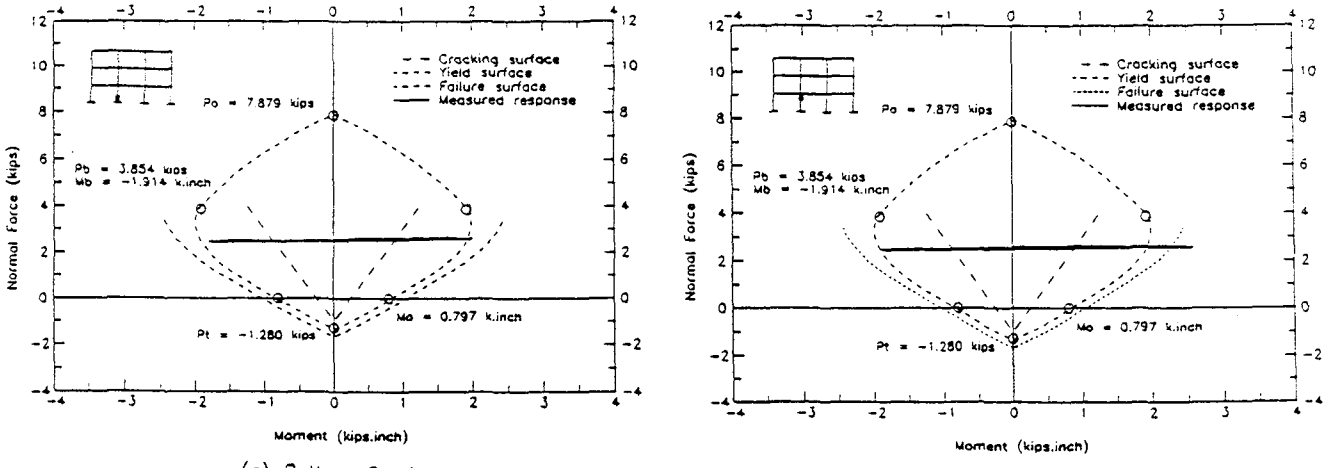


(a) Bottom Section. (b) Top Section.

Figure 3.18: Moment-Normal Force Response of Column 1-B (Run Taft 0.18-G).

All columns were cracked during this run as their interaction curves exceeded their cracking envelopes. Also, the first story columns yielded at least in one direction as shown in figures 3.17 and 3.18. It was noticed that the interaction curves exceeded the yield surface in columns 1-B and 1-C, indicating an overstrength of these columns. Overstrength of concrete components during cyclic tests has been reported by other investigators [10] where it was attributed to factors such as (a) the increase in the concrete strength and its maximum strain capacity due to the strain gradient and confinement of concrete, (b) the fact that steel reinforcement is likely to reach higher stresses in a column than in a tensile coupon because the smaller length under maximum tension in a column is not likely to have a weak "link" that limits the strength in a coupon tension test, (c) the increase in the concrete and steel strengths due to the strain rate effects, especially for smaller scale models where the loading rate is increased due to the time compression, and (d) the strain hardening of model reinforcement, especially for a highly flexible model like the present one. The failure surface of the model columns is approximated by the dashed curves in figures 3.17 and 3.18. In those curves, the ultimate steel stress of 55 ksi was used instead of the yield stress of 42 ksi, and the concrete compressive strength $f_c^{'}$ was also increased by 25% [16] to account for the loading rate effects.

The second story columns barely reached yield during this run, with a damage level less than that of the first story columns. Visual inspection of these columns supported this observation as less cracking was observed at the second story columns.

### Beams

The bending moments at the critical sections of the first story longitudinal beam were obtained using both the static reactions on the columns measured before the seismic test and the changes in those reactions recorded during the table excitation. The time-histories of these moments are presented in figures 3.19.a through 3.19.f for sections B1 to B6 respectively (figure 2.1a). Cracking and yielding moments are also shown on the same plot for each section.

Inspection of the moment traces of sections B1 and B6 indicates that the two sections showed close response during this run, with the beam cracked in both the positive and the negative directions in both sections. It can be observed that the discontinuous bottom beam reinforcement reached its yield point once during the entire run for each section. The negative reinforcement over the support remained well below its yield point through this run. No sign of discontinuous steel pullout was detected at these two sections.

Sections B2 and B5 were already cracked under the floor's own weight. As the seismic test excitation was applied, the change in the bending moments at section B2 was not enough to yield the beam reinforcement in either direction, or even to crack it in the positive direction. The response of section B5 was quite different, where it cracked and yielded in both directions. Again for these two sections, the discontinuous positive beam reinforcement did not pullout of the columns during this run. This result was also confirmed by the visual inspection of the two sections after the seismic test. Among the reasons that could have contributed to the difference in the response of sections B2 and B5 are (a) the accidental overstrength

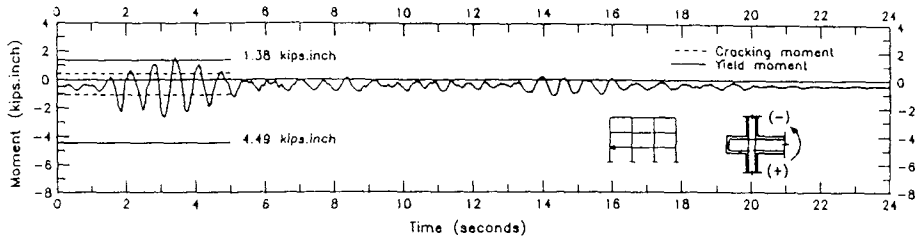


(a) Section B1.

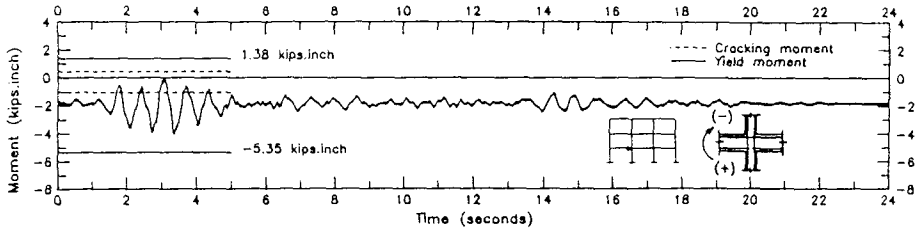


(b) Section B2.

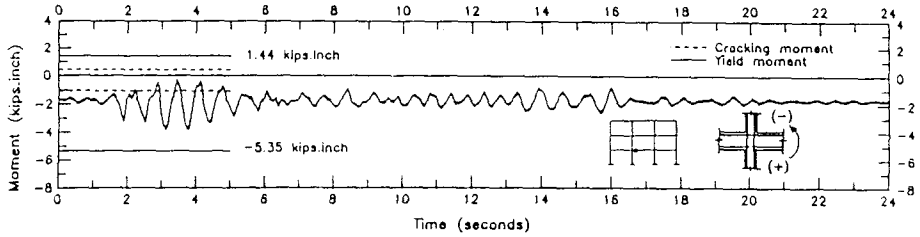


(c) Section B3.

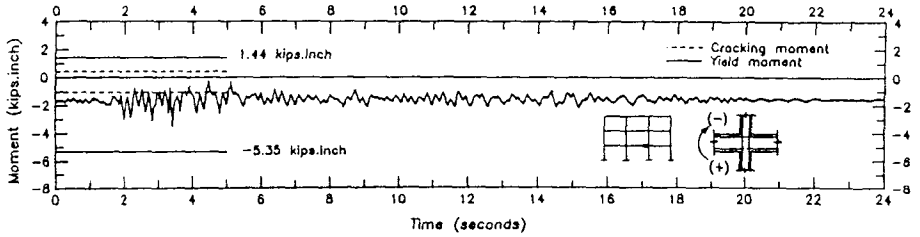


(d) Section B4.

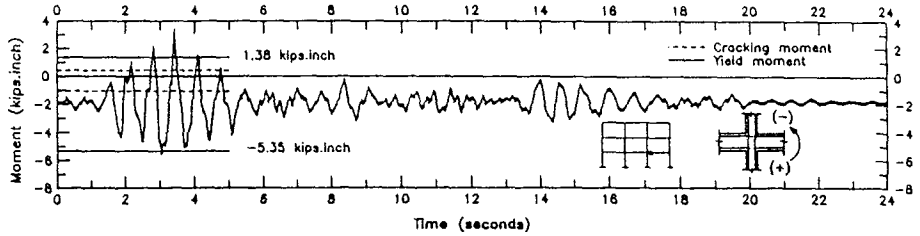


(e) Section B5.

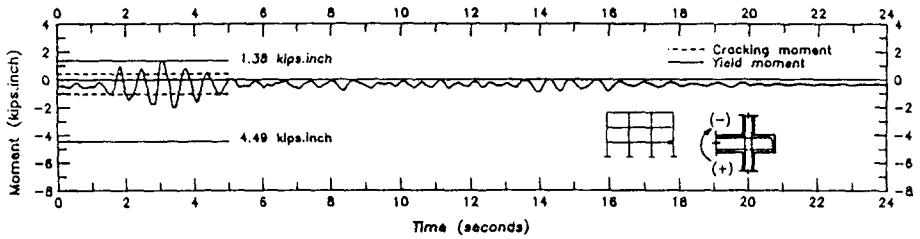


(f) Section B6.

Figure 3.19: **Bending Moments of The First Story Longitudinal Beams (Run Taft 0.18-G).**

of section B5 due to the difficulty associated with controlling the slab thickness, and (b) the dependence of the bending moments at both sections (B2 and B5) on the change in the exterior columns axial force which might contain some errors.

The response of sections B3 and B4 was very similar to that of section B2, where both sections were cracked under static loads, and were subjected to a relatively small change in their moments due to the seismic tests. Figures 3.19.c and 3.19.d show that both sections were not subjected to any positive moment during the entire run and did not yield in the negative direction either. As would be expected, no pull-out of the discontinuous positive beam reinforcement occurred at these two sections.

The longitudinal frame bending moment diagrams are shown in figures 3.20.a and 3.20.b for the maximum positive and the maximum negative base shears respectively. These moments were obtained by superposing the static bending moment diagram recorded before the seismic test and the bending moments measured during the test. It can be seen that external column moments were highly affected by the over-turning moments. In the case of maximum positive base shear for example, the over-turning moments increased the axial force on axis A columns (1-A and 2-A), and decreased it on line D columns (1-D and 2-D). This was directly reflected in the high bending moments in line A columns compared to those of line D columns. This phenomenon was less pronounced in interior columns as shown in figure 3.20.a. The same observation was true for maximum negative base shear as shown in figure 3.20.b.

The bending moments on sections B3 and B4 of the first story interior beam

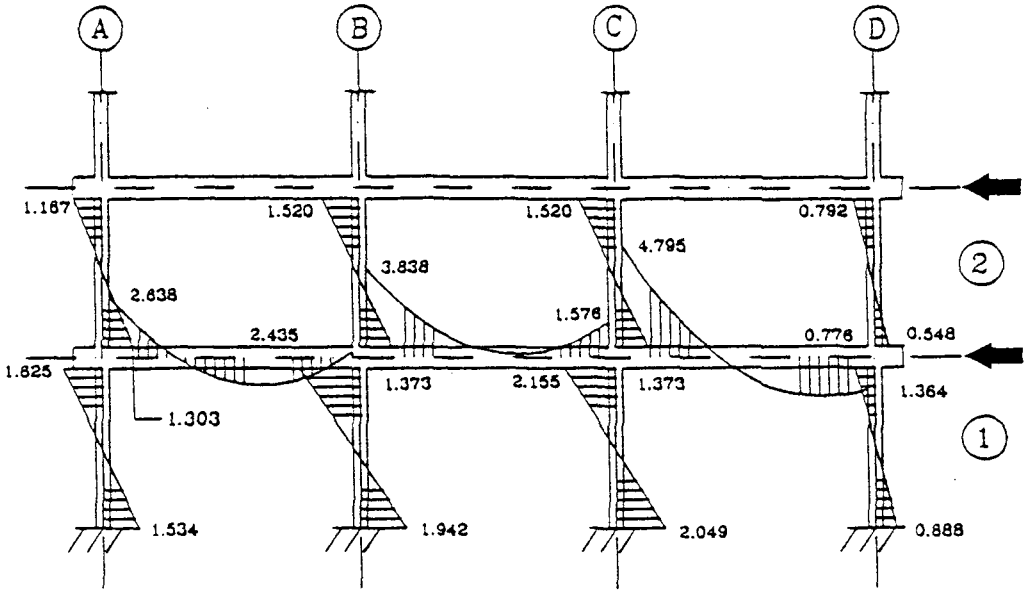


(a) Bending Moments at The Maximum Positive Base Shear.
(Time = 3.11 seconds)

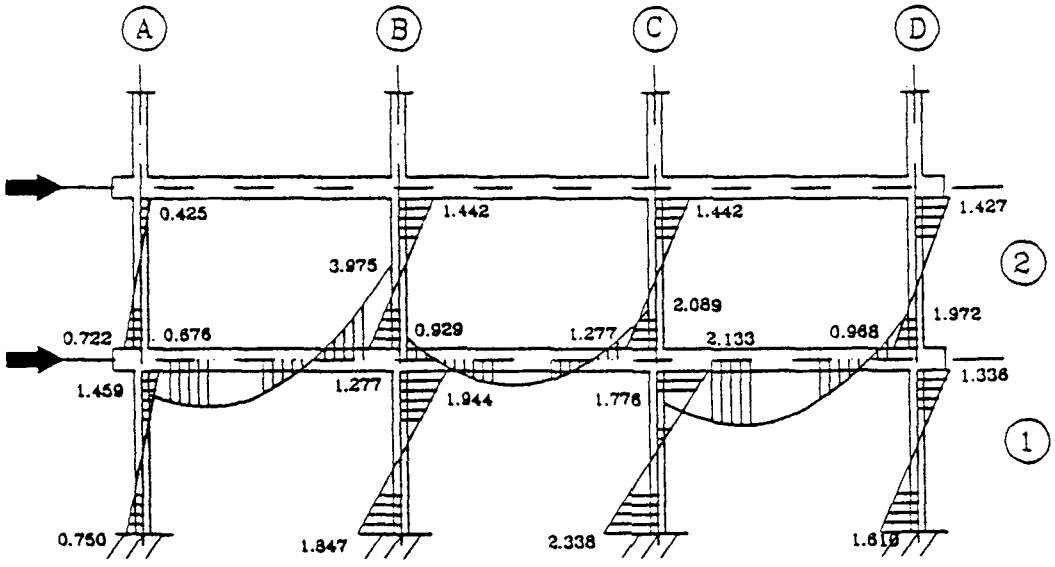


(b) Bending Moments at The Maximum Negative Base Shear.
(Time = 3.37 seconds)

Figure 3.20: **Bending Moments at The Maximum Base Shear (Run Taft 0.18-G).**

were always negative, eliminating the possibility of discontinuous bottom reinforcement pull-out. In exterior beams, positive moments were developed at sections B6, B1, and B5, with only B5 exceeding its static yield point (figure 3.20.e). It was also important to notice that post-test inspection showed that all three sections were not subjected to any significant damage.

## 3.6 Run Taft 0.35 g

### 3.6.1 Global response

#### Model deformation

The model structure displayed large deformations during this run as the top story drift recorded a maximum value of 1.024" corresponding to 1.93% of the model height. The maximum story displacements were 41%, 44%, and 40% higher than those of the previous run for the first, second and third stories respectively (table 3.3). Despite the large deformations, the three stories were still moving in phase, with their peak values occurring at the same time, indicating the domination of the first mode of vibration. The mode shape at the moment of maximum base shear was similar to that of the previous run, suggesting that the model was deforming in the same manner despite its strong non-linearities (figure 3.3).

Unlike the previous test, the model experienced significant deformation during the entire seismic excitation time (20 seconds) as shown in figures 3.21.a, b, and c. This observation is attributed to smaller changes in the model properties during this run than during the previous run. Table 3.2 indicates that (a) the reduction in the fundamental frequency due to the current run was 8.8% versus 18.2% recorded

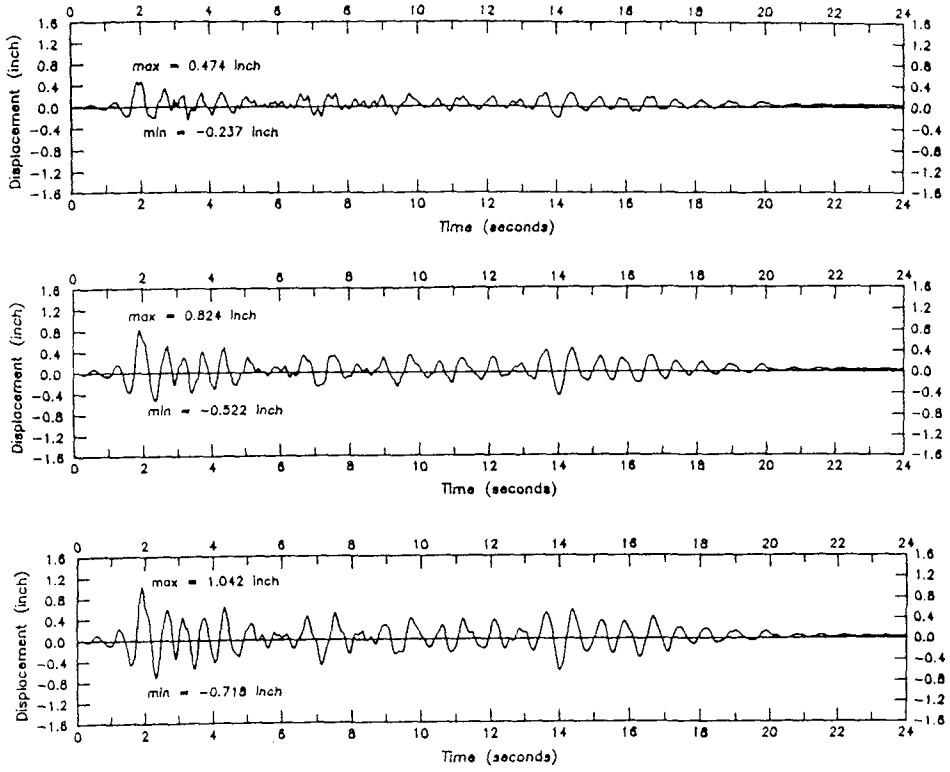


Figure 3.21: Story Displacements (Run Taft 0.35-G).

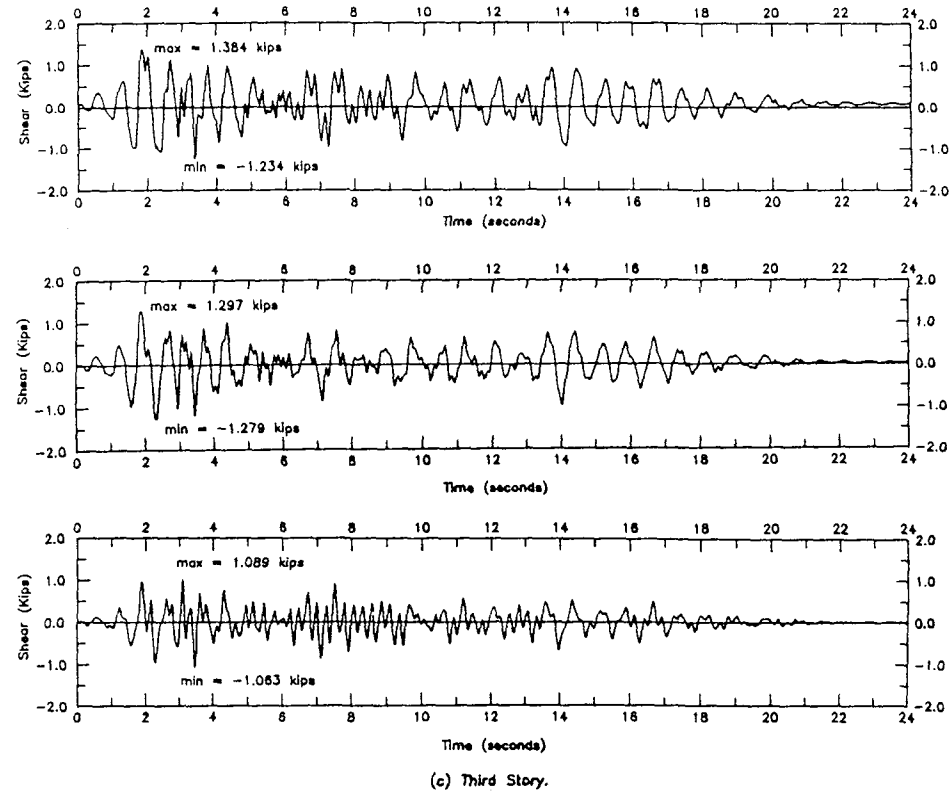


Figure 3.22: Story Shears (Run Taft 0.35-G).

during run Taft 0.18 g, and (b) the change in the damping ratios due to the present run were very minor as compared to that of the previous run. Further discussion of this point will be presented in the following section.

### Story shears

The time-histories of the story shears are shown in figure 3.22 for all three stories. It can be seen that the base shear recorded a maximum value of 1.384 kips corresponding to 9.4% of the total weight of the building. Compared to the previous run, the maximum story shears were 10.5%, 16.8%, and 30.3% higher than the maximum values recorded during the previous run for the first, second and third stories respectively. The non-uniform increase in the maximum story shears is directly related to the softening of the first story with respect to the second and the third stories. This point is emphasized even more as the story shears at the instant of maximum base shear presented in figure 3.3 are inspected. It can be seen that although the mode shape of the structure was almost the same for all three seismic tests, the percentage of the second and third story shears (with respect to the base shear) increased as the model deformation increased.

It can be observed from figure 3.22 that all three stories experienced large shear forces during most of the entire seismic excitation (20 seconds). This may be due to the relatively smaller changes in the model properties (particularly in damping ratios) during this run as compared to the changes recorded during the previous run (table 3.2).

### Story stiffness and energy dissipation

The two measures used to investigate the change in the story stiffness during the

seismic test were (a) the flexibility matrix coefficients obtained from the static test, and (b) the average slope of the (story shear)-(inter-story drift) hysteresis loops. It is believed that the second measure provides a more realistic estimation of the story stiffness since it covers a larger range of story forces and inherently includes the loading rate effects. On the other hand, in the static test, a static force of a maximum value of 150 lb is used (in increments of 50 lb) at each floor level to determine the flexibility matrix coefficients.

It can be seen from table 3.7 that the average slopes of the first, second and third story hysteretic curves were less than those obtained for run Taft 0.05 g by 64.4%, 59.6%, and 58.9% respectively, indicating that model was significantly damaged, especially at the first story. It can also be observed from table 3.7 that the stiffness reduction due to the current run was significantly less than that caused by the previous run, indicating that most cracks were developed during the previous run. This observation was reflected in the way the model dissipated energy during this run.

The total energy dissipated by the model during this run was 2.55 times that of the previous run. As shown in figure 3.24.a, the first story dissipated a large proportion of this energy (45.2%), while the second and the third stories dissipated 31.7%, and 23.1% of the total energy respectively. Comparing these figures to those of the previous run (table 3.8), it can be observed that the contribution of the upper two stories to the total energy increased during this run as they showed a high degree of plasticity manifested in their broader hysteresis loops (figures 3.23.b and c). Comparing figures 3.11.b and 3.24.b, it can be seen that the energy dissipation

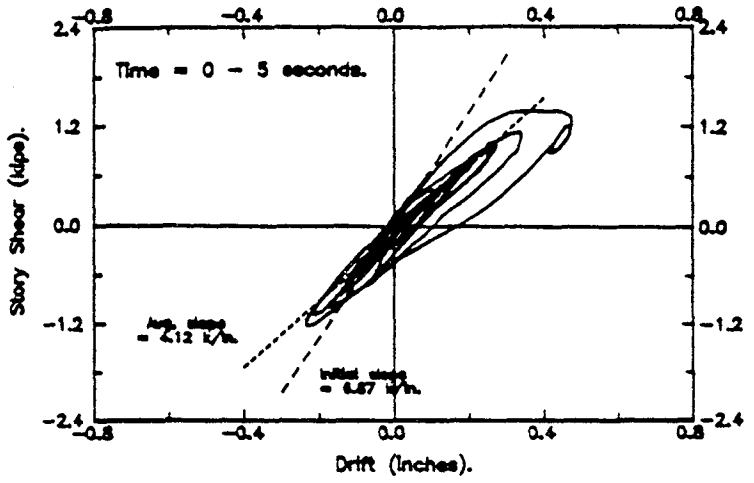


(a) First Story.

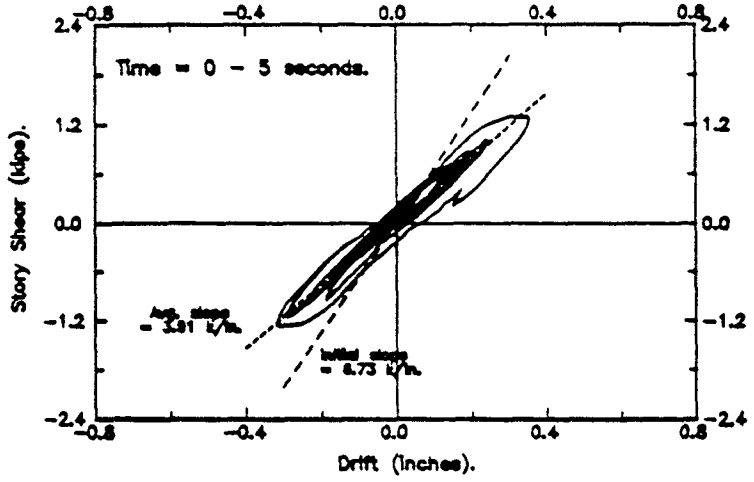


(b) Second Story.

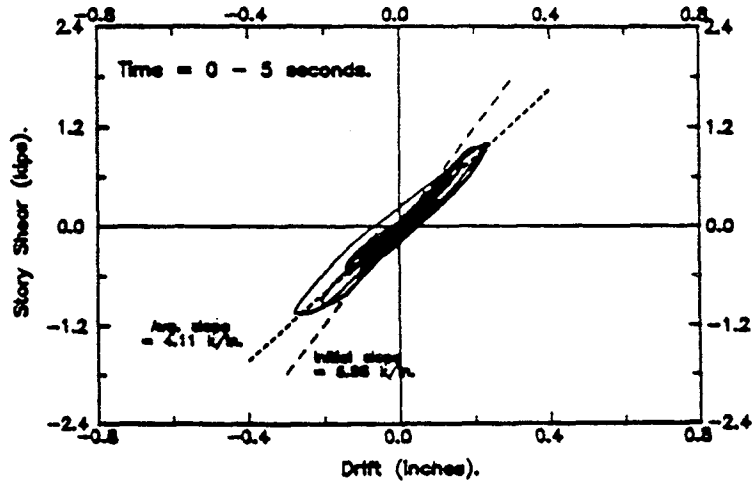


(c) Third Story.

Figure 3.23: Story Shear Versus Inter-Story Drift Hysteresis Curves (Run Taft 0.35-G).

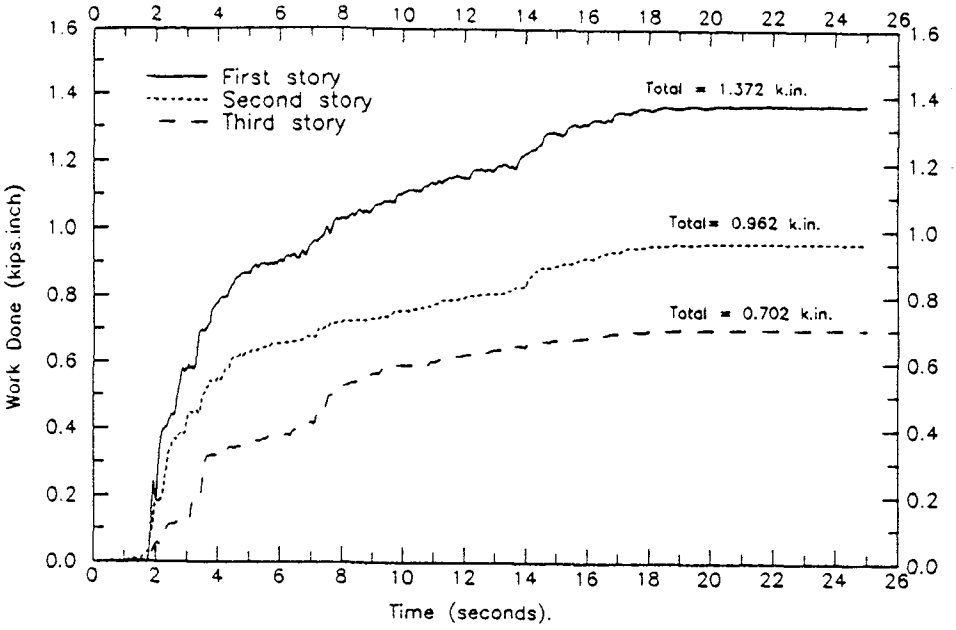


(a) Energy Dissipated by Each Story.

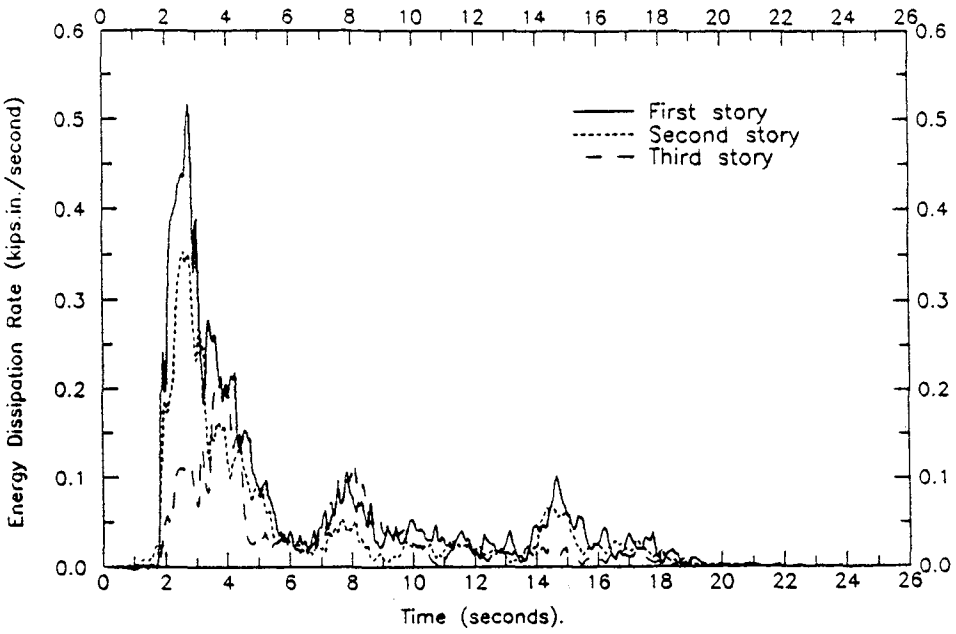


(b) Change of Energy Dissipation Rate With Time.

**Figure 3.24: Energy Dissipation (Run Taft 0.35-G).**

Table 3.8: Approximate Energy Dissipation During Seismic Tests

| Test | Energy Dissipated ($kips \times inch$) | | | |
|---|---|---|---|---|
| | $1^{st}$ Story | $2^{nd}$ Story | $3^{rd}$ Story | Total Energy |
| Taft 0.05 g | — | — | — | — |
| Taft 0.18 g | 0.636 | 0.397 | 0.156 | 1.189 |
| Taft 0.35 g | 1.372 | 0.962 | 0.702 | 3.036 |

occurred more uniformly over the test duration for the current run, as the energy dissipated during the first five seconds represented only 61% of the total energy (in contrast to 85% recorded for the previous run). In fact, it took the model 12.43 seconds to dissipate 85% of the total energy dissipated during this run. This observation suggests that the change in the model properties during this run was of a more gradual nature, associated with phenomena such as crack propagation, steel yielding, and bond deterioration. On the other hand, the generation of new cracks was the major reason for the sudden change in the model properties during the previous run.

### 3.6.2 Local response

#### Columns

The shear forces in the first and the second story columns are shown in figures 3.25, and 3.26 respectively. It can be seen from both figures that symmetric columns were subjected to nearly similar shearing forces during the entire run. The ratio of internal to external column shears was 1.92 for the first story and 1.54 for the

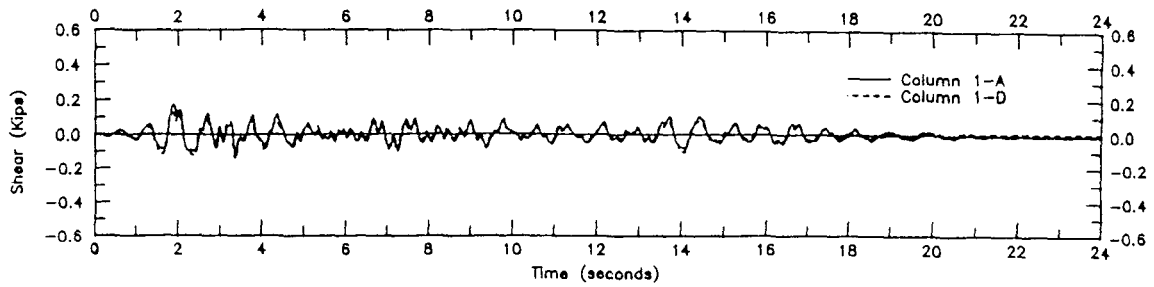


(a) Exterior Columns.

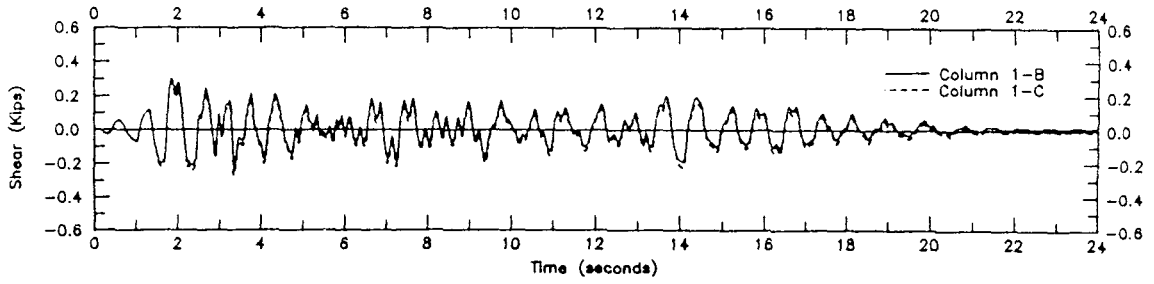


(b) Interior Columns.

Figure 3.25: First Story Columns Shear (Run Taft 0.35-G).

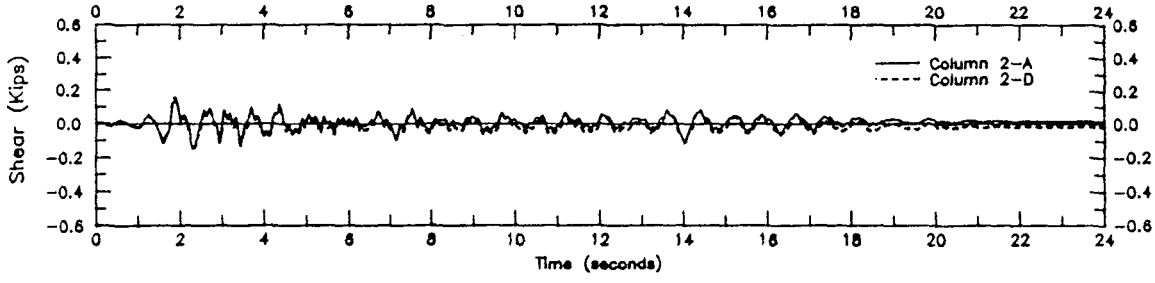


(a) Exterior Columns.

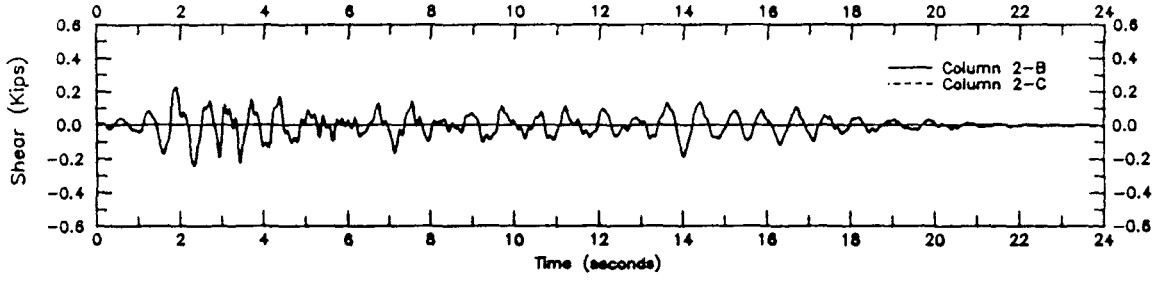


(b) Interior Columns.

Figure 3.26: Second Story Columns Shear (Run Taft 0.35-G)

second story as shown in figure 3.4. As previously observed for run Taft 0.18 g, the maximum base shear obtained from the load cell readings was 27% higher than that obtained from the acceleration measurements. The difference is referred to the large P-$\Delta$ effect resulting from testing the bare frame.

The shear force-inter-story drift hysteresis curves are shown in figures 3.27 and 3.28 for the first and the second stories respectively. It can be seen from all curves that larger areas were enclosed by the hysteretic curves than those recorded during the previous run, indicating higher energy dissipation. Large flat portions of the hysteresis curves corresponding to steel yielding were observed in most columns. Inspection of the average slopes of the hysteresis loops indicates that interior columns were much stiffer than exterior columns, especially for the first story. This observation is related directly to the higher axial force on interior columns. As these slopes are compared to those of the previous run, it can be seen that all columns experienced an average stiffness reduction of about 23%.

Figures 3.29 through 3.32 show the moment-normal force interaction curves for two columns on each of the first and second stories. It can be seen that all interior columns yielded in the two directions for both stories. The figures also indicate that exterior columns yielded only in the high axial force direction, and did not yield in the other direction. This observation suggests the column stiffness, and correspondingly its ability to attract more shear, is directly related to its axial force. This point will be discussed further in the following sections.

### Beams

The bending moments at the critical sections of the first story longitudinal beam

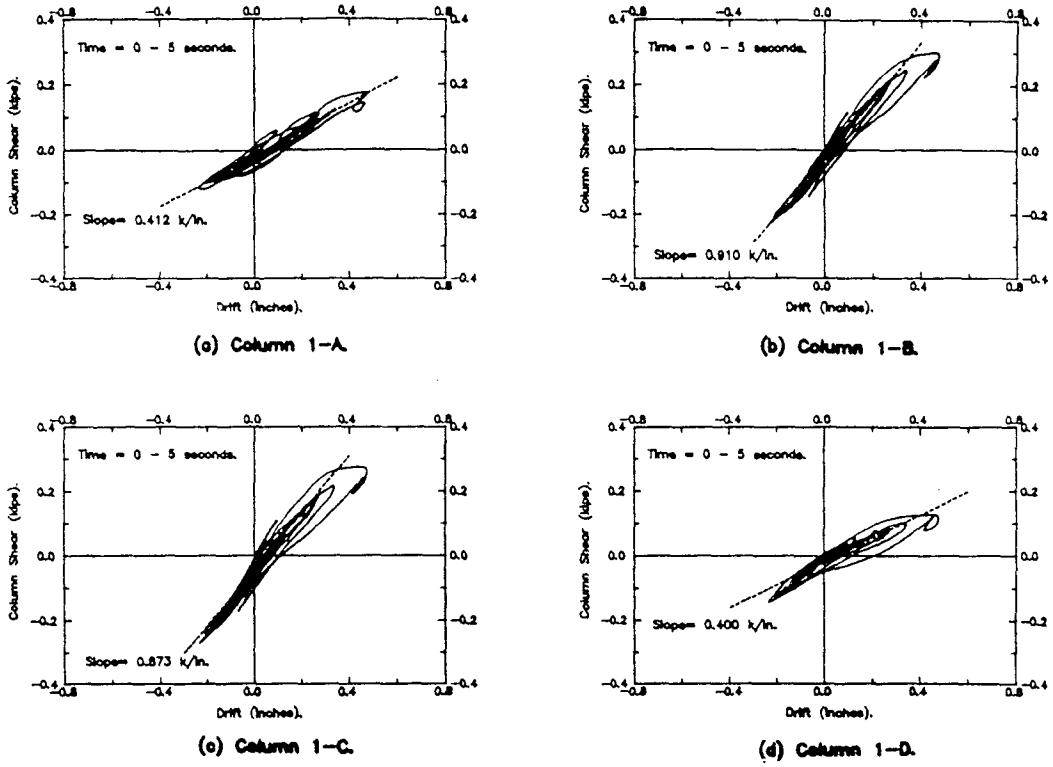


Figure 3.27: First Story Shear-Drift Hysteresis Curves (Run Taft 0.35-G).

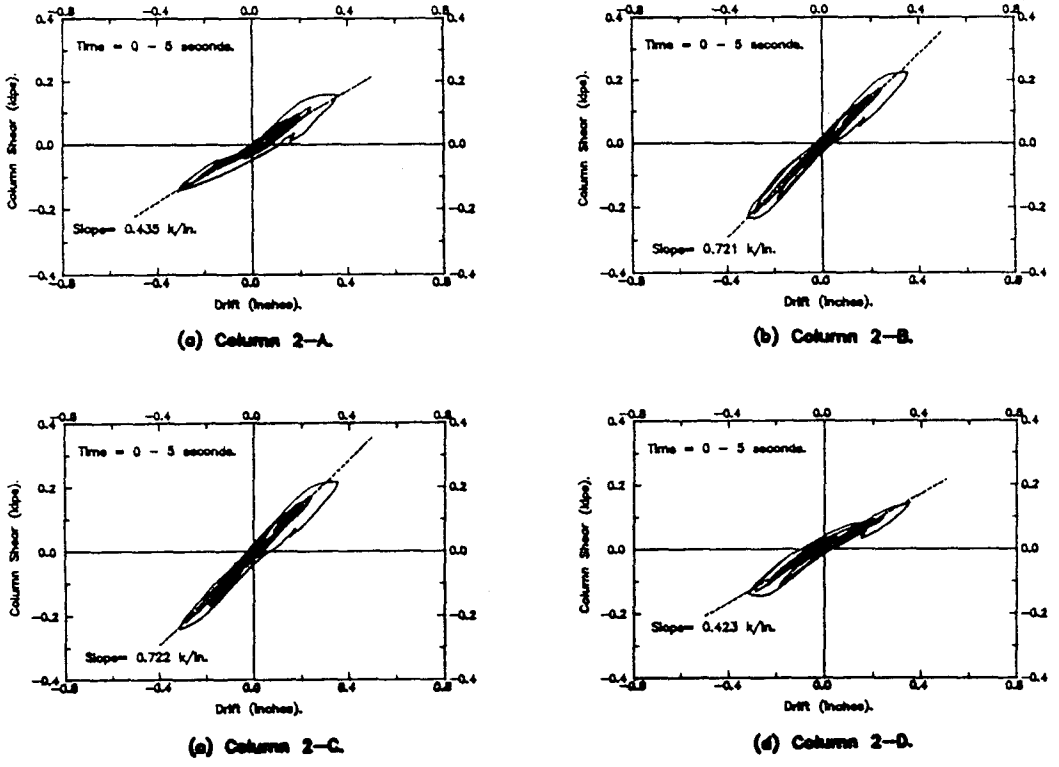


Figure 3.28: Second Story Shear-Drift Hysteresis Curves (Run Taft 0.35-G).

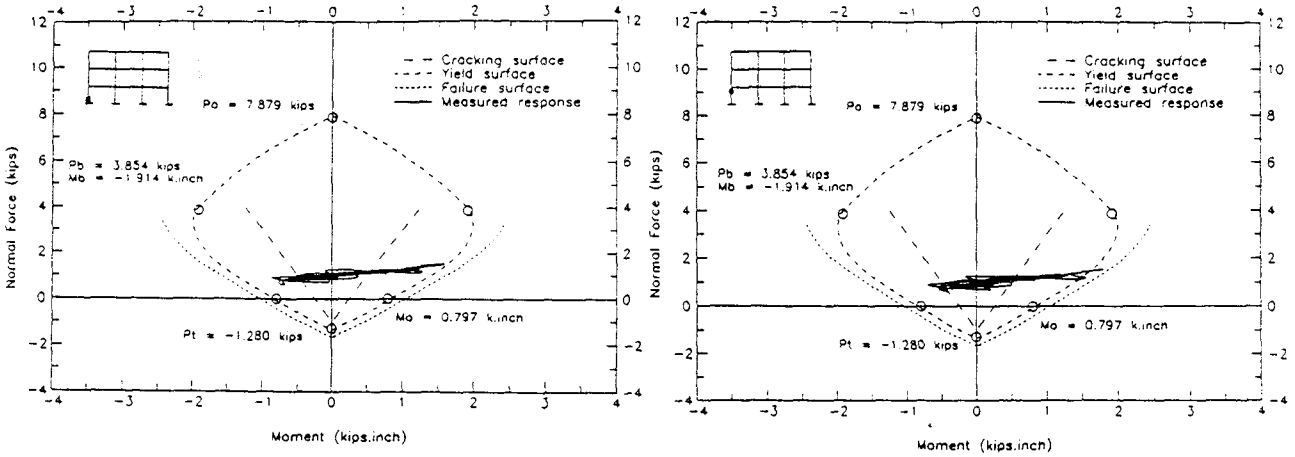


(a) Bottom Section. (b) Top Section.

Figure 3.29: Moment-Normal Force Response of Column 1-A (Run Taft 0.35-G).

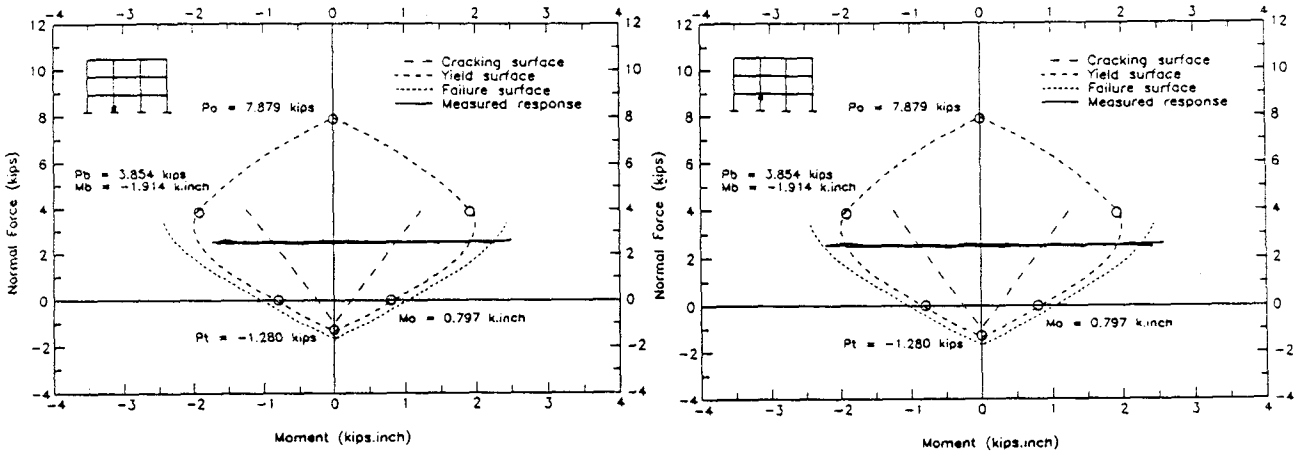


(a) Bottom Section. (b) Top Section.

Figure 3.30: Moment-Normal Force Response of Column 1-B (Run Taft 0.35-G).

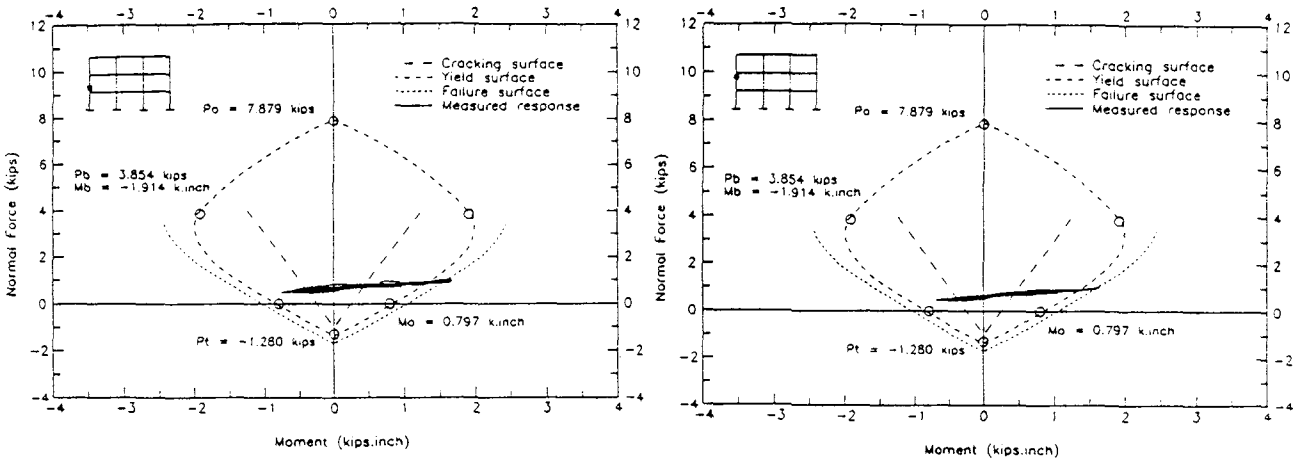


(a) Bottom Section.

(b) Top Section.

Figure 3.31: Moment-Normal Force Response of Column 2-A (Run Taft 0.35-G).

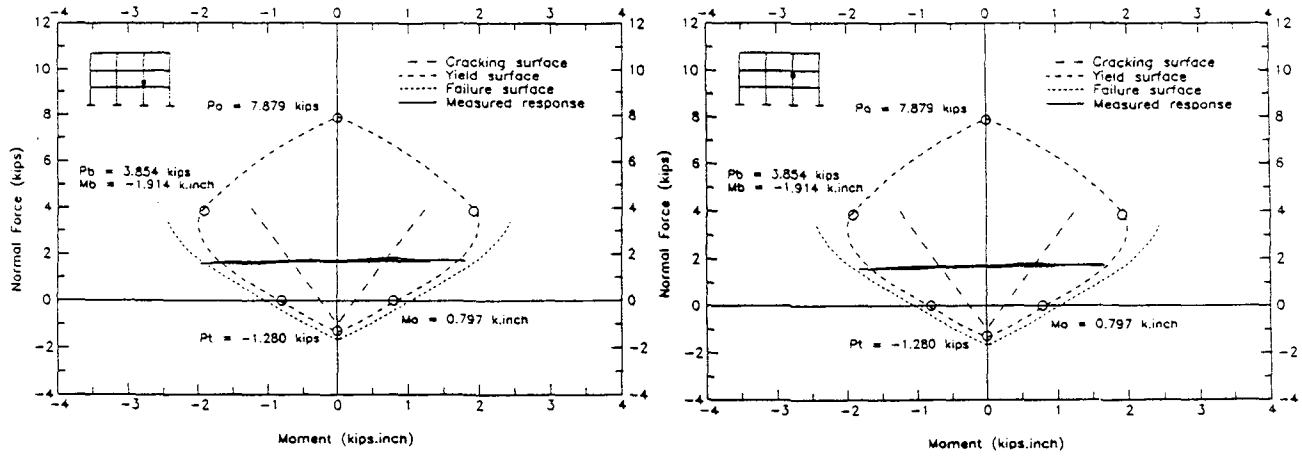


(a) Bottom Section.

(b) Top Section.

Figure 3.32: Moment-Normal Force Response of Column 2-C (Run Taft 0.35-G).

are shown in figures 3.33.a through 3.33.f for sections B1 through B6 respectively. The total moment at each section was obtained following the same steps explained for run Taft 0.18 g. It can be seen from figures 3.33.a and 3.33.f that sections B1 and B6 were subjected to very similar bending moment histories during this run. Both sections reached the positive yield point once, and did not yield at all in the negative direction during the entire run. The discontinuous beam positive reinforcement did not pullout during this run as indicated by visual inspection of the two sections after the seismic test.

The response of sections B3 and B4 during this run was generally similar to that of the previous run, where both beams did not yield in the negative direction. Section B4 cracked and yielded once in the positive direction, but the discontinuous positive beam reinforcement still did not pullout during this run.

Section B2 cracked during this run in the positive direction as shown in figure 3.33.b, but it still did not yield in either direction. On the other hand, section B5 was subjected to a relatively high bending moment and exceeded both its positive and negative yield points during this run. As these two sections were checked after the seismic test, there was no indication of a positive reinforcement pullout in either of them.

The bending moments of the longitudinal frame are shown in figures 3.34.a and 3.34.b at the time of maximum positive and maximum negative base shear respectively. It can be seen from both figures that the increase in the exterior column axial force resulting from the over-turning moment effect caused an increase in their bending moments. This phenomenon was observed to a less degree for

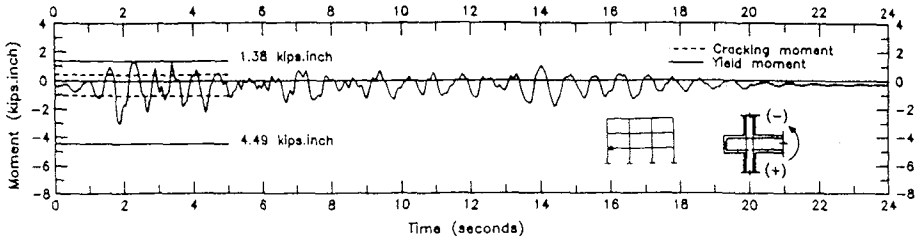


(a) Section B1.

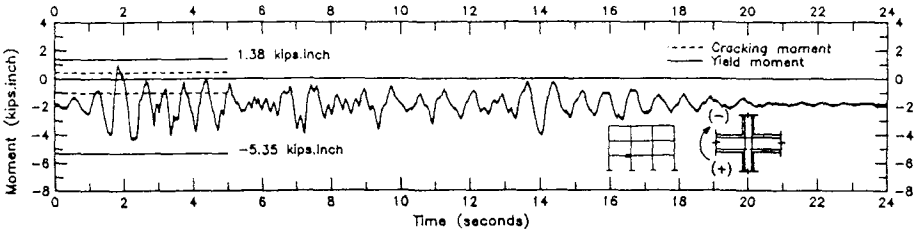


(b) Section B2.

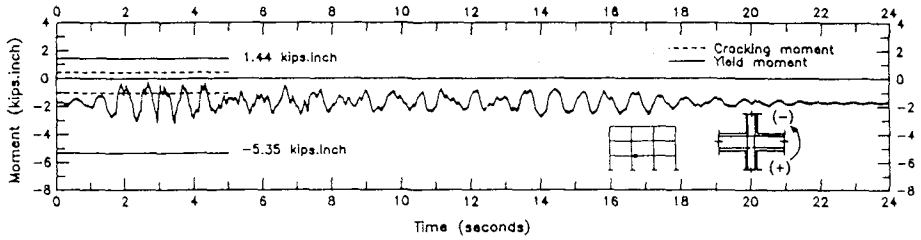


(c) Section B3.

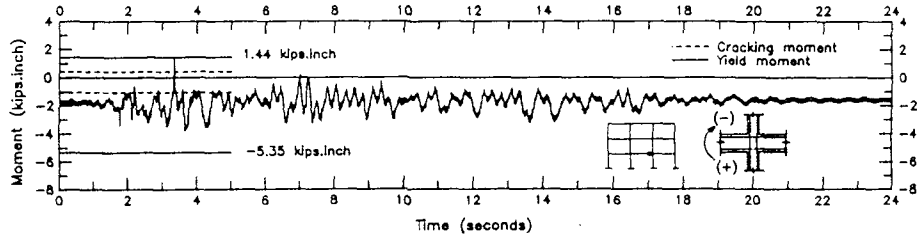


(d) Section B4.

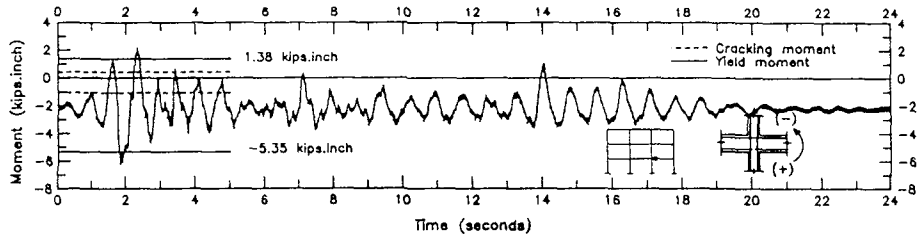


(e) Section B5.

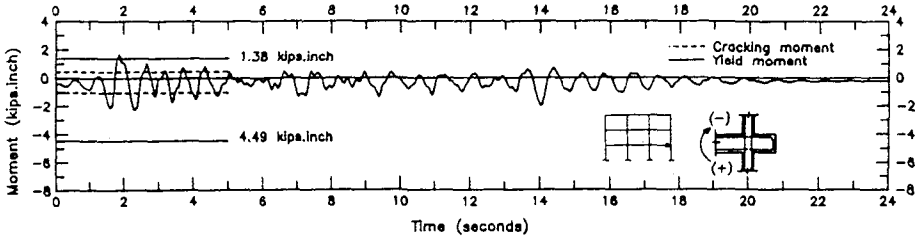


(f) Section B6.

Figure 3.33: Bending Moments of The First Story Longitudinal Beams (Run Taft 0.35-G).

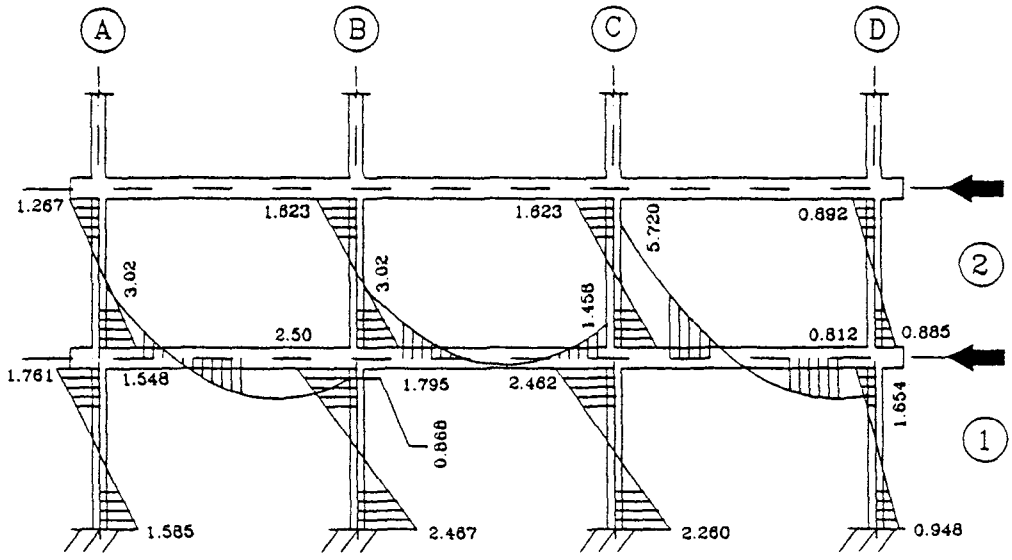


(a) Bending Moments at The Maximum Positive Base Shear.
(Time = 1.86 seconds)

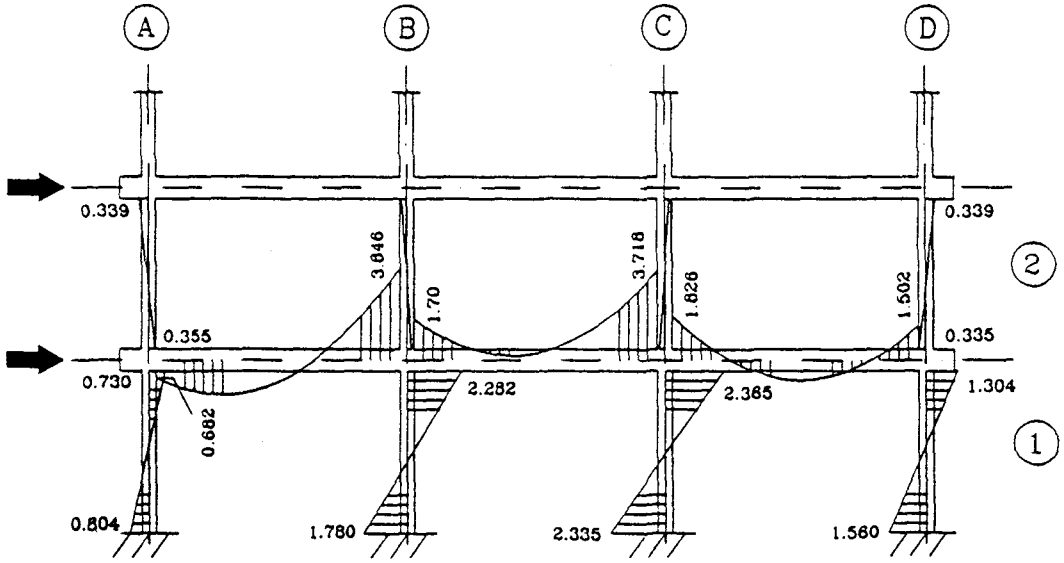


(b) Bending Moments at The Maximum Negative Base Shear.
(Time = 3.36 seconds)

**Figure 3.34: Bending Moments at The Maximum Base Shear (Run Taft 0.35-G).**

the interior columns as shown in the figures. The beam moments at the interior joints were always on the negative side (except for section B2), consequently no discontinuous beam positive reinforcement pull-out was detected. Although the situation was different for the exterior joint sections where positive moments were developed, it is believed that the positive beam reinforcement yielded at those sections without pulling out. These conclusions are in agreement with test results obtained from prototype beam-column joints [20] as will be discussed in chapter 5.

## 3.7 Run Taft 0.80 g

The purpose of this run was to examine the ultimate shear capacity of the model building and to study its failure mechanism. The model collapsed at the seventh second of the test after it experienced very large deformations and significant damage, especially at the first story. The maximum base shear based on the acceleration readings was 1.43 kips (3.3% higher than the previous run) which forms 9.7% of the total vertical loads on the building. The failure was caused by a soft story mechanism at the first story. Inspection of the video taped test at slow motion indicated that interior column column 1-B was the first column to fail, followed by the rest of the building in a progressive failure mode. This observation is in agreement with Paulay's [19] suggestion that soft story mechanisms imposes very high ductility demand on the columns, which the highly stressed interior columns could not deliver in the current case. No other reliable data was recorded during this run.

CHAPTER 4

# ANALYTICAL RESULTS

## 4.1 Introduction

Results of the numerical analyses performed for the 3-story model structure using program IDARC (Inelastic Damage Analysis of Reinforced Concrete structures) [14], [17], [18] are presented, discussed, and compared with the experimental results in this chapter. A full description of the program organization, model idealization, and input data can be found in reference [18].

## 4.2 3-Story model analysis

### 4.2.1 Input data

The input information of program IDARC used to perform the Taft 0.18-G test simulation are summarized in the following data sets:

1. **Structure configuration**

   The model structure (figure 4.1) is composed of two 3-bay by 3-story identical frames with a centerline to centerline span of 27", and a story height of 18". A total weight of 4.89 kips was assigned to each floor for the dynamic analysis.

2. **Material information**

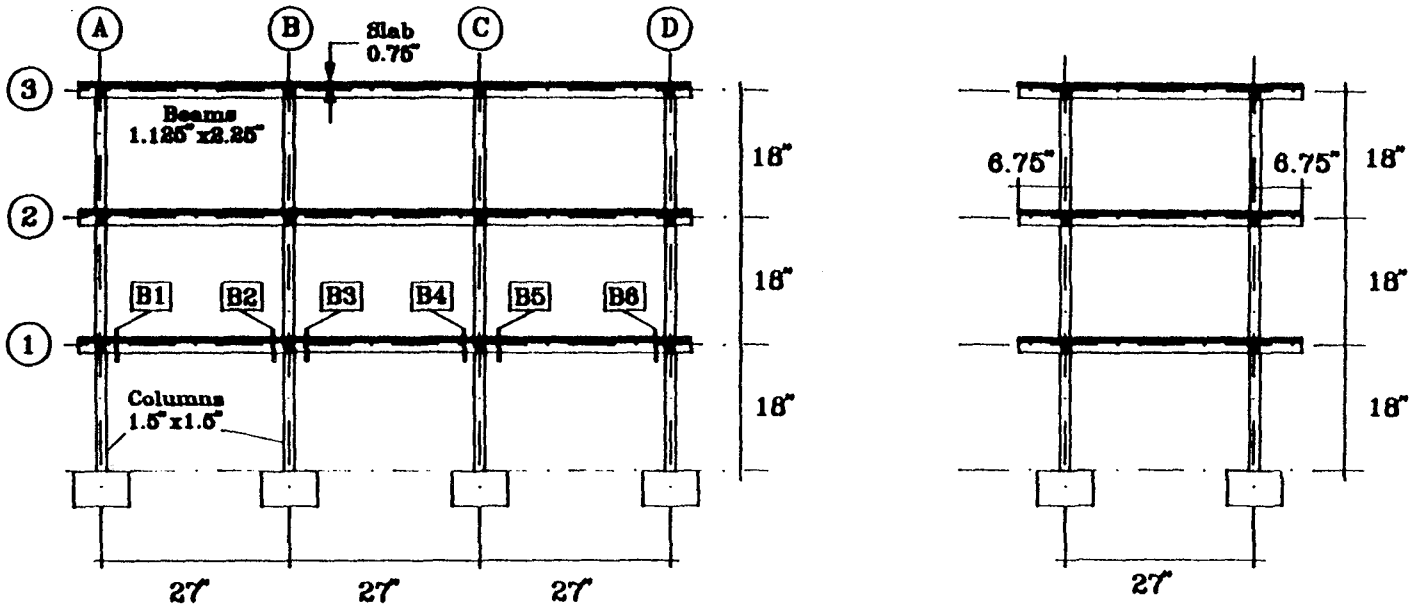


**(a) Elevation.** **(b) Sideview.**

Figure 4.1: General Layout of The 3-Story Model.

One type of concrete was used for all members, where the measured microconcrete properties were directly used (figure 4.2). A reduced modulus of elasticity of $0.7E_{0.45f_c'}$= 1400 ksi was used to account for the effect of concrete cracking due to the static loads and shrinkage. For the steel reinforcement, a yield stress of $f_y$= 40 ksi and a Young's modulus $E_s$= 29,000 ksi were adopted. The strain hardening portion of the steel stress-strain curve was assumed to start at a 3% strain and a strain hardening modulus of $E_{sh}$= 500 ksi was used beyond that point (figure 4.3).

### 3. Element information

All columns had the same cross section of 1.5" × 1.5" and a clear span of 16.875" for the first story and 15.75" for the second and the third stories. The column reinforcement and confinement ratios were directly obtained from figure 2.5. Beams had a common cross section of 1.125" × 2.25" and a 25.5" clear span. Tee sections had a slab thickness of 0.75" and an effective width of $\frac{span}{4}$= 6.75".

Since program IDARC requires the static reactions on each member, an elastic analysis was conducted using program STRAND-2D [22] to obtain the axial forces on the columns and the bending moments at each beam end (figure 4.4).

### 4. Dynamic analysis information

The measured table acceleration during the actual test was used as the input ground motion to eliminate any error in the calculated response due to the differences between the required and the measured acceleration traces. The

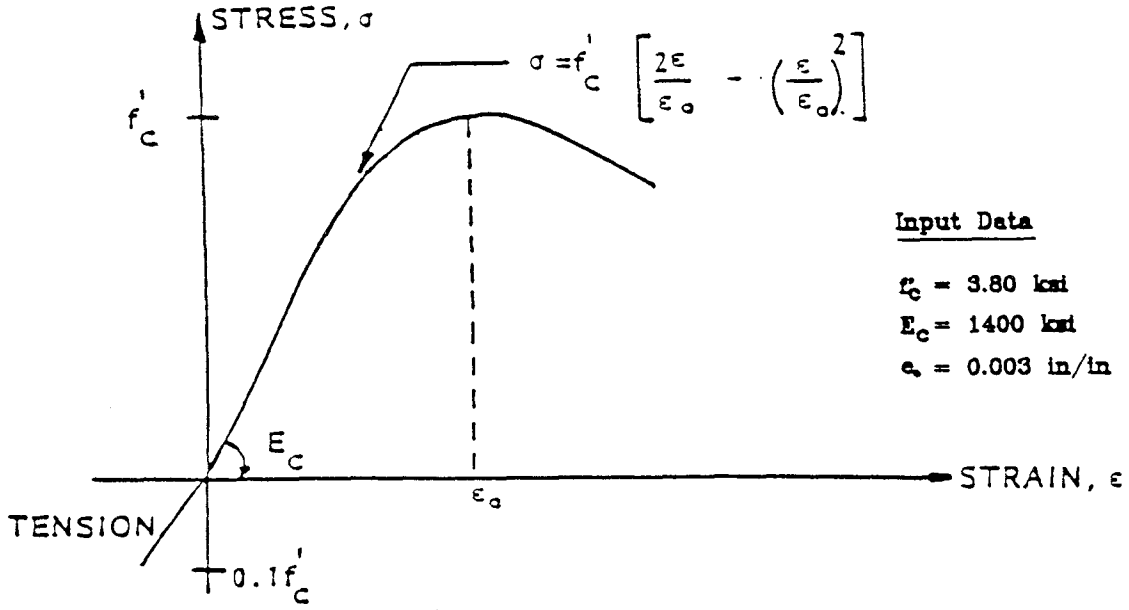


Figure 4.2: Idealized Microconcrete Stress-Strain Curve [Park et.al 1987].

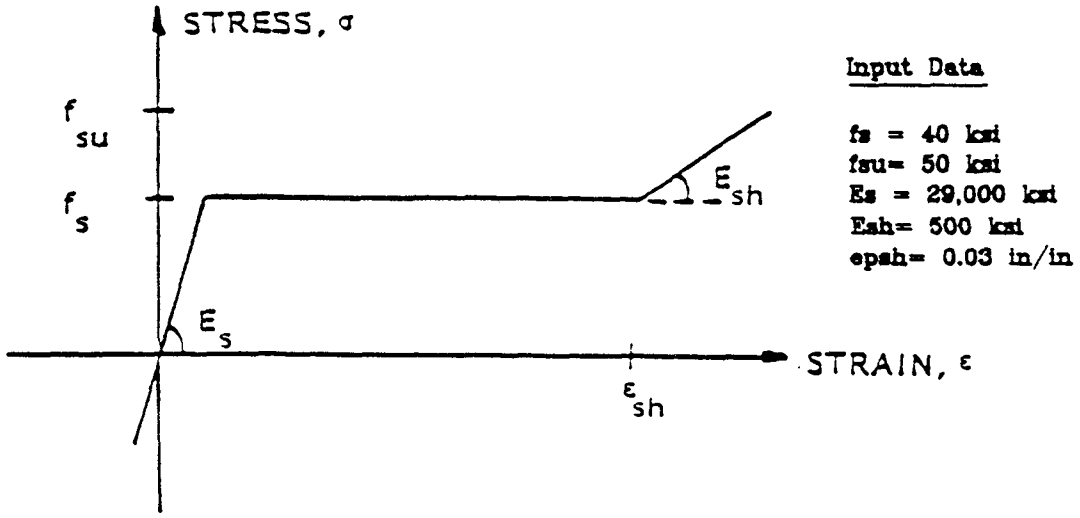


Figure 4.3: Idealized Steel Reinforcement Stress-Strain Curve (Park et.al 1987].

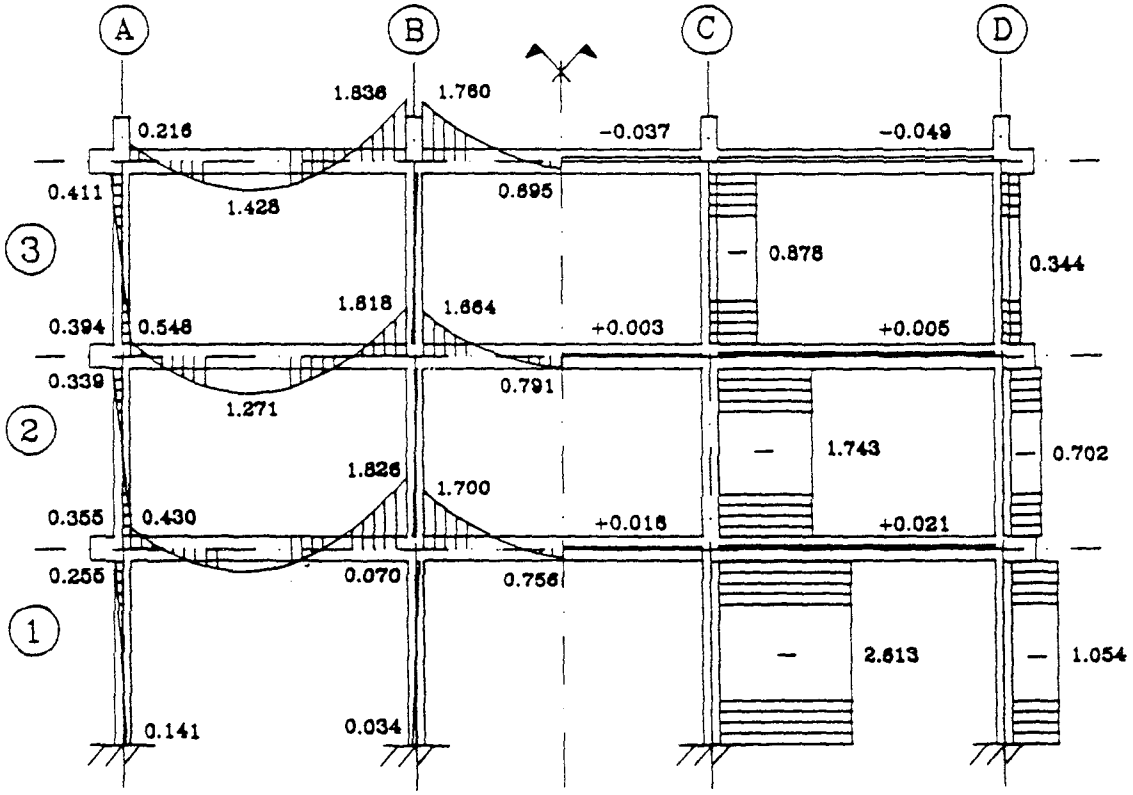


(a) Bending Moments (b) Normal Force

Figure 4.4: Static Normal Force and Bending Moments Due to Dead Loads Only.

first mode damping ratio obtained from the free-vibration test performed prior to the seismic tests was used in the analysis.

Based on the values recommended in references [14] and [17], the three parameters $\alpha$, $\beta$, and $\gamma$ were taken equal to 2.0, 0.05, and 1.0 respectively. It should be kept in mind that these parameters were based on prototype tests, and not on small scale models that have properties resembling those of the present model.

The same data was used for run Taft 0.35-G, but with the exception that the concrete modulus of elasticity was modified to $0.5E_{0.45f_c'}$= 1000 ksi to account for the stiffness reduction caused by run Taft 0.18-G, and the ground acceleration trace was that measured at the shake table surface during that run.

### 4.2.2 Run Taft 0.18-G results

#### Global response

The predicted global response of the model was generally in good agreement with the experimental results. It can be seen from figures 4.5.a through 4.5.c that the story shears were reasonably predicted during this run. The maximum shear, and second story shears were over-estimated by 7.7% and 0.7% respectively. Both the computed and the measured responses were in the same phase during the entire run, indicating that the controlling parameters of the hysteresis loops $\alpha$, $\beta$, and $\gamma$ were properly chosen. Some drift in the base shear was detected at the end of the run due to the accumulation of numerical error. It was found that this kind of error can be minimized by decreasing the integration time step from 0.002 seconds to 0.001 seconds.

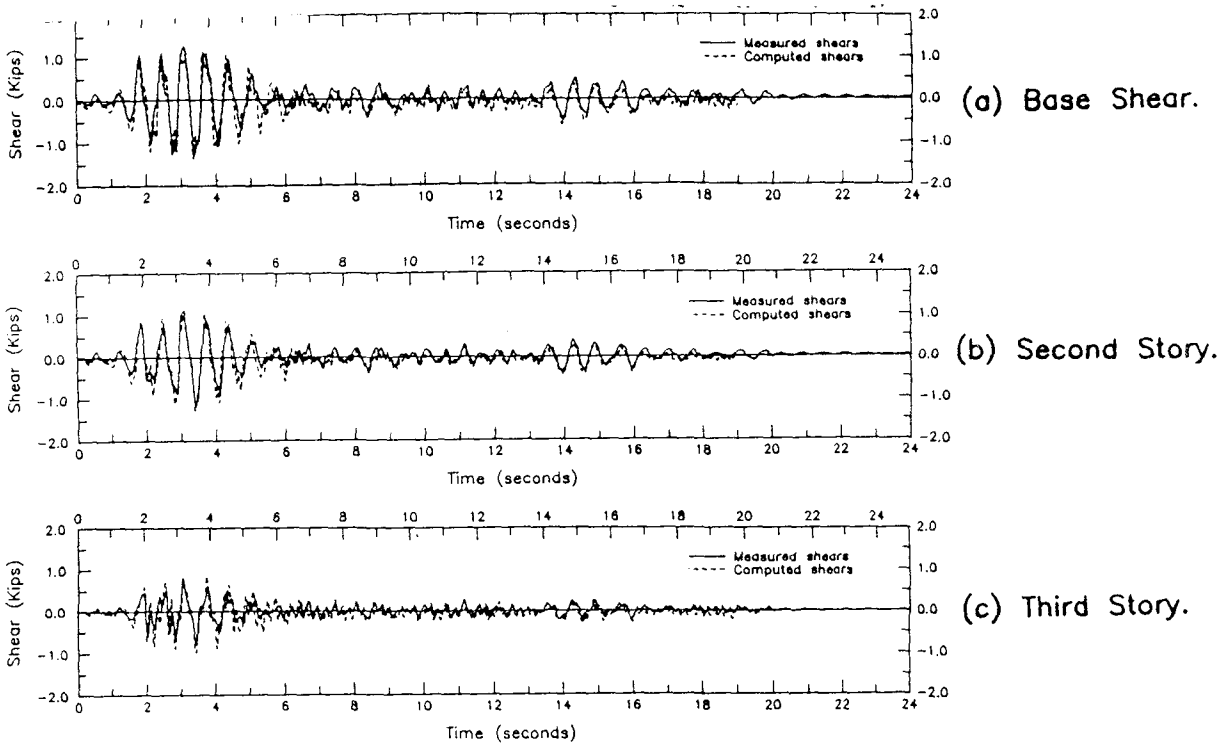


Figure 4.5: Computed Versus Measured Story Shears (Run Taft 0.18-G).

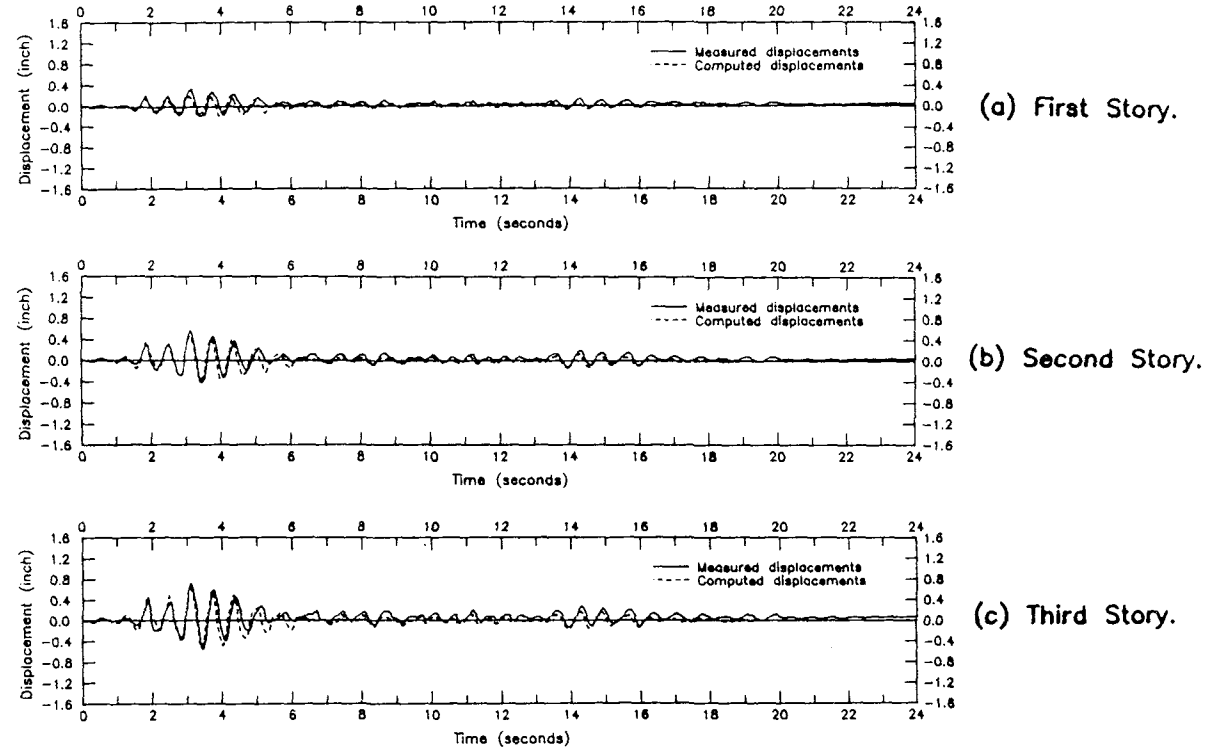


Figure 4.6: Computed Versus Measured Story Displacements (Run Taft 0.18-G).

The computed story displacements are plotted against the measured displacements in figures 4.6.a through 4.6.c for the first, second and third stories respectively. It can be seen that the third story displacement was reasonably predicted during this run. Although the maximum displacement was under-estimated by about 10%, and the computed displacements were slightly out of phase during the first few seconds, both the computed and the measured traces were generally in good agreement. On the other hand, the computed first and second story displacement time histories did not correlate well with the measured values, indicating that the mode shape of the structure was not accurately predicted. The maximum first and second story displacements were under-estimated by 31% and 16% respectively.

The program predicted an overall structural damage index of 1.0 corresponding to a complete collapse of the structure. This was a highly conservative estimation of the structural damage, since there was no experimental evidence that supports this prediction. The predicted yield mechanism at the end of this run is shown in figure 4.7.b, where it can be seen that the analytical mechanism was fundamentally different than the experimental one. The program predicted a weak beam-strong column mechanism while the experimental evidence indicated a weak column-strong beam mechanism that might lead to soft story failure type. Many factors could have contributed to this major discrepancy, among them:

- Analytical column shears are highly under-estimated from neglecting the P-$\Delta$ effect which was found experimentally to contribute up to 27% of the measured column shears for the current case.

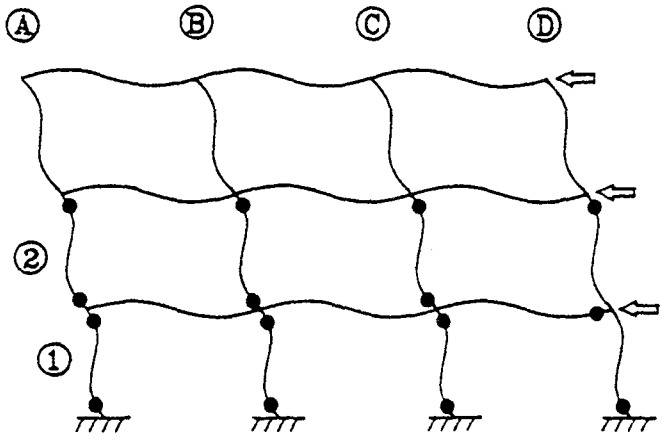


(a) Experimental Mechanism.

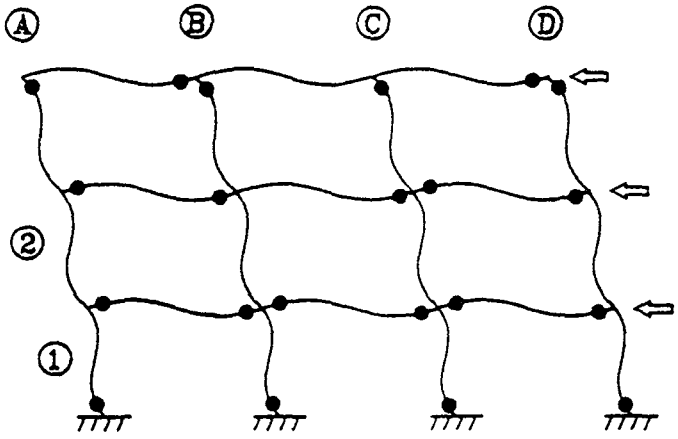


(b) Analytical Mechanism.

Figure 4.7: Yield Mechanism at Run Taft 0.18-G.

- Overturning moment effects were not included in the current analysis, while the axial load cell readings indicated the significant effect of the change of the column axial force on its stiffness and moment carrying capacity.
- The effective slab width of $\frac{span}{4}$ may be overly conservative, and a larger portion of the slab may have contributed to the beam strength.

It is believed that until these factors are taken into consideration, an acceptable prediction of the model failure mechanism is not possible.

**Local response**

Figures 4.8.a and 4.8.d show the computed shear time-histories for the first story columns. It can be seen that the computed shear forces were generally less than the measured values. This is directly attributed to overlooking the P-$\Delta$ effect in the analysis. As a result of ignoring the over-turning moment effects, symmetric columns (with respect to the building principal axis) showed nearly identical shear time-histories in contradiction to the experimental results. The predicted ratio of interior to exterior column shears at the moment of maximum base shear was 1.29 in contrast to measured value of 1.78. This observation suggests that the column stiffening due to the axial load was not accurately represented using the current model in program IDARC. A significant drift in column 1-A computed response was observed at the end of this run.

The damage indices for all first story columns were equal to 1.0, corresponding to a total collapse of the structure during this run. This was found to be a very conservative prediction where the model survived this run and even the next run

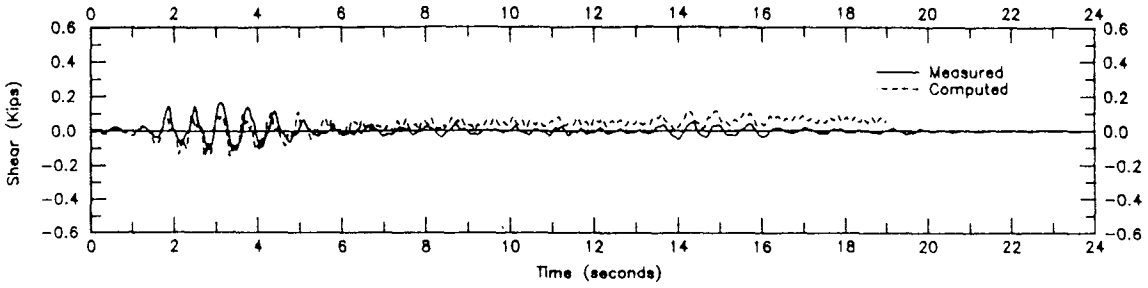


(a) Exterior Column 1–A.

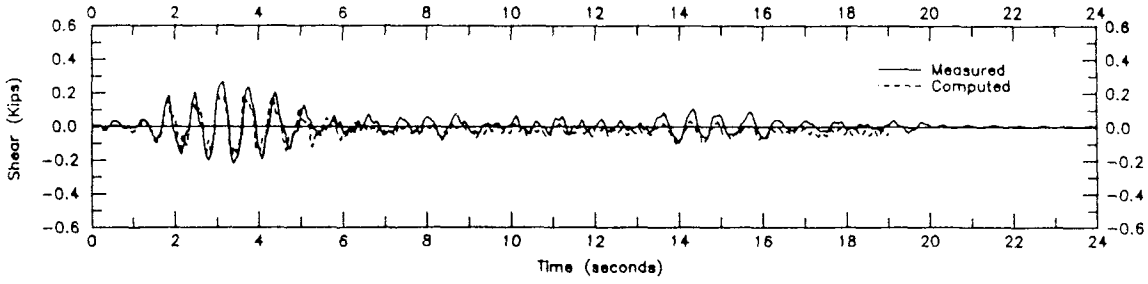


(b) Interior Column 1–B.

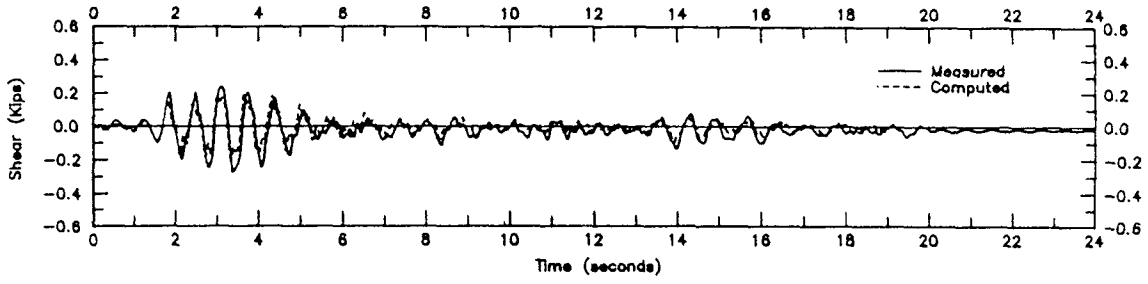


(c) Interior Column 1–C.

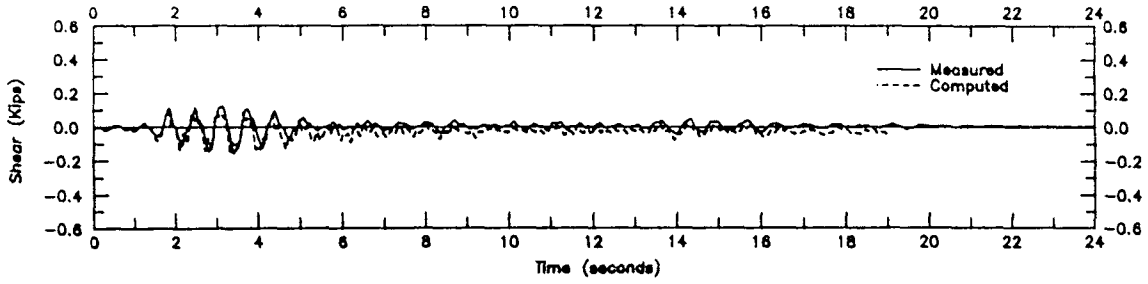


(d) Exterior Column 1–D.

Figure 4.8: Computed Versus Measured Column Shears (Run Taft 0.18-G).

with 0.35 G amplitude.

The computed first story beam bending moments are plotted against the measured moments in figures 4.9.a through 4.9.d for sections B1, B2, B3, and B4 respectively. It can be seen from all figures that there were appreciable differences between the measured and the computed moments; This could be referred to the large under-estimation of the column shears due to (a) neglecting the P-$\Delta$ effect, and (b) overlooking the change in the column axial force caused by the over-turning moments. The damage indices for the two considered beams were also very conservative (1.0) as compared to the visual damage observed at the end of the seismic test.

### 4.2.3 Run Taft 0.35-G

The same input data used for the previous run were used for this higher level run except that (a) the measured table acceleration during this run was used as the ground motion, and (b) the concrete modulus was reduced to $0.5E_{0.45f_c'}$= 1000 ksi to account for the reduction in the model stiffness due to cracking.

#### Global response

The computed story shears are plotted against the measured shears in figures 4.10.a through 4.10.c for the first, second, and third stories respectively. It can be seen all three story shears were reasonably predicted during this run. The differences between the computed maximum shear forces and the measured values were -3.2%, 3.2%, and 9% for the first, second and third stories respectively. It was also observed that both the computed and the measured shears were in phase during the entire run, indicating that the change in the model period due to stiffness degra-

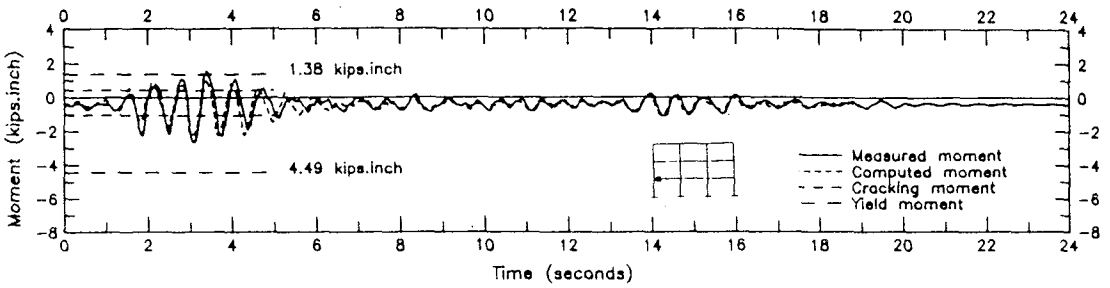


(a) Section B1.

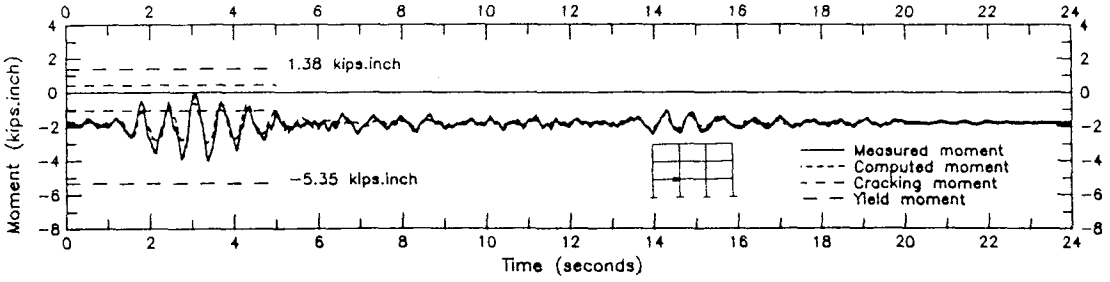


(b) Section B2.

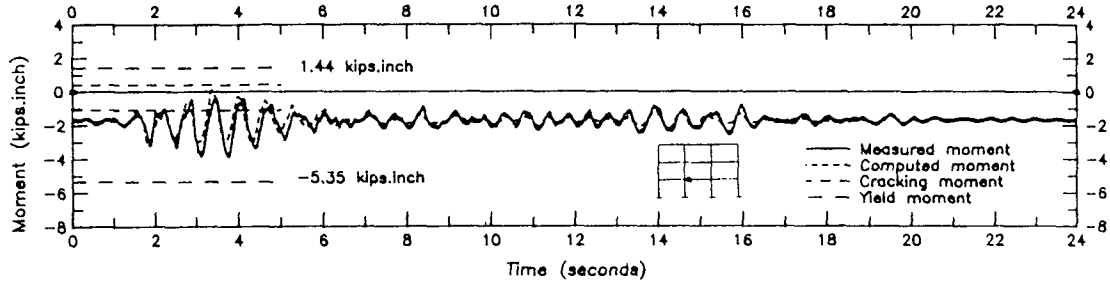


(c) Section B3.

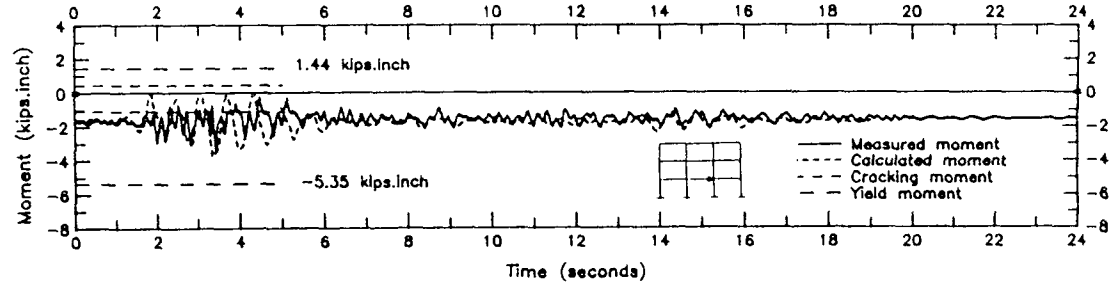


(d) Section B4.

Figure 4.9: Computed Versus Measured First Story Longitudinal Beam Moments (Run Taft 0.18-G).

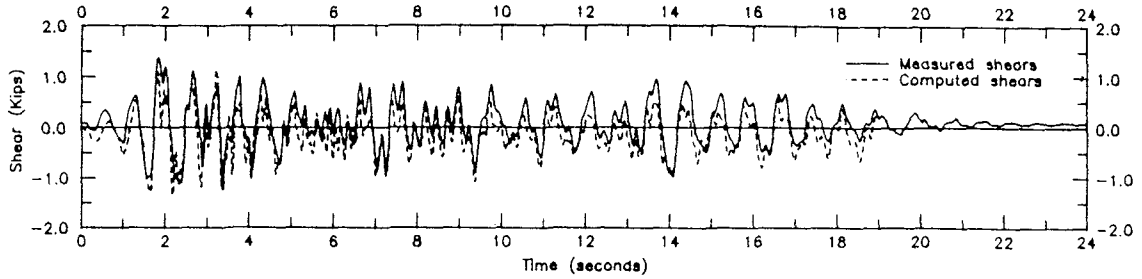


(a) Base Shear.

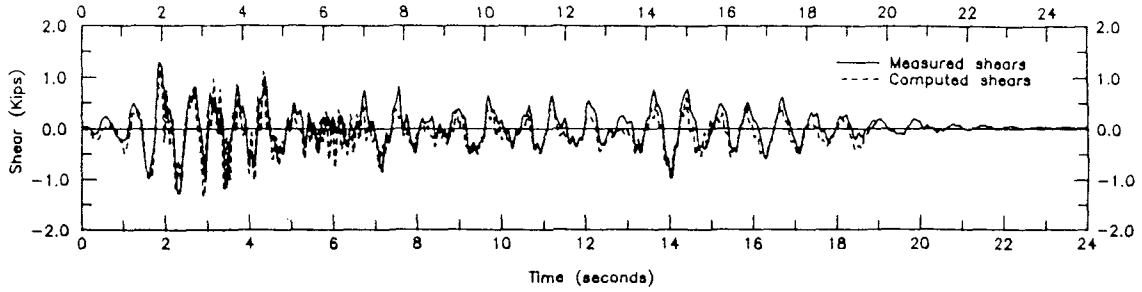


(b) Second Story.

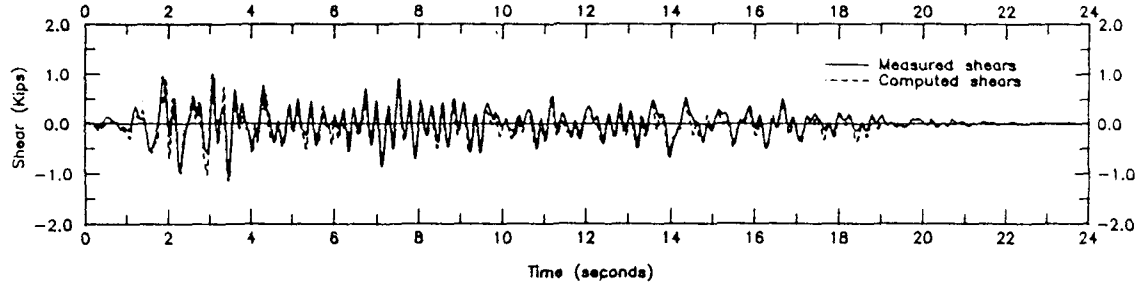


(c) Third Story.

Figure 4.10: Computed Versus Measured Story Shears (Run Taft 0.35-G).

dation and other factors was reasonably reflected in the analysis. As previously observed for run Taft 0.18-G, some base shear drift was observed near the end of the run due to numerical errors.

The story displacements shown in figure 4.11 did not correlate as well with the measured displacements. It can be seen from figure 4.11.c that the third story displacement was accurately predicted until the maximum positive value, then the computed displacements started to deviate from the measured ones. The same observation was valid to a lesser degree at the first and the second stories where the computed maximum displacements were 37% and 15% less than the measured value. This suggests that the mode shape was poorly estimated despite the good prediction of the story shears.

The estimated damage index for the whole building was equal to 1.0, indicating a total failure of the model. Again, this was in contradiction with the experimental results where no severe damage was detected after this run. More plastic hinges were developed at this run (figure 4.12), and the tendency of the model to fail in a soft-story mechanism was becoming more obvious.

### Local response

The computed first story column shears are plotted against the measured shears in figure 4.13. As previously observed for run Taft 0.18-G, the predicted shears were significantly less than the measured values. This was again referred to ignoring the P-$\Delta$ effect. The ratio of internal to external maximum column shears was 1.15 in contrast to the experimental value of 1.92 recorded during this run. The large difference indicates the inaccurate calculation of the column shears due to ignoring

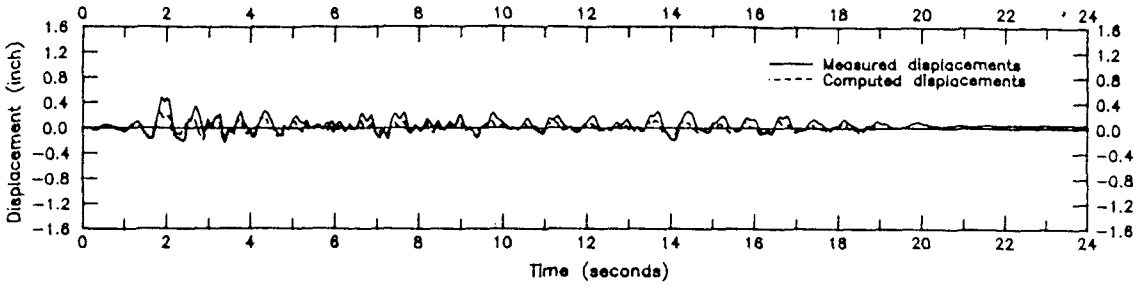


(a) First Story.

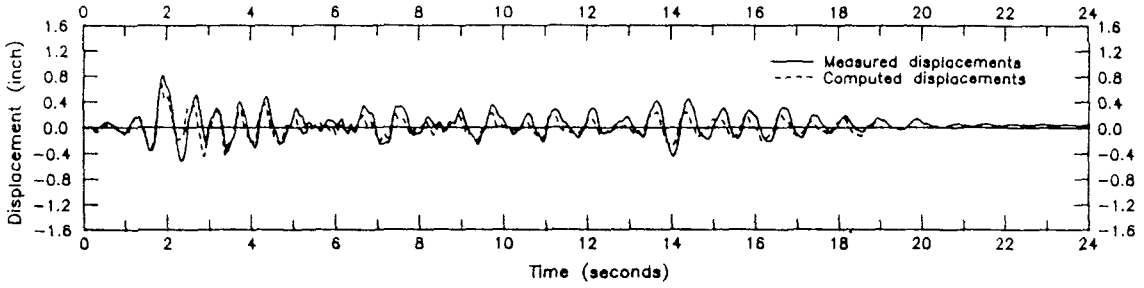


(b) Second Story.

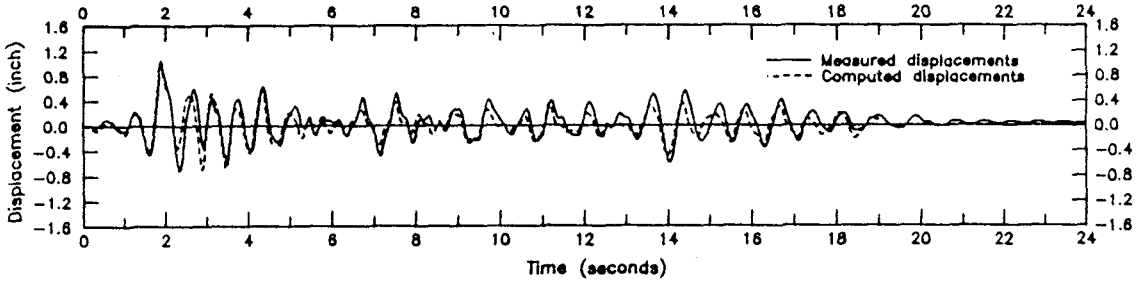


(c) Third Story.

Figure 4.11: Computed Versus Measured Story Displacements (Run Taft 0.35-G).

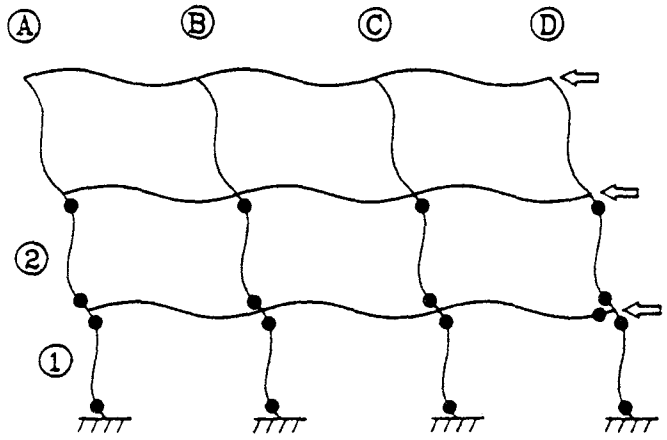


**(a) Experimental Mechanism.**

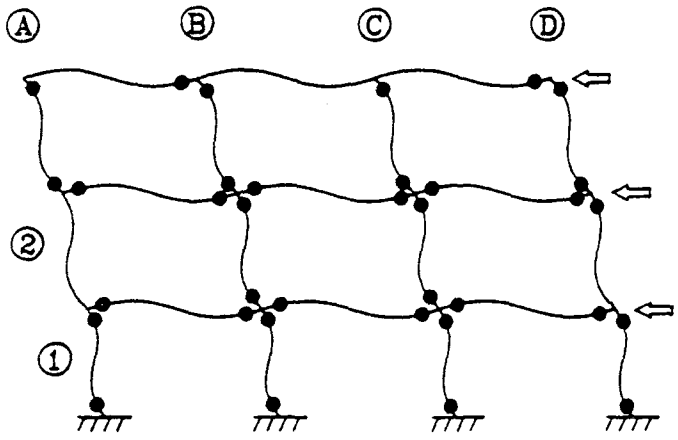


**(b) Analytical Mechanism.**

Figure 4.12: Yield Mechanism at Run Taft 0.35-G.

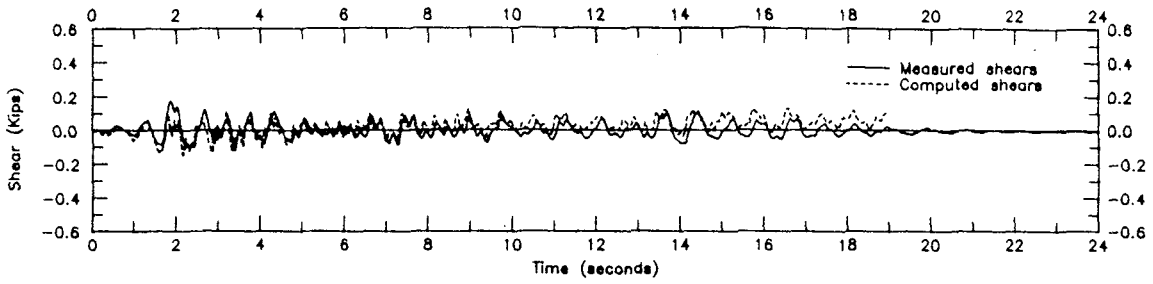


(a) Column 1–A.

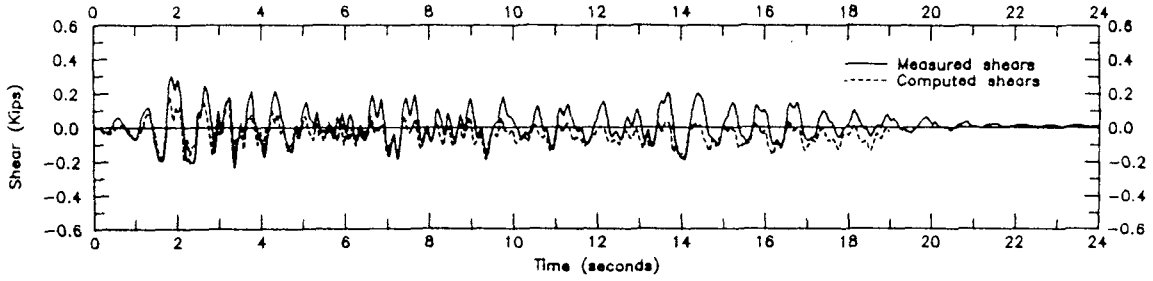


(b) Second Story.

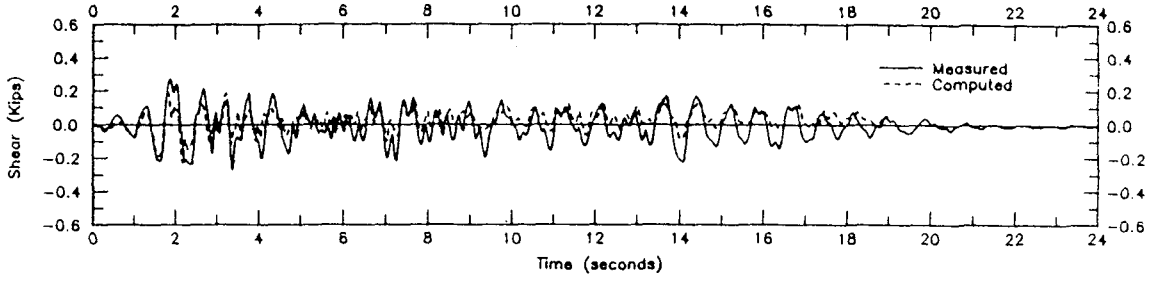


(c) Exterior Column 1–C.

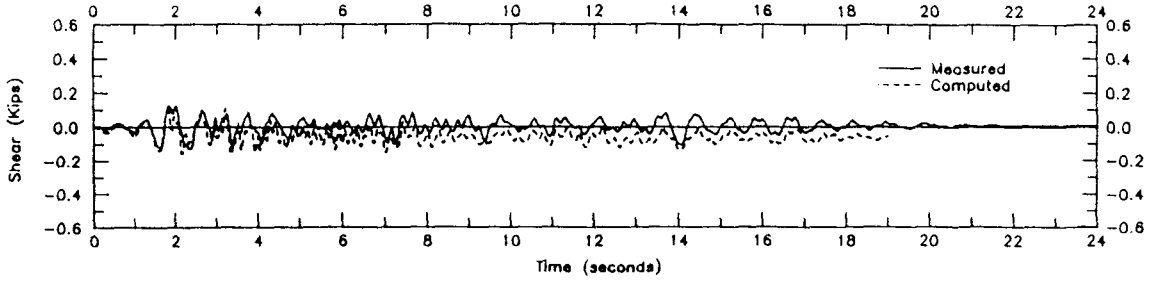


(d) Interior Column 1–D.

Figure 4.13: Computed Versus Measured Column Shears (Run Taft 0.35-G).

the overturning moment effects. The program predicted a common damage index of 1.0 for all the first story columns, which has proven to be very conservative as compared to the visual damage of the model columns after this run.

The computed first story longitudinal beam moments are plotted against the measured moments in figures 4.14.a through 4.14.d for sections B1, B2, B3, and B4 respectively. The same observations made for the previous can be extended to the current run where the computed moments were significantly less than the measured ones, especially at the beam sections that are most affected by the column axial force changes like section B2 (figure 4.14.b). It was important to notice that the program indicated beam yielding in the negative moments at sections that did not yield experimentally. This questions the use of the ACI [2] effective slab width in the analysis, as the experimental evidence indicated that a larger portion of the slab contributed to the beam strength.

### Summary

The analytical results of the 3-story model building using program IDARC can be summarized in the following points:

1. The global response of the 3-story model, in terms of story displacements and story shears can be reasonably predicted, given that the initial properties of the model such as stiffness reduction due to initial cracking and damping ratio can be rationally estimated. However, the first mode shape was inaccurately predicted by the analysis.

2. The predicted failure mechanism did not agree with the observed experimental behavior, suggesting that the portion of the slab contributing to the

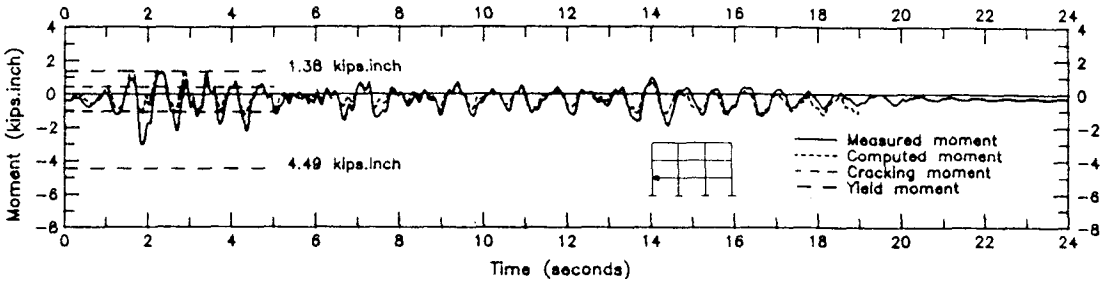


(a) Section B1.

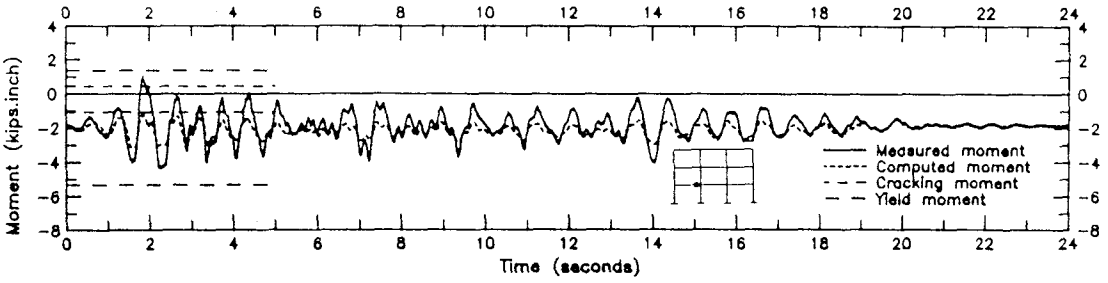


(b) Section B2.

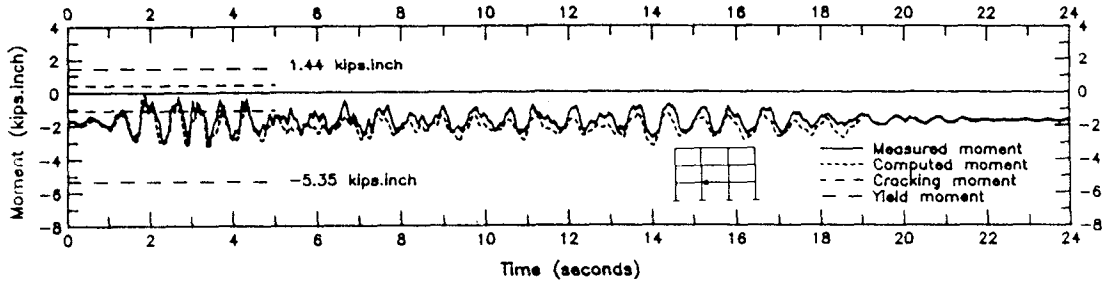


(a) Section B3.

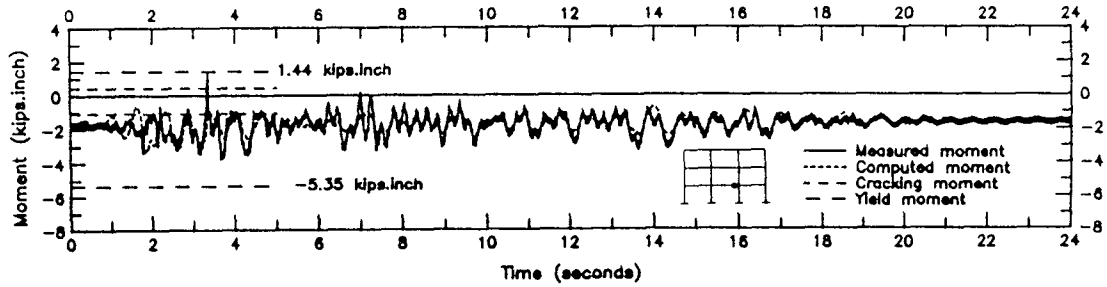


(d) Section B4.

Figure 4.14: Computed Versus Measured First Story Longitudinal Beam Moments (Run Taft 0.35-G).

beam strength was larger than the ACI [2] recommended effective slab width of $\frac{span}{4}$.

3. Column shear forces were highly under-estimated due to neglecting both the P-$\triangle$ and the over-turning moment effects.

4. Beam moments were also affected by neglecting the over-turning moment effects, as the computed values were always smaller than the measured ones.

5. Finally, the damage indices provided by the program were highly conservative, as the model structure always showed much less damage than predicted.

CHAPTER 5

# PERFORMANCE EVALUATION OF LIGHTLY REINFORCED CONCRETE BUILDINGS DURING EARTHQUAKES

## 5.1 Introduction

The design philosophy of lightly reinforced concrete (LRC) buildings and its impact on the response of such buildings during earthquakes will be discussed in this chapter. The discussion will also extend to the implementation of the experimental evidence of the current research in addition to previous lightly reinforced concrete component tests conducted at Cornell University [5], [20] in the evaluation of the seismic performance of LRC structures.

## 5.2 Design philosophy of LRC buildings versus modern seismic design

The terminology "lightly reinforced concrete structures" is usually referred to those buildings that are designed and detailed to resist primarily gravity loads. The design of such buildings aims at producing a structure that behaves satisfactorily under service loads in terms of cracking and deflection limits, and provides an ample margin of safety at ultimate. Such structures are not expected either to undergo large deformations, or to dissipate energy during this action (if it occurs). This

design approach had been adopted since early 1900's in the Central and Eastern U.S. region and has resulted in economically sound structures that have shown excellent performance over the years.

In contrast to the previous design approach, modern seismic design aims at producing a structure that can withstand mild earthquakes with no structural damage, moderate (frequent) earthquakes with repairable damage, and does not collapse during strong (rare) earthquakes. Recognizing the fact that designing a structure that remains elastic during strong ground motions would be neither practical nor economic, the design codes [2] assumes non-linear (ductile) structure response that can dissipate a considerable amount of energy during the earthquake. In fact the recommended design lateral forces of a ductile structure are about only 25% of the forces the same structure would experience assuming elastic behavior. Special attention has been given to member proportions and reinforcement details that will guarantee ductile performance and will avoid the formation of local failure mechanisms (such as the soft story mechanism).

In the light of this introduction to the two design philosophies, a LRC structure will most likely carry certain characteristics that can be summarized in the following points:

1. Interior columns are subjected to high axial forces and relatively low bending moments, resulting in slender columns under high normal stresses and with low reinforcement ratios ($\rho$ of 1.0% is common, older buildings in New York city may have $\rho$ as low as 0.5%).

2. Columns have minimum confinement to prevent local buckling of the re-bars

and to hold the longitudinal reinforcement in place during casting. These hoops or spirals are not expected to add much to the column ductility.

3. The sum of column flexural strength at a joint might be equal or even less than that of the beams, especially for low rise buildings or the top 3 or 4 stories of a tall building.

4. Column lap splices are located immediately above the floor slab in the maximum bending moment region with no special confinement (figure 2.5).

5. Construction joints are located above and below the beam levels.

6. As in the case of columns, beams will have low reinforcement ratios. In addition, negative reinforcement is usually provided only over the support and its length is controlled by the development length (figures 2.5).

7. Beam positive (bottom) reinforcement is discontinuous and extends for only 6 inches inside the column (figure 2.5).

8. Shear reinforcement will be provided only when required by the design, and if provided, it may be in the form of open stirrups that have limited confining capacity (figure 2.6).

9. Joints will not be designed and their size will be governed by the intersecting beam and column sizes. Also little or no joint reinforcement will be provided at the joints (figure 2.5).

In addition to the previous characteristics, the common material design strengths during the period 1900 to 1970 were (a) a nominal steel yield stress $f_y$ of 40 ksi,

and (b) a concrete compressive strength no greater than 3,500 psi. The significance of these stresses will be discussed in section 5.3.2.

## 5.3 Implication of the design philosophy and the experimental evidence in performance evaluation

The aforementioned structural characteristics will create a certain mode of behavior of LRC structures during seismic excitation. In the following discussion, the anticipated LRC building performance will be introduced and criticized. Experimental evidence that supports the discussion will be provided when appropriate.

### 5.3.1 General performance evaluation

#### Stiffness degradation

Experimental results indicate that the stiffness of a LRC structure will be subjected to a significant reduction after the first few cycles of a moderate earthquake due to (a) the lack of ductility caused by the poor member confinement, especially at the joint region, and (b) the possible pullout of the discontinuous positive beam reinforcement, especially those with large diameter bars (#8 or larger [20]). These two factors were observed in previous tests conducted at Cornell (2-story building test [5]), where the model showed a high degree of flexibility even during a mild seismic run. Only the first factor contributed to the failure of the current 3-story model as will be discussed later.

#### Model deformation

LRC structures are most likely to experience large displacements during earth-

quakes. In Cornell tests [5], the relatively high degree of stiffness degradation of LRC buildings was associated with large inelastic deformations. This phenomena was observed for both model buildings. At run Taft 0.36-G, the 1/6 scale 2-story model [5], recorded a first story drift of 1.93%. Also, at an equally strong table motion (run Taft 0.35-G), the current 3-story model showed a 2.63% drift. Although these figures depend heavily on the loading history and the damage level of each structure, they provide an idea of the degree of flexibility of this type of building. It is important to emphasize that in these two seismic tests, no significant damage was observed (in terms of excessive cracking or positive reinforcement pullout) in the beams of either buildings. It was concluded that the column slenderness (resulting from gravity load design) was responsible for the high degree of flexibility.

### 5.3.2 Member performance

#### Columns

The current model test provided a good opportunity of investigating the response of both interior and exterior columns. The ratio $P/(A_g f_c^{'})$ was equal to 0.13 for exterior column and 0.32 for interior columns, indicating that the ACI 318-89 code requirements for column strength and transverse reinforcement do apply. Table 5.1 shows the column-beam flexural strength ratios for the first story joints in the current model building. It can be seen that the code requirements are strongly violated (especially for interior columns) and a soft-story mechanism is to be expected.

Test results supported the previous speculation, where the 3-story model failure

Table 5.1: Ratio of Columns Flexural Strength to Beams Flexural Strengths for The First Story Beam-Column Joints

| Test | Exterior Joint | | Interior Joint | |
|---|---|---|---|---|
| | +ve Moment | −ve Moment | +ve Moment | −ve Moment |
| 3-Story Model | 1.76 | 0.54 | 0.54 | 0.54 |

was finally caused by a soft-story mechanism.

Column shear forces in LRC buildings seem to be highly influenced by the P-$\Delta$ effect. In the current 3-story model building case, an increase of 27% in the column shears due to the P-$\Delta$ effect was detected. The share of the total story shear force carried by each column was found to strongly depend on its axial force. This can be attributed to the fact that for columns supporting axial forces less than $P_b$, an increase in the axial force will result in an increase of their moment carrying capacity and consequently their shear capacity (figure 5.1). This will result in column shear distribution dictated by the axial force distribution. Although this argument deals with the column behavior at ultimate, experimental evidence observed by Abrams [1], Pessiki [20], and the current model tests indicated that the axial force effect starts at an earlier stage due to the delaying of cracking and consequently maintaining a relatively large column stiffness.

It was suggested by Abrams [1] that in addition to other structural connectivity factors, column axial forces should be recognized in assigning each column share of the total story shear force. He argued that the column stiffening effects do

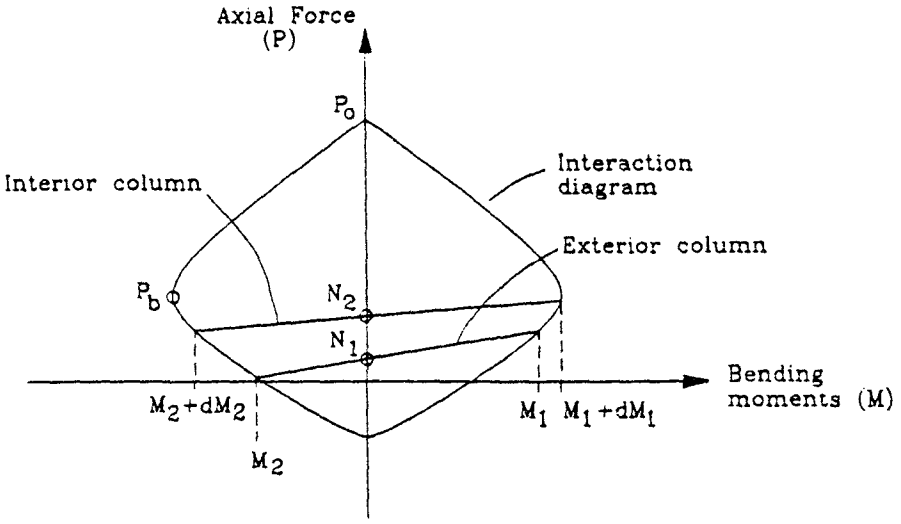


(a) Effect of Column Axial Force on Its Flexural Capacity.

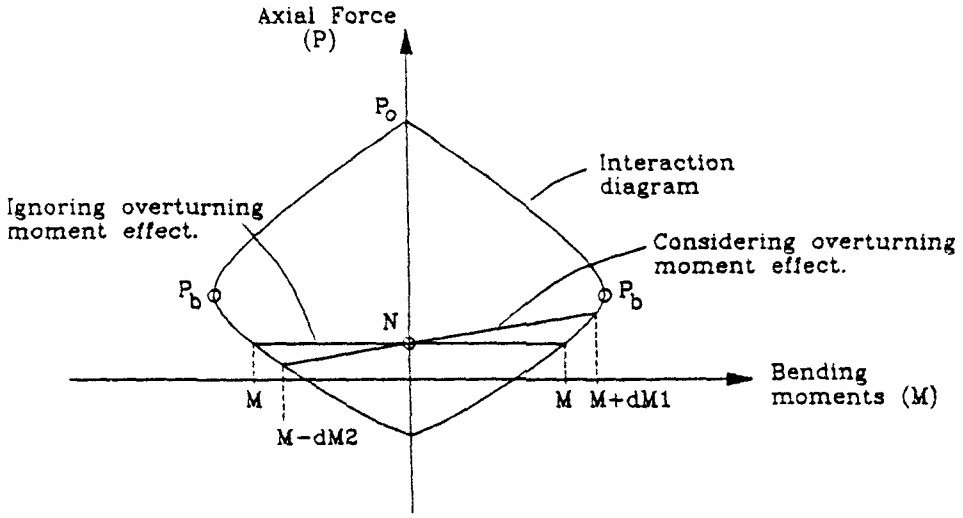


(b) Overturning Moment Effect on The Column Flexural Capacity.

Figure 5.1: Effect of Axial Force Variation on The Column Flexural Capacity.

not appear in any elastic structural analysis. It is the author's opinion that this should be coupled with that fact that column axial forces are continuously changing during an earthquake, especially for exterior columns where a fluctuation of $\pm 40\%$ was observed due to the over-turning moment effects. The change in column axial force, and consequently the shear force, is expected to be more severe for slender buildings with aspect ratios larger than 2.

**Beams**

Beam behavior observed during the model test was consistent with the observed behavior for full-scale component tests, where pullout stresses of 53 ksi and 30 ksi were recorded for #6 bars and #8 bars respectively [20]. This indicates that for the currently used grade 40 steel, small diameter bars might yield before they pullout. However, the discontinuous bars pullout stresses are expected to be less in exterior joints due to the reduction of the column axial compressive force (which may even turn to tension in slender buildings) when the joint is subjected to opening moments (figure 5.2). This prediction is in good agreement with the test results where the positive beam reinforcement pullout did not occur in the 3-story model test. The reflection of positive beam reinforcement pullout on the structure response will be discussed in more detail in the following section.

The slab contribution was found to be significant as it added extra strength to the beams with respect to the columns, especially when beam sections were subjected to negative moments. This resulted in developing the plastic hinges in the columns instead of the beams, creating a soft-story mechanism.

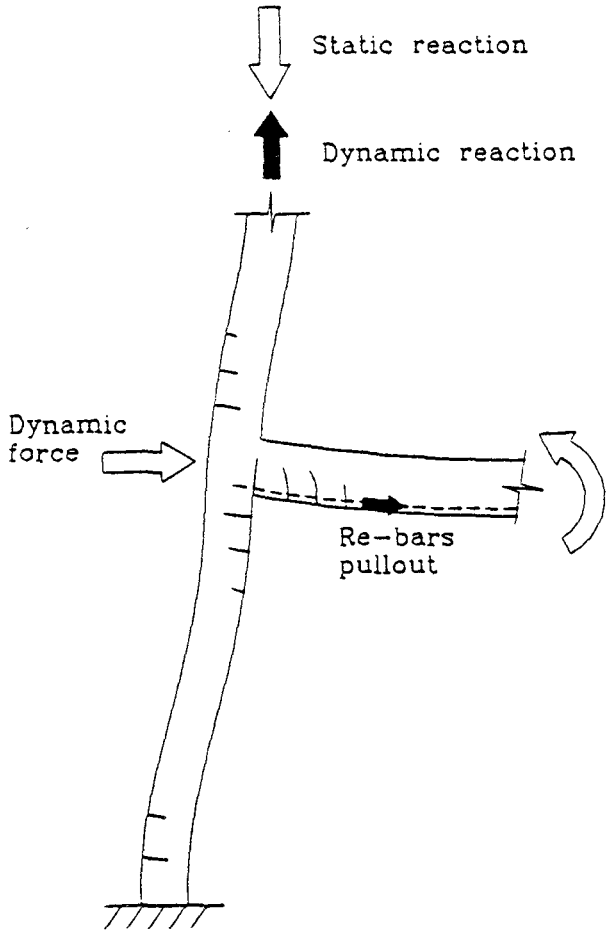


Figure 5.2: Re-bars Pullout at Exterior Beam-Column Joints.

### 5.3.3 Failure mechanism

#### Small-scale model test

The 3-story model collapsed in a soft-story failure mechanism during the Taft 0.8-G seismic test (figure 5.3). At failure, columns which were much weaker than the beams (table 5.1) experienced very large deformations associated with a significant increase in bending moments and shear forces caused by the P-$\triangle$ effect. Playback of the video tape recorded during the test indicated that failure started at one of the interior columns followed by the other columns in a progressive failure mode. This was in agreement with that fact that the high axial forces in interior columns significantly limited their ductility as compared with external columns.

#### Large-scale LRC beam-column tests

The failure of the four large-scale LRC beam-column specimens tested previously at Cornell [20] was always caused by beam failure due to the positive reinforcement pullout. This was associated with a significant damage in the joint region and the top and bottom columns. This mechanism was different than the observed mechanisms for the two small-scale model tests, where failure was caused by a soft-story mechanism. Both the beams and the joint region were not subjected to severe damage, even when beam positive reinforcement pullout took place. The discrepancy is mainly attributed to eliminating both the slab and the transverse beams in the full-scale specimens. This significantly reduced the strength of the beams with respect to the columns, especially in the negative moment side of the specimen. An approximate estimation of the slab contribution to the relative column-beam flexural strengths is provided in table 5.2. It can be seen that when

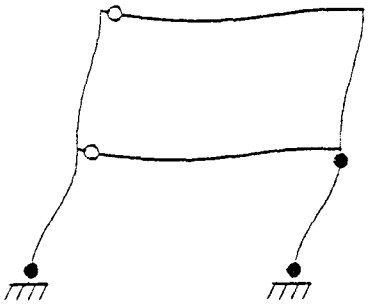

(a) 2-Story Model Failure Mechanism.

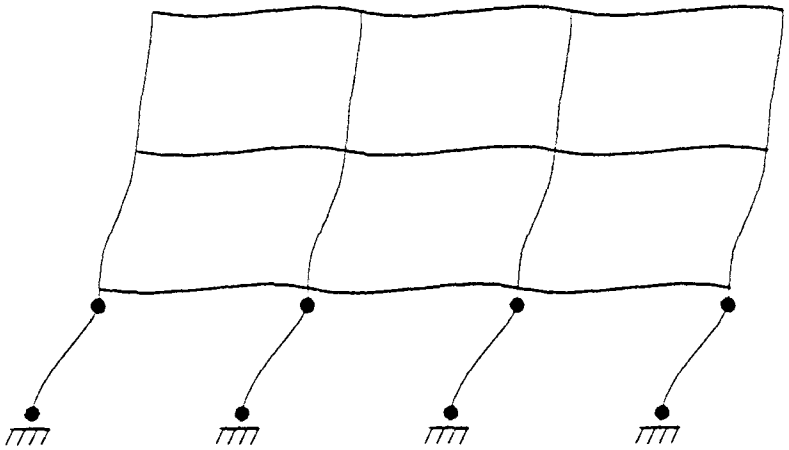

(b) 3-Story Model Failure Mechanism.

**Figure 5.3: Failure Mechanisms of The Model Structures.**

Table 5.2: Ratio of Column to Beam Flexural Strengths for The Full-scale Beam-Column Joints Tested at Cornell (Pessiki 1990)

| Specimen # | Sum of Columns Flexural Strength $\sum M_c$ (kips.in) | Sum of Beams Flexural Strength $\sum M_g$ (kips.in) | $R1^\star$ | $R2^\dagger$ | $R3^\ddagger$ |
|---|---|---|---|---|---|
| 7 | 5967 | 5651 | 1.06 | 1.39 | 0.87 |
| 8 | 6006 | 4713 | 1.27 | 1.40 | 0.87 |
| 9 | 5091 | 5022 | 1.01 | 1.29 | 0.82 |
| 10 | 5149 | 5495 | 1.12 | 1.47 | 0.93 |

$\star$ $R1 = \frac{\sum M_c}{\sum M_g}$.

$\dagger$ $R2 = \frac{\sum M_c}{\sum M_g}$ considering only discontinuous steel pullout.

$\ddagger$ $R3 = \frac{\sum M_c}{\sum M_g}$ considering both the discontinuous steel pullout and the slab contribution to the beam strength.

the slab is assumed to increase the beam negative moment flexural capacity by only 75% [4], [23], the sum of the beams flexural strength $\sum M_g$ exceeds that of the columns $\sum M_c$ even when the discontinuous steel pullout is considered (last column of table 5.2). This points out the high probability of a soft-story mechanism in LRC buildings, and the importance of including the slab in this kind of tests.

## 5.4 General comments

The aforementioned discussion of the response of LRC buildings to seismic hazards indicates that due to the adoption of an inadequate design philosophy for the design (from a seismic point of view), the resulting buildings suffer from two major flaws. First, the relative member strengths are not appropriate for seismic resistant buildings, especially when the actual member capacities are considered. Secondly, the member reinforcement is not detailed to ensure ductility and energy dissipation. It seems from the current complete buildings tests that the first factor will dominate the response of low to medium rise LRC buildings during earthquakes. Although the non-seismic reinforcement detailing seems to be a severe disadvantage to these buildings, it has been proven experimentally that the detailing may result in unfavorable structure behavior (such as the development of excessive deformations), but not in a total collapse of the building (2-story model test [5]). On the other hand, when the relative member strength ratios allowed by the design codes [2], [3] were severely violated in the 3-story model, total building collapse due to a soft-story mechanism took place.

It was interesting to notice that while the current design codes (ACI 318-89 [2] and ACI-ASCE committee 352 [3]) are being criticized by many investigators [19], [16] for allowing an unconservative column to beam strength ratio of 1.2 [2] or 1.4 [3], many of the existing LRC buildings highly violate these requirements. This fact should be taken into account when considering a retrofit for such buildings. It may not be sufficient to overcome the inadequate detailing problem. Instead, the whole building should be re-designed for earthquake resistance according to

the given seismic zone requirement; then specific member strengthening can be performed with special attention paid to the reinforcement details.

CHAPTER 6

# SUMMARY, CONCLUSIONS, AND FUTURE RESEARCH

## 6.1 Introduction

Since the early 1900's, thousands of buildings in the Central and Eastern United States were designed and detailed to resist primarily gravity loads with little or no consideration to any lateral forces due to wind or earthquakes. However, seismic activities are possible in these areas where this kind of building may experience significant damage. The study reported here is a part of a comprehensive research effort at Cornell University on the performance of lightly reinforced concrete structures subjected to earthquakes.

In the first phase of this study, started in 1987, improved small-scale modeling techniques for reinforced concrete structures under dynamic loading were developed [9]. In the second phase, two lightly reinforced concrete small-scale buildings were constructed and tested on the Cornell University shake table to evaluate their seismic performance. The final phase included an assessment of the adequacy of program IDARC for predicting the response of this type of building. Only the last two phases of the investigation are summarized in Section 6.2 of this chapter. Section 6.3 includes the conclusions of both the experimental and the analytical work. This chapter ends with recommendations for future research in this area.

## 6.2 Summary

### 6.2.1 Experimental work

The lightly reinforced concrete building tested during this research was a $\frac{1}{8}$ scale 3-story one-bay by three-bay story office building. The model designed for gravity loads and detailed in such a way that it reflects as close as possible typical design practice. It contained no walls or partitions. Test results will be summarized in the following sections.

#### 3-Story model test results

The 3-story model was tested on the Cornell University shake table using the Taft 1952 S69E earthquake. The test amplitudes were 0.05 g, 0.18 g, 0.35 g, and 0.80 g. The model collapsed after the first 7 seconds of the last run. Test results can be summarized in the following points:

1. The model response was dominated by the first mode of vibration during the seismic tests.

2. The same mode shape was detected during all seismic tests, even when the model response was highly non-linear.

3. The model showed a high degree of flexibility, where maximum inter-story drifts of 1.87% and 2.63% were recorded in the first story during run Taft 0.18 g and Taft 0.35 g, respectively.

4. Except for run Taft 0.05 g, the large model deformation resulted in a significant P-$\Delta$ effect that increased the column shears by as much as 27%.

5. The share of the total story shear force carried by each column was found to be heavily dependent on the axial force acting on the column. Interior columns in the 3-story model resisted about twice the shear force acting on the exterior columns.

6. Most of the deformation, damage, and energy dissipation occurred in the first story column. No significant damage was observed in the beams or the joint panels.

7. Columns lap splices did not appear to be a controlling factor in the model columns response.

8. Discontinuous positive beam reinforcement did not pullout during the seismic tests.

9. Plastic hinging developed only in the columns and not in the beams or the joint panel.

10. The model failed in a soft-story mechanism in the first story columns.

## 6.3 Analytical results

The non-linear dynamic analysis for reinforced concrete program IDARC [18] was used to predict the response of the model building. The input data included geometric information, material properties, hysteretic rules parameters, and the ground motion (measured table acceleration). The findings of the analysis can be summarized in the following points:

1. The global response of lightly reinforced concrete buildings (story shears and story displacements) can be reasonably predicted using program IDARC

given that the initial dynamic properties (including the initial fundamental period T) of the structure are based on rational assumptions.

2. Good correlation between the experimental and the analytical global responses was obtained for the 3-story model. This was attributed to the fact that the discontinuous positive beam reinforcement did not pull-out in this building.

3. Program IDARC did not reflect the P-$\Delta$ effect, which was found to increase the first story column shears by about 27% in the 3-story model.

4. The effect of the continuously changing axial forces in the columns was not taken into account when evaluating the yield status of the columns. IDARC recognizes only the initial static axial forces in the analysis. This was found to misrepresent the exterior columns behavior where an axial force change of the order of $\pm$40% was detected.

5. The damage indices provided by the analysis highly overestimate the actual observed structural damage.

6. The effective slab width was found to be of vital importance in the analysis since it can directly affect the structure failure mechanism by increasing beam flexural strength to the point that column behavior governs.

## 6.4 Conclusions

The experimental work presented in this report is the first to address the performance of lightly reinforced concrete buildings tested under realistic seismic loading conditions. Test results of the model building revealed many important aspects of

the behavior of buildings during earthquakes. Based on the current experimental results and the analytical study, the following conclusions may be drawn:

1. Although the inadequate reinforcement details of lightly reinforced concrete structures may form a potential source of damage, they are probably not sufficient to develop a local failure mechanism. In fact, a large increase in the structure period might shift it to a descending part on the response spectrum of the given ground motion, resulting in a reduction in the level of lateral forces.

2. The currently existing lightly reinforced concrete (LRC) buildings may be subjected to very large deformations associated with a significant reduction in stiffness during a moderate earthquake.

3. Due to their high flexibility, the P-$\Delta$ effect is significant in LRC structures and should be considered in the analysis.

4. Lateral stiffness of columns is a strong function of their axial force level. This observation imposes a limitation on the use of most available elastic dynamic analysis programs where such effects do not appear.

5. The inclusion of the slab contribution to the beam flexural strength under negative moment is a vital step in the assessment of the performance of LRC structures during earthquakes since it has the potential of altering the relatively ductile strong column-weak beam mechanism to a soft-story mechanism. This will be true even when some reduction factors are applied to account for the discontinuous positive beam reinforcement pullout.

6. Low and medium height LRC buildings will collapse in a soft-story mechanism due to the higher flexural strengths of beams with respect to the columns. The situation is aggravated by the the very low ductility of these columns caused by their high axial forces and poor confinement of primary longitudinal reinforcement.

7. Small-scale reinforced concrete models can be used as a powerful tool to study the performance of complete buildings or large subassemblies.

## 6.5 Future Research

The current experimental effort has served as a preliminary investigation on the response of lightly reinforced concrete structures to seismic loads. The following topics still need to be addressed for a more thorough understanding of the behavior of this class of buildings during earthquakes.

### Effect of slab and transverse beams

Lightly reinforced concrete beam-column joint details tested so far at Cornell University did not include a slab or transverse beams [20]. The observed failure mechanism consistently started in the beams, a favorable situation for seismic loading. However, it has been indicated by other investigators that the presence of the slab and the transverse beams significantly increases the beam strength in the negative moment direction [4], [21]. The transverse beams can also provide some confinement to the discontinuous positive beam reinforcement, especially when they are subjected to negative moments. The contribution of the slab and the transverse beams act together in favor of the beam, resulting in a high possibility of devel-

oping the plastic hinges in the columns instead of the beams. More experimental evidence is required to clarify these issues, along with additional analyses to define the strength and ductility demands imposed on beams and columns during earthquakes.

**Effect of axial force variation in exterior joints.**

In slender buildings, exterior columns will be subjected to large changes in their axial forces during an earthquake and they may even be subjected to tension force instead of compression in extreme cases. Unfortunately, when these columns are subjected to their minimum axial force, the beam-column joint will be under an opening moment, and the discontinuous positive beam reinforcement will be in tension. It is believed that this situation may result in a pullout of the discontinuous beam reinforcement at a substantially smaller force than that when the columns were under large compressive force. More data in this area are in need.

**Effect of infill walls.**

The presence of infill walls parallel to the direction of motion will significantly reduce the large deformations, and the consequent P-$\Delta$ effect generally observed in lightly reinforced concrete structures. The interaction between the lightly reinforced concrete frame and the wall is certainly a major issue that needs to be addressed both experimentally and analytically. LRC buildings typically have rather brittle unreinforced masonary walls that may function well for low levels of acceleration, but will be subjected to very sudden loss of strength with equally sudden transfer of lateral loads to the building columns. LRC columns will not respond well to this type of loading.

**Risk assessment of existing structures.**

Results of both large-scale component tests and small-scale complete structure tests can be incorporated in enhancing the capabilities of program IDARC to accurately predict the response of lightly reinforced concrete structures during earthquakes. The program can then be used to study a wide range of buildings with various configurations and for different ground motions. This study will be very useful in the performance evaluation and risk assessment of building cases other than those tested experimentally.

# CHAPTER 7

# REFERENCES


[1] Abrams, D., "Influence of Axial Force Variations on Flexural Behavior of Reinforced Concrete Columns," ACI Structural Journal Vol. 84, No. 3/ May-June 1987.

[2] ACI Committee 318, "Building Code Requirements for Reinforced Concrete," American Concrete Institute, Detroit 1989.

[3] ACI-ASCE Committee 352, "Recommendations for Design of Beam-Column Joints in Monolithic Reinforced Concrete Structures," ACI Structural Journal Vol. 86, No. 2/ May-June 1985.

[4] Durrani, A., and Wight, J.K., "Earthquake Resistance of Reinforced Concrete Interior Connections Including a Floor Slab," ACI Structural Journal Vol. 84, No. 4/ September-October 1987.

[5] El-Attar, A., White, R.N., and Peter Gergely, "Shake Table Test of A 1/6 Scale Lightly Reinforced Concrete Building", National Center for Earthquake Engineering Research. Technical Report NCEER-91-0017.

[6] ENDEVCO CORPORATION/ DYNAMIC INSTRUMENTS DIVISION, "Instruction Manual For ENDEVCO Peizoresistive Accelerometers", September 1978.

[7] Harris, H.G., Sabnis, G.M., White, R.N., "Small Scale Direct Models of Reinforce and Prestressed Concrete Structures," Report No.326, Department of Structural Engineering, Cornell University, Ithaca, N.Y., September 1966.

[8] Hassoun, M.N., "Design of Reinforced Concrete Structures", PWS Publishers, 1985.

[9] Kim,W., El-Attar, A., and White, R.N. ,"Small-Scale ModeLing Techniques For Reinforced Concrete Structures Subjected To Seismic Loads", National Center for Earthquake Engineering Research. Technical Report NCEER-88-0041, November 22, 1988.

[10] Low, S.S. and Moehle, J.P.,"Experimental Study of Reinforced Concrete Columns Subjected to Multi-Axial Loading", UCB/EERC-87/14, September 1987.

[11] Micro-Measurements Division, Catalog 500/Part A ,"Strain Gage Listing", Measurements Group Inc., P.O. Box 27777, Nc (1989).

[12] MTS SYSTEMS CORPORATION/ MACHINE CONTROLS DIVISION, "TemposonicsTM Linear Transducer System With Analog Output/ Installation and Instruction Manual", 1989.

[13] National Research Council Committee on Earthquake Engineering Research, Earthquake Engineering Research 1982, National Academy Press, 1982.

[14] Reinhorn, A.M., Seidel, M.J., Kunnath, S.K., and Park, Y.J.,"Damage Assessment of Reinforced Concrete Structures In Eastern United States", National Center for Earthquake Engineering Research. Technical Report NCEER-88-0016, June 15, 1989.

[15] Roark, R.J. and Young, W.C., "Formulas for Stress and Strain", Fifth Edition, McGraw-Hill Book Company, New York 1982.

[16] Russo, Gaetano, "Beam Strength Enhancement at Design Ductility Factor Demands," Journal of the Structural Division, ASCE, Vol. 116, No. 12, December 1990.

[17] Park, Y.J., Ang, A.H-S., and Wen, Y.K., "Seismic Damage Analysis and Damage-Limiting Design of R/C Buildings", Civil Engineering Studies, SRS No. 516, University of Illinois, Urbana, October 1984.

[18] Park, Y.J., Reinhorn, A.M., and Kunnath, S.K., "IDARC: Inelastic Danage Analysis of REinforced Concrete Frame-Shear-Wall Structures", National Center for Earthquake Engineering Research. Technical Report NCEER-87-0008, July 20, 1987.

[19] Paulay, T., "A Critique of The Special Provisions for Seismic Design of The Building Code Requirements for Reinforced Concrete (ACI 318-83)," ACI Structural Journrnal Vol. 83, No. 2/ March-April 1986.

[20] Pessiki S.P., Conley, C.H., Gergely, P., and White, R.N., "Seismic Behavior of Lightly-Reinforced Concrete Column and Beam-Column Joint Details", National Center for Earthquake Engineering Research. Technical Report NCEER-90-0014, August 27, 1990.

[21] Shahrooz, B.M., Moehle, J.P., "Experimental Study of Seismic Response of R.C. Setback Buildings," Earthquake Engineering Research Center, University of California/ Berkeley, California. Report No. UCB/EERC-87/16, October 1987.

[22] STRAND-2D, A Program for STRuctural ANalysis and Design of Two dimensional Plane Frame Structures, Group 2000 Engineering Corp., 3520 Long Beach Boulevard, Long Beach, California 90807.

[23] Zerbe, H.E., and Durrani, A., "Seismic Response of Connections in Two-Bay Reinforced Concrete Frame Subassemblies with Floor Slab ," ACI Structural Journal Vol. 87, No. 4/ July-August 1990.

# Appendix A

# 3-Story Building Design

## A.1 Prototype design

### A.1.1 Design Loads

The prototype 3-story building was designed for gravity loads of self weight, and live load of 50 psf for the first and the second floors and 55 psf for the roof. The slab thickness was estimated according to the ACI 318-83 code (section 9.5) as follows:

Assume $h$ = 6", and a 9" × 18" beam (figure A.1.a).

$\overline{y}$ $= 11.82"$

$I_b$ $= \frac{33\times6^3}{12} + 6 \times 33 \times (15 - 11.82)^2 + \frac{9\times6^3}{12} + 9 \times 12 \times (11.82 - 6)^2$

$= 7573\ in^4$

$I_s$ $= 18 \times 12 \times \frac{6^3}{12} = 3888\ in^4$

$\alpha_m$ $= \frac{E_c\times I_b}{E_c\times I_s} = \frac{7573}{3888} = 1.95$

$\beta_s$ $= 0.5$

$\beta$ $= 1.0$

$l_n$ $= 207"$

$f_y$ $= 40{,}000$ ksi

$h$ $\geq \frac{l_n(800+0.005\times f_y)}{36{,}000+5000\times\beta(\alpha_m-0.5(1-\beta s))(1+\frac{1}{\beta})}$

$\geq \frac{207(800+0.005\times40{,}000)}{36{,}000+5000\times1(1.95-0.5(1-0.5))\times2} \geq 4.79"$

$h$ $\geq \frac{l_n(800+0.005\times f_y)}{36{,}000+5000\times\beta(1+\beta_s)}$

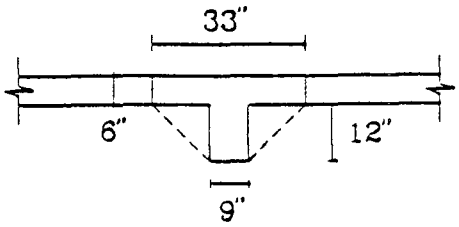


Figure A.1: Beam Cross Sections Used for Slab Thickness Calculation.

$$h \geq \frac{207(800+0.005\times 40{,}000)}{36{,}000+5000\times 1.5(1+0.5)} \geq 4.76"$$

$$h \geq \frac{l_n(800+0.005\times f_y)}{36{,}000}$$

$$\geq \frac{207(800+0.005\times 40{,}000)}{36{,}000} \geq 5.75" \text{ (governs).}$$

Use a slab thickness $h$ equal to 6". The design loads for the 3-story building are summarized in table A.1.

Table A.1: Loads on Prototype 3-Story Building

| Item | First and Second stories | Top story |
|---|---|---|
| Dead load | | |
| Slab (6 inches thick) | 0.075 $k/ft^2$ | 0.075 $k/ft^2$ |
| Ceiling | 0.008 $k/ft^2$ | 0.008 $k/ft^2$ |
| Exterior Wall on transverse girders (8" block + 4" brick)) | 0.562 $k/ft$ | — |
| Partitions | 0.020 $k/ft^2$ | — |
| Asphalt tile | 0.001 $k/ft^2$ | 0.001 $k/ft^2$ |
| Live Load | 0.050 $k/ft^2$ | 0.055 $k/ft^2$ |

## A.1.2 Equivalent frame method

The "Equivalent frame method" (ACI 318-89 section 13.7) was adopted for the floor design. Design details are introduced in the following paragraphs.

### Relative member stiffnesses

### Beams:

For a 9" × 18" beam, and 6" slab, the inertia of an interior beam-slab section

(figure A.1.b) becomes:

$\overline{y} = \frac{216\times6\times15+9\times12\times6}{216\times6+9\times12} = 14.31"$

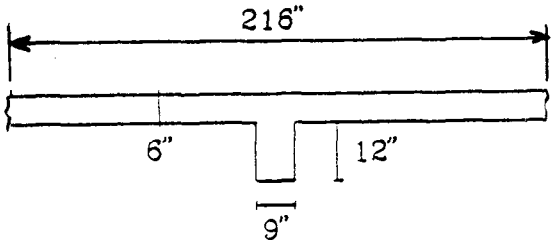


(b) Interior Beam Cross Section.

$I_{s_{interior}} = \frac{9\times12^3}{12} + 9 \times 12 \times 8.308^2 + \frac{216\times6^3}{12} + 216 \times 6 \times 0.692^2 = 13259\ in^4$

And for an exterior beam (figure A.1.c),

$\overline{y} = 13.75"$

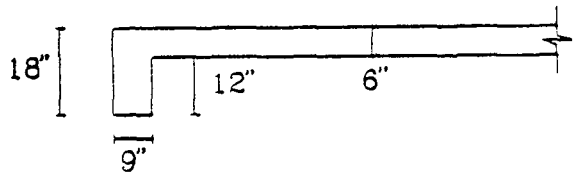


(c) Exterior Beam Cross Section.

$I_{s_{exterior}} = \frac{9\times12^3}{12} + 9 \times 12 \times 7.754^2 + \frac{112\times6^3}{12} + 112 \times 6 \times 1.246^2 = 10849\ in^4$

Distribution and carry-over factors are computed using the column analogy method. For the analogous beam shown in figure A.2.a, the following properties are obtained:

Area (A) $= \frac{17}{EI} + \frac{0.892}{EI} = \frac{17.892}{EI}$

Inertia (I) $= \frac{17^3}{12\times EI} + 2 \times [\frac{0.892}{EI} \times \frac{0.5^3}{12} + \frac{0.892}{EI} \times 0.5 \times 8.75^2] = \frac{477.73}{EI}$

$K_{a-b} = \frac{EI}{17.892} + 9.0 \times 9.0 \times \frac{EI}{477.73} = 4.058\ \frac{EI}{L}$

$K_{b-a} = \frac{EI}{17.892} - 9.0 \times 9.0 \times \frac{EI}{477.73} = 2.046\ \frac{EI}{L}$

$C.O.F = \frac{2.046}{4.058} = 0.504$

**Torsional stiffness of beams:**

Torsional stiffness of an interior beam $K_t$ is computed as follows (figure A.2.b):

$C = \sum(1 - 0.63 \times \frac{x}{y})\frac{x^3y}{3}$

$C_1 = (1 - 0.63 \times \frac{9}{18})\frac{9^3\times18}{3} + 2(1 - 0.63 \times \frac{6}{12})\frac{6^3\times12}{3} = 4180\ in^4$ (governs)

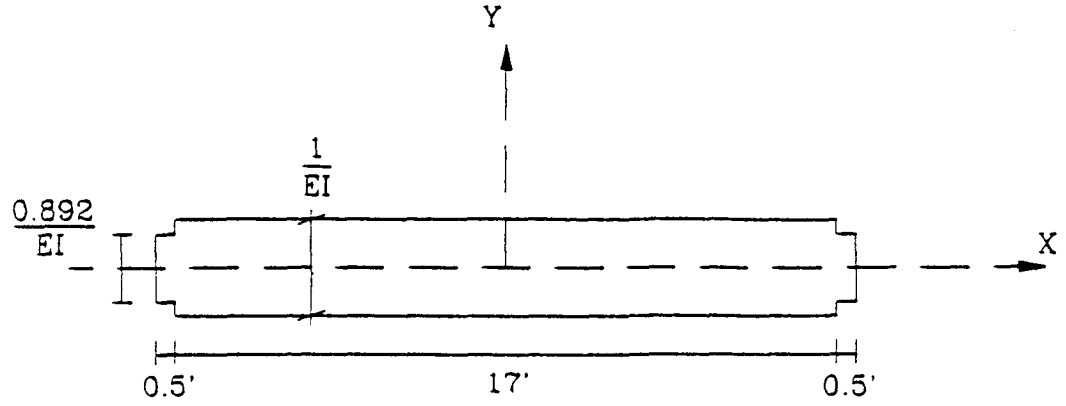


(a) Beam Analogous Section.

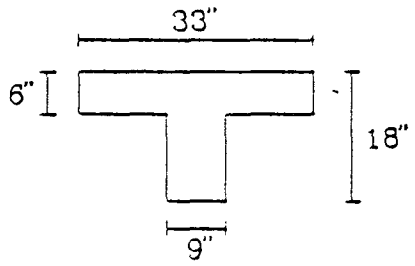


(b) Interior Beam Section Used For Torsional Stiffness Calculation.

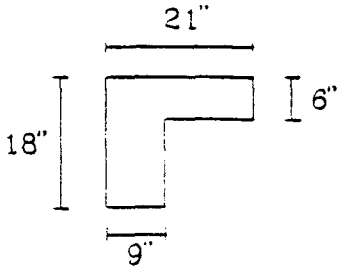


(c) Exterior Beam Section Used for Torsional Stiffness Calculations.

**Figure A.2: Different Beam Sections Used for Stiffness Calculations.**

$$C_2 = (1 - 0.63 \times \tfrac{9}{12})\tfrac{9^3 \times 12}{3} + 2(1 - 0.63 \times \tfrac{6}{33})\tfrac{6^3 \times 33}{3} = 3642\ in^4$$

For C= 4180 $in^4$, $K_t$ will be equal to:

$$K_{t_{interior}} = \frac{9E_c \times C}{l_2(1-\frac{c_2}{l_2})^3} \times \frac{I_{bt}}{I_t} = \frac{9E_c \times 4180}{216(1-\frac{12}{216})^3} \times \frac{13259}{3888} = 705\ E_c$$

For an exterior beam (figure A.2.c):

$$C = (1 - 0.63 \times \tfrac{9}{18})\tfrac{9^3 \times 18}{3} + (1 - 0.63 \times \tfrac{6}{12})\tfrac{6^3 \times 12}{3} = 3588\ in^4$$

$$K_{t_{exterior}} = \frac{9E_c \times 3588}{216(1-\frac{12}{216})^3} \times \frac{13259}{3888} = 605\ E_c$$

## Columns:

For the analogous column shown in figure A.3, the following properties can be obtained:

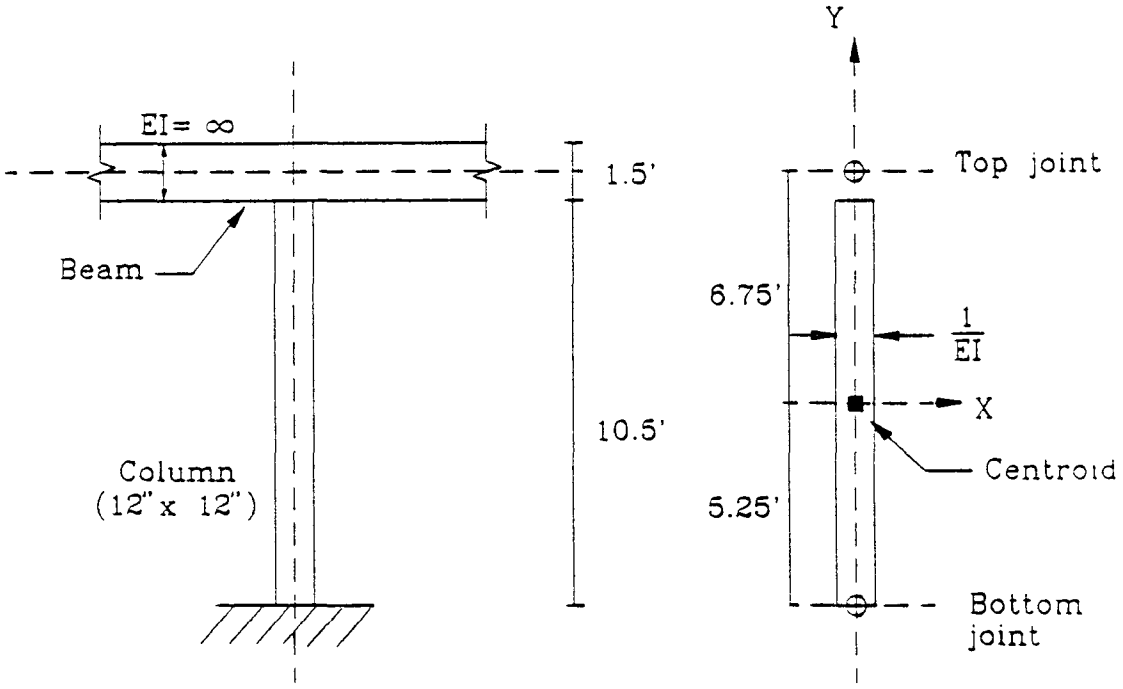


Figure A.3: Column Analogy Section.

Area (A) $= \frac{10.5}{EI}$

Inertia (I) $= \frac{10.5^3}{12 \times EI} = \frac{96.5}{EI}$

$M_{tt} = (\frac{1}{10.5} + \frac{6.75^2}{96.5}) \times 12 \times EI = 6.81EI$

$M_{tb} = (\frac{1}{10.5} - \frac{6.75 \times 5.25}{96.5}) \times 12 \times EI = 3.26EI$

$M_{tt} = (\frac{1}{10.5} + \frac{5.25^2}{96.5}) \times 12 \times EI = 4.57EI$

The carry over factors will then be given by:

$C.O.F_{tb} = \frac{3.26}{6.81} = 0.479$

$C.O.F_{bt} = \frac{3.26}{4.57} = 0.714$

Column top and bottom stiffness also become:

$K_{top} = \frac{6.81 \times EI}{L} = \frac{6.81 \times 12^3 E}{144} = 81.72$ E

$K_{bottom} = \frac{4.57 \times EI}{L} = \frac{4.57 \times 12^3 E}{144} = 54.84$ E

**Equivalent Frame:**

The relative member stiffnesses for an equivalent longitudinal frame (in the direction of shaking) can be obtained as follows:

Floor:

$I_s \quad = 13259\ in^4$

$K_s \quad = 4.06 \times \frac{13259}{216} \times E_c = 249\ E_c$

$C.O.F \ = 0.504$

Columns:

For an interior column;

$I_c \quad = \frac{12 \times 12^3}{12} = 1728\ in^4$

$K_c \quad = 81.72\ E_c$

$C.O.F_{tb} = \frac{3.26}{6.81} = 0.479$

$C.O.F_{bt} = \frac{3.26}{4.57} = 0.714$

$\frac{1}{K_e} \quad = \frac{1}{[K_{top}+K_{bottom}]} + \frac{1}{2 \times K_t} = \frac{1}{[54.84+81.72] \times E_c} + \frac{1}{2 \times 705 \times E_c}$

$K_e \quad = 125\ E_c$

And for an exterior column;

$\frac{1}{K_e} \quad = \frac{1}{[54.84+81.72] \times E_c} + \frac{1}{2 \times 605 \times E_c}$

$K_e \quad = 123\ E_c$

The relative member stiffnesses, along with the distribution and carry-over factors are shown in figure A.4.a and b, respectively. The bending moments due to the factored dead and live loads on all the spans are shown in figure A.5. Lateral distribution of bending moments is computed according to section 13.6.4 of the ACI-318 code [2], and results are shown in figure A.6.

## A.1.3 Design of beams

### Longitudinal beam

The bending moments acting on the first story longitudinal beam are shown in figure A.7.a. The beam cross section dimensions are as follows:

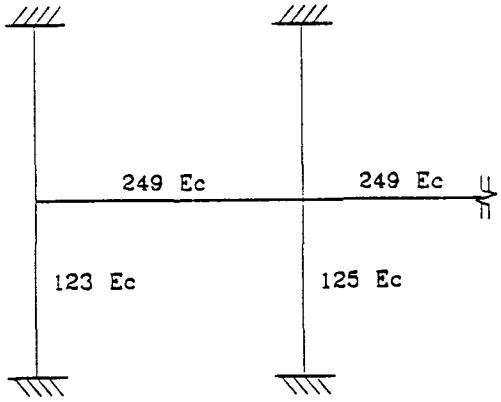


(a) Relative Member Stiffnesses.

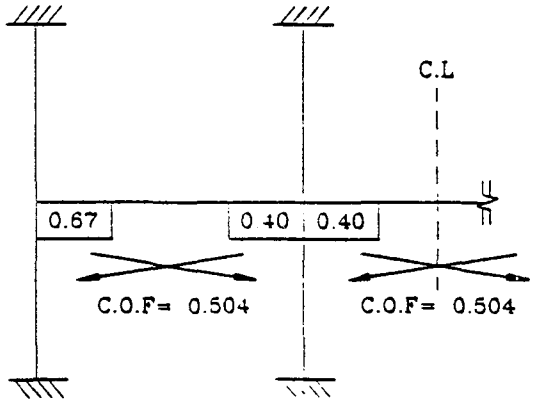


(b) Distribution and Carry-Over Factors.

Figure A.4: Distribution and Carry-Over Factors for The Moment Distribution.

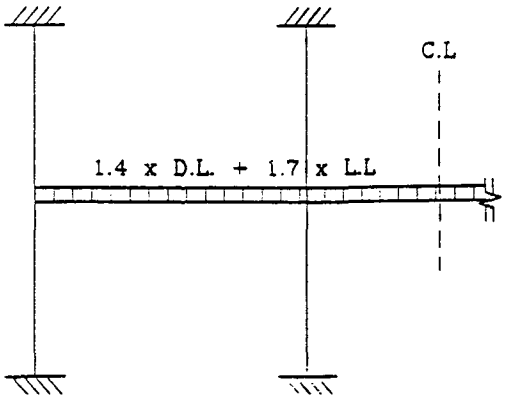


(a) Design Load Case.

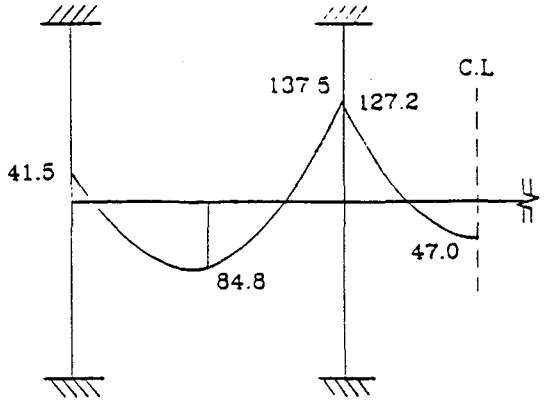


(b) Total Floor Moments.

Figure A.5: Floor Design Moments.

Thickness (h) $= 18"$

Depth (d) $= 18 - 2 = 16"$

Breadth (b) $= 9"$

Slab thickness ($t_s$) $= 6"$

Section (1):

$M_n = \frac{M_n}{0.9} = \frac{73.75}{0.9} = 81.94$ k.ft $= 983$ k.in

$= 0.85 \times 3500 \times 9 \times a \times (16 - \frac{a}{2}) \rightarrow$ a= 2.489"

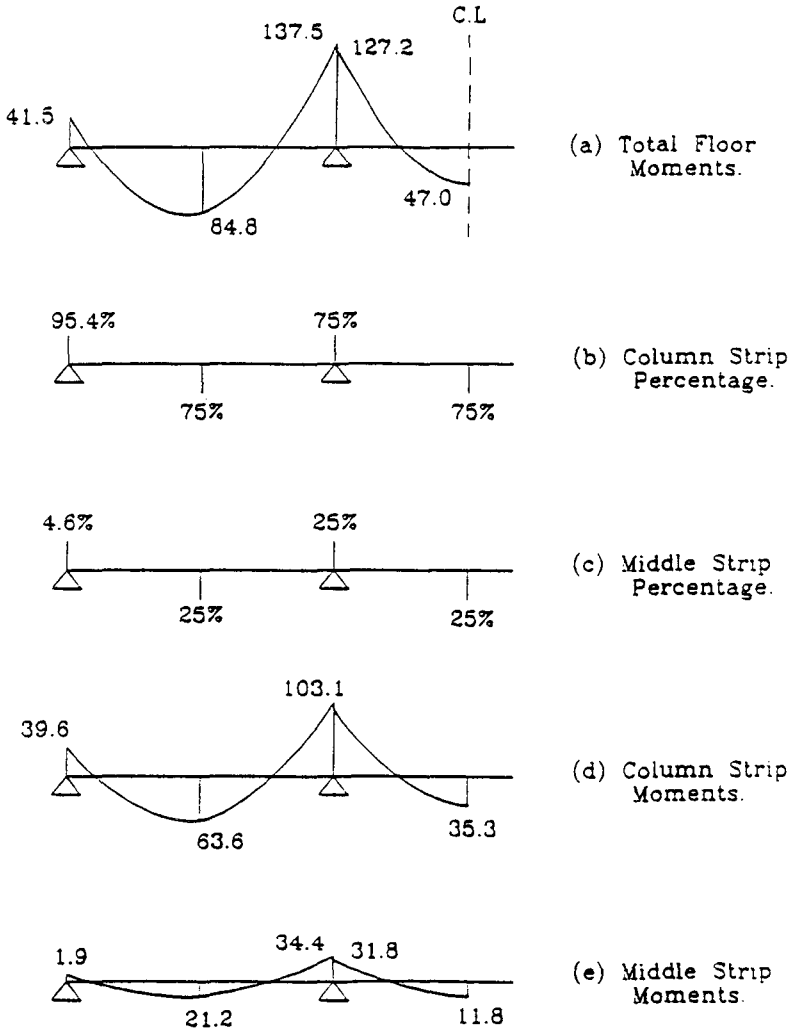


**Figure A.6: Lateral Distribution of Bending Moments.**

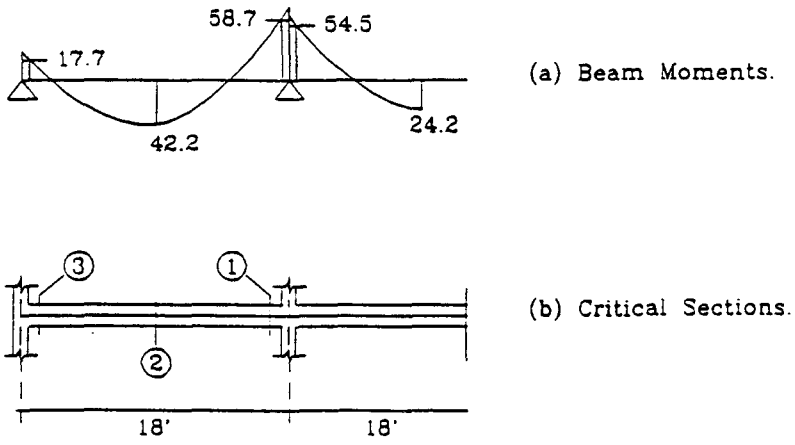


**Figure A.7: Beam Design Moments.**

$= A_s \times 40 \times 16 - \frac{2.489}{2} \rightarrow A_s = 1.67\ in^2 \rightarrow 2\sharp 9$

Section (2):

$M_n = \frac{M_n}{0.9} = \frac{54.1}{0.9} = 59$ k.ft $= 708$ k.in

$= 0.85 \times 3500 \times 54 \times a \times (16 - \frac{a}{2}) \rightarrow$ a= 0.279"

$= A_s \times 40 \times 16 - \frac{0.279}{2} \rightarrow A_s = 1.12\ in^2 \rightarrow 2\sharp 7$

Section (3):

$M_n = \frac{M_n}{0.9} = \frac{25.02}{0.9} = 27.8$ k.ft $= 333.6$ k.in

$= 0.85 \times 3500 \times 9 \times a \times (16 - \frac{a}{2}) \rightarrow$ a= 0.797"

$= A_s \times 40 \times 16 - \frac{0.797}{2} \rightarrow A_s = 0.53\ in^2 \rightarrow 2\sharp 5$

For shear reinforcement, use 3♯8 @ 8" spacing. Edge beams were designed in a similar fashion to that of the longitudinal beams.

## A.1.4 Design of columns

### Column design loads

According to figure A.7, the area carried by each column is given by:

Area carried by column C1 $= 18 \times (0.6 + 0.5) \times (18 \times 0.4 + 2.0) = 182\ ft^2$

Area carried by column C2 $= 18 \times (0.6 + 0.5) \times 18 \times (0.6 + 0.5) = 392\ ft^2$

Column own weight = 1.6 k/floor

Beam load = 0.113 k/ft

Wall load = 0.562 k/ft

**First story columns:**

Interior column $C_2$:

$P_u$ = 300 kips

Table A.2: Column Loads

| Column | C1 | | | C2 | | |
|---|---|---|---|---|---|---|
| Story | $3^{rd}$ | $2^{nd}$ | $1^{st}$ | $3^{rd}$ | $2^{nd}$ | $1^{st}$ |
| Area carried ($ft^2$) | 182 | | | 392 | | |
| Live load ($k/ft^2$) | 55 | 50 | 50 | 55 | 50 | 50 |
| Dead load ($k/ft^2$) | 94 | 109 | 109 | 94 | 109 | 109 |
| Reduction factor R% | 1 | 14 | 27 | 14 | 40 | 60 |
| $(1-R)\%$ | 99 | 86 | 73 | 86 | 60 | 40 |
| Live load $\times(1-R)\%$ $\times Area$ (kips) | 9.98 | 7.83 | 6.65 | 20.46 | 11.76 | 7.84 |
| Deal load $\times Area$ (kips) | 17.12 | 19.86 | 19.86 | 36.85 | 42.73 | 42.73 |
| Column own weight (kips) | 1.57 | 1.57 | 1.57 | 1.57 | 1.57 | 1.57 |
| Beam load (kips) | 3.04 | 3.04 | 3.04 | 4.46 | 4.46 | 4.46 |
| Wall Load (kips) | — | 11.11 | 11.11 | — | — | — |
| $P_{L.L.}$ (kips) | 10.02 | 9.11 | 9.11 | 21.56 | 19.60 | 19.60 |
| $P_{D.L.}$ (kips) | 21.74 | 32.55 | 32.55 | 42.89 | 48.77 | 48.77 |
| $P_u$ (kips) | 47.40 | 108.46 | 169.51 | 96.70 | 198.30 | 299.89 |

$M_L - M_R = 137.5 - 127.2 = 10.3$ k.ft

This moment will be distributed according to the relative stiffness of the first and second story columns (figure A.5) as follows:

$M_u = 10.3 \times \frac{81.72}{81.72+54.34}$ k.ft

$\beta_d = \frac{M_{D.L.}}{M_{D.L.}+M_{L.L.}} = 0.64$

Column stiffness can be estimated as follows:

For $A_s = A_s' = 0.01\ A_c = 1.44" \rightarrow 2\ \sharp 8$, and

$E_c = 57,000\sqrt{f_c'} = 57,000\sqrt{3500} = 3{,}372$ ksi

$I_g$ $= 1827\ in^2$

$I_s$ $= 1.57 \times 3.5^2 \times 2 = 34.47\ in^2$, the column stiffness $EI$ would be given by:

$EI$ $= \frac{0.2\ E_c\ I_g + E_s\ I_s}{\beta_d} = 1.391 \times 10^6\ lb.in^2$ or;

$= \frac{0.4\ E_c\ I_g}{\beta_d} = 1.421 \times 10^6\ lb.in^2$ (governs)

Slenderness effect:

$I_{col}$ $= 1728\ in^4$

$I_{beam}$ $= 0.5 \times 13259 = 6629.5\ in^4$ (figure A.8)

$l_u$ $= 12 \times 12 - 18 = 126$"

$\psi_{bottom}$= 0.0 (fixed support)

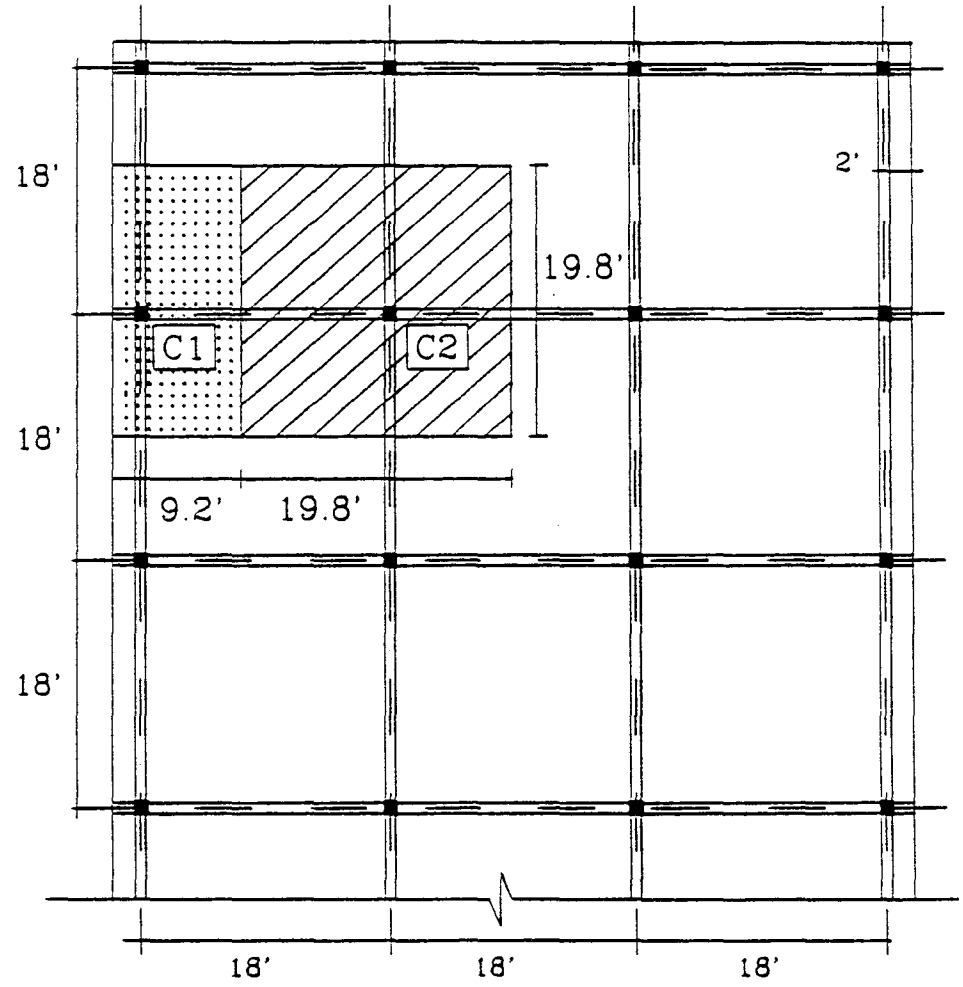


Plan of The 3-Story Building.

**Figure A.8: Area Carried by Columns C1 and C2.**

$\psi_{top} = \frac{2\times1728\times216}{2\times6629.5\times126} = 0.447$

$\psi_{mean} = \frac{\psi_{bottom}+\psi_{top}}{2} = 0.223$

$K = \frac{20-\psi_m}{20} \times \sqrt{1+\psi_m} = \frac{20-0.223}{20} \times \sqrt{1+0.223} = 1.094$

$K \times l_u = 137.8"$

$P_{cr} = \frac{\pi^2\times EI}{(K\times l_u)^2} = \frac{\pi^2\times1.421\times10^6}{137.8^2} = 739$ kips

For an exterior column, the critical load $P_{cr}$ can be computed as follows:

$\psi_{bottom} = 0.0$ (fixed support)

$\psi_{top} = \frac{2\times1728\times216}{6629.5\times126} = 0.894$

$\psi_{mean} = \frac{\psi_{bottom}+\psi_{top}}{2} = 0.447$

$K = \frac{20-0.447}{20} \times \sqrt{1+0.447} = 1.176$

$K \times l_u = 148.2"$

$P_{cr} = \frac{\pi^2\times EI}{(K\times l_u)^2} = \frac{\pi^2\times1.421\times10^6}{148.2^2} = 639$ kips

The magnification factor $\delta$ will be equal to:

$\delta = \frac{1}{1-(\frac{\sum P}{0.7\times\sum P_{cr}})} = \frac{1}{1-(\frac{170+300}{0.7\times[739+639]})} = 1.95$

$M_n = 1.95 \times 6.146 = 12$ kips.ft

Eccentricity (e) $= \frac{12\times12}{300} = 0.48$ inch

Assume a column reinforcement of 4#6, then $P_n$ can be computed as follows:

$P_n = \frac{bhf_c'}{(\frac{3he}{d^2})+1.18} + \frac{A_s'f_y}{(\frac{e}{d-d'})+0.5}$ (Whitney equation [8])

$P_n = \frac{12\times12\times3.5}{(\frac{3\times12\times0.48}{9.5^2})+1.18} + \frac{0.884\times40}{(\frac{0.48}{7})+0.5} = 367.5 + 62.2 = 430$ kips

$> \frac{300}{0.7} > 428$ kips

A minimum shear reinforcement of #3 bars at 12" spacing is used for column C2.

Exterior column $C_1$:

$P_u$ = 170 kips

$M_u$ = $41.46 \times \frac{81.72}{81.72+54.84}$ = 24.8 kips.ft

$M_n$ = $1.95 \times 24.81$ = 48.4 kips.ft

e = $\frac{48.4 \times 12}{170}$ = 3.415 inch

Assume a column reinforcement of 4#6, then $P_n$ will be given by:

$$P_n = \frac{bhf_c'}{(\frac{3Ae}{d^2})+1.18} + \frac{A_s' f_y}{(\frac{e}{d-d'})+0.5}$$

$$P_n = \frac{12\times12\times3.5}{(\frac{3\times12\times3.415}{9.5^2})+1.18} + \frac{0.884\times40}{(\frac{3.415}{7})+0.5} = 234 \text{ kips} \simeq \frac{170}{0.7} = 242 \text{ kips}$$

For the shear reinforcement, also use #3 bars at 12" spacing.

The same dimensions and steel reinforcement were used for all the three story columns. Lap splices were located immediately above the floor level and with a common length of 24 times the bar diameter (18" in the present case). Reinforcement details of the 3-story model are presented in figures 3.14 and 3.15 in chapter 3.

# Appendix B

# Load Cell Design, Fabrication, and Calibration

## B.1 Cell Design

### B.1.1 Introduction

Since the 3-story model structure was shaken in only one direction, it was decided that the internal-force transducers (load cells) should be capable of measuring the axial force, bending moment and shearing force in the direction of motion, and the shearing force normal to the direction of motion. The first step in the design of load cells was to establish their location in the structure. These locations were selected so that they (a) provide the desired information about the structure subassembalge, (b) develop minimum disturbance to the host member mass and stiffness, and (c) allow an easy and economic installation of the transducer. Once the locations of the transducers in the structure were determined, their design loads could be evaluated using approximate analytical methods along with the calculated capacities of the host structural members. Other important design considerations of the load cells were: (d) linearity and repeatability of the strain measurements, (e) independent measurements of strains induced by forces in different directions, and finally (f) ease and economy of fabrication.

For the present case of the 3-story office building, the mid-heights of the first and the second story columns were selected as the load cell positions. It can be seen

from figure B.1 that the selected locations for the load cells will reduce the first floor of the structure to a statically determinate subassemblage where all straining actions in the beams, columns, and joints can be obtained.

### B.1.2 Mechanical Design and Fabrication

The load cell was designed for (1) an axial force of 3.0 kips, (2) a bending moment of 0.5 kips.inch, (3) a shearing force in the direction of motion of 2.0 kips, and (4) a shearing force normal to the direction of motion of 2.0 kips. The cell dimensions were selected so that they satisfy the following requirements:

- Stresses in the load cell should be well below the yield stress to ensure linearity and repeatability of the cell readings.
- Buckling load of the cell walls must be far above the service load to ensure linearity of the cell readings.
- Contribution of the load cell to the column stiffness should be minimal (less than 10%).

The cell body was composed of a 1.5" × 1.5" × 0.125" structural steel tube, with a total height of 1.5" (figure B.2). Based on the cell design, the thickness of the middle 1" of the cell walls was machined down to 0.0625" to increase the cell sensitivity, leaving the upper and lower 0.25" of the tube walls at the original thickness. This provided more uniform heat transfer between the cell walls and the base plates so that satisfactory weld pendtration can be achieved. The welding throat was about 0.125" all around the tube edges.

Two relatively thick base plates (3" × 3" × 0.5") were welded to the top and

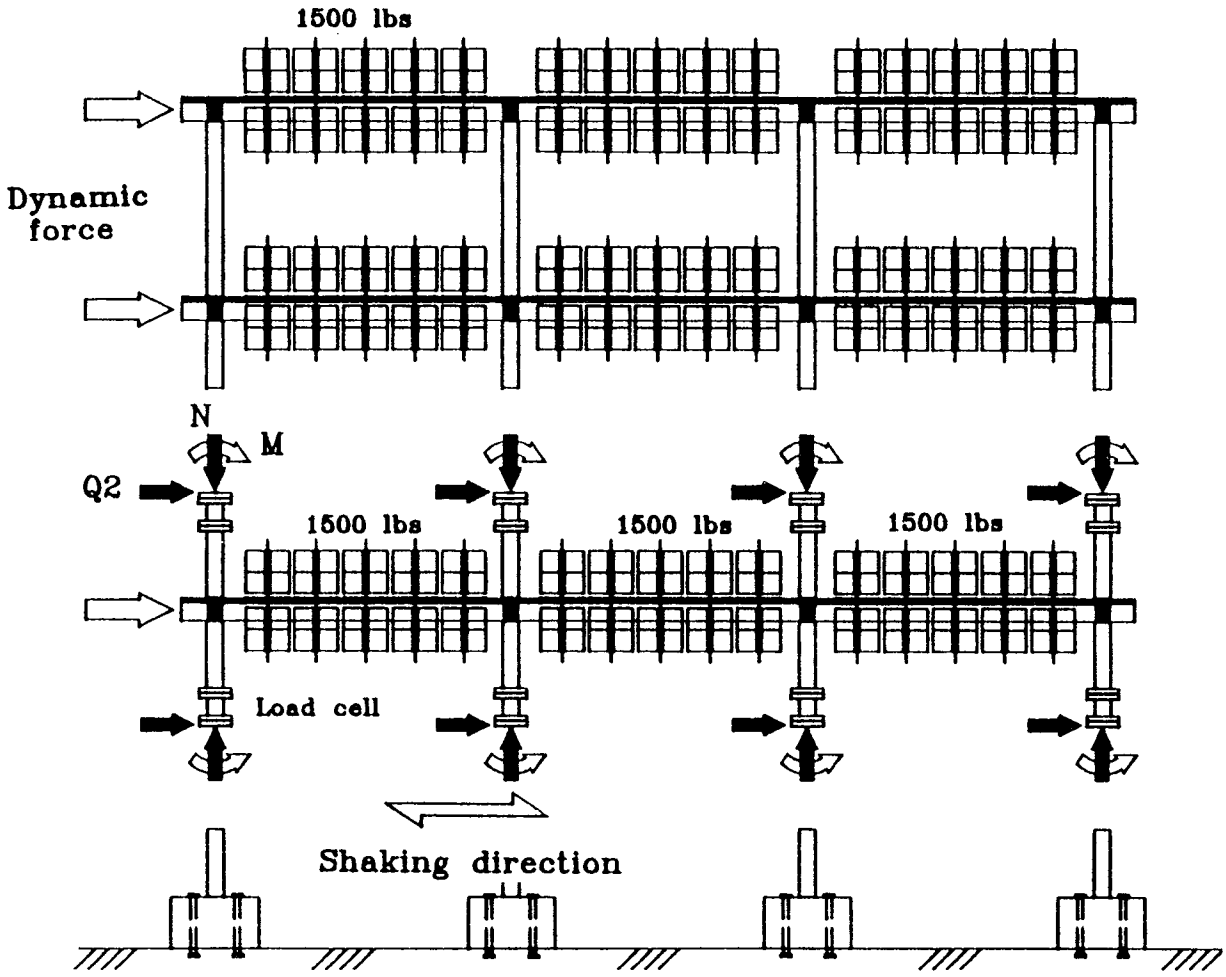


Figure B.1: Forces Acting on The First Story During Seismic Tests.

bottom bases of the steel tube to ensure uniform distribution of stresses over the cell cross section and to facilitate its installation. Each plate had a 1 inch central hole to provide access to the inside face of the tube.

The load cell was heat treated at 600 degrees $C$ for 8 hours to relieve all residual stresses resulting from the welding process. The cell was then sand blasted to clean its surface and to roughen the cell walls for mounting the strain gages. The cell body (except for the strain gages locations) was plated with bright Nickel to protect it against corrosion.

## Straining actions on the cell

Properties of area of the cell cross section were calculated as follows;

$$a = 4 \times 0.0625 \times 1.3125 = 0.328\ inch^2$$

$$I = 2 \times 1.3125 \times 0.0625 \times \frac{1.31252^2}{2} + 2 \times 0.0625 \times \frac{1.3125^2}{12}$$

$$= 0.0421\ inch^4$$

where:

a = cross sectional area of the cell.

I = second moment of area of the cell cross section.

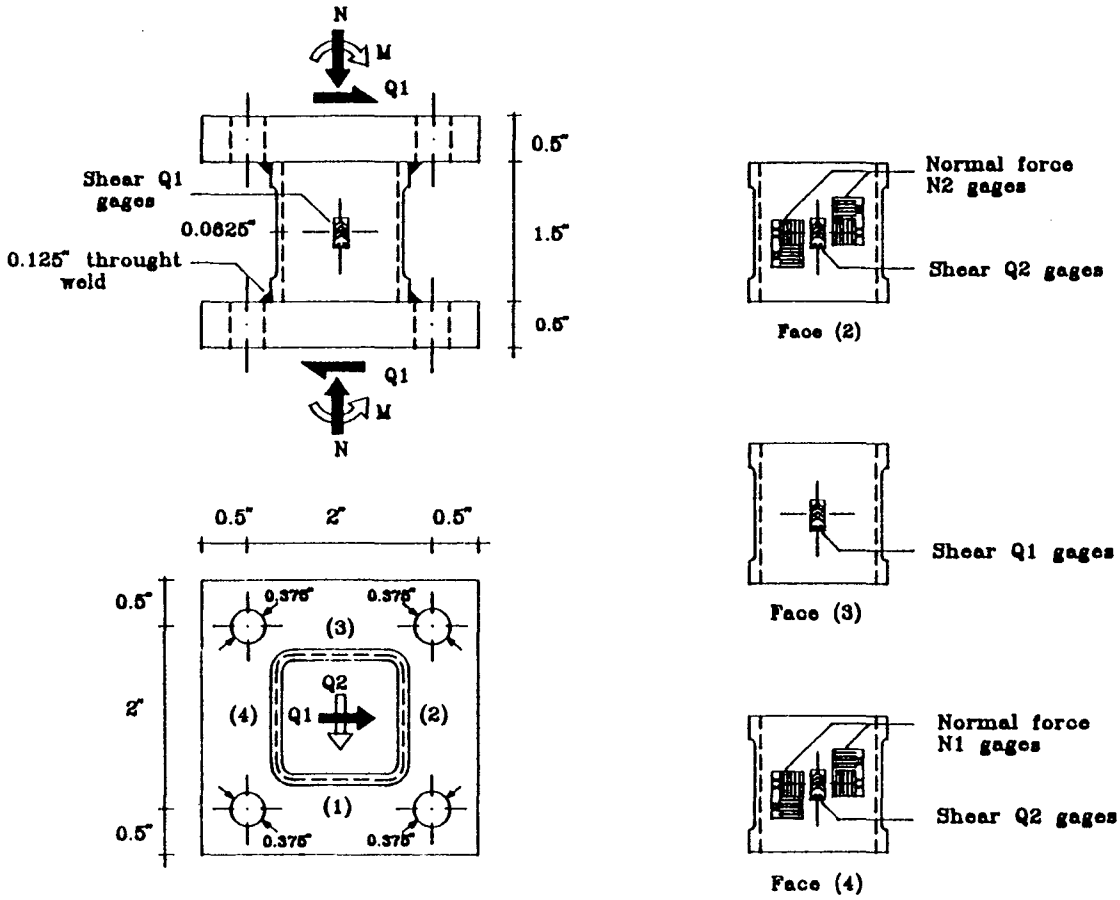


Figure B.2: Load Cell Dimensions and Strain Gaging.

The maximum stresses acting on the infinitsimal element shown in figure B.3 are then given by;

Shearing stresses $\tau = \frac{2}{2\times1.3125\times0.0625} = 12.19\ ksi$

Bending stresses $\sigma_b = \frac{2\times1.3125}{2\times0.09421} = 13.94\ ksi.$

Normal stresses $\sigma_n = \frac{3.0}{0.328} = 9.146\ ksi.$

The maximum principal stresses on the element were computed as follows;

$$\sigma_{max,min} = \frac{\sigma_x+\sigma_y}{2} \pm \sqrt{\frac{\sigma_x+\sigma_y}{2} + {\tau_{xy}}^2}$$

$$= -11.54 \pm 16.79 = +5.25\ ,\ -28.33\ ksi$$

It can be seen that both stresses are well below the nominal yield stress ($f_y = 60ksi$) of the cell walls.

### Stability of the cell walls

The stability of the cell walls against local buckling was checked assuming (conservatively) that each of the cell walls will act as a plate simply supported on four sides (figure B.4). The critical normal stresses and shear stresses were computed as follows [15];

Shear stresses;

$\frac{L_1}{L_2} = 1.0 \Rightarrow K = 7.75$

$\tau_{cr} = k \times \frac{E}{1-\nu^2} \times (\frac{t}{b})^2 = 416$ ksi.

Normal stresses;

$\frac{L_1}{L_2} = 1.0 \Rightarrow K = 7.75$

$\sigma_{cr} = k \times \frac{E}{1-\nu^2} \times (\frac{t}{b})^2 = 177$ ksi.

It can be seen that both stresses are much higher than those acting on the cell

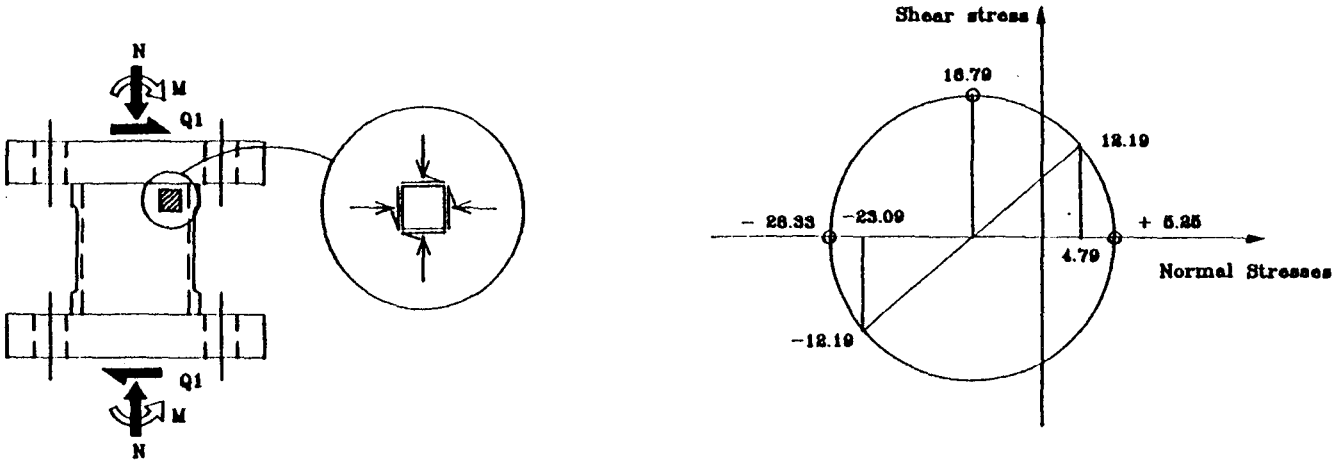


Figure B.3: Principal Stresses in The Cell Walls.


(a) Under Axial Force

(b) Under Shear Force.

Figure B.4: Stability of The Cell Walls.

walls due to the design shearing force and axial force.

### Cell contribution to the column stiffness

The column analogy method was used to estimate the effect of the presence of the load cell on the column stiffness in the elastic range. The properties of both the column and the cell cross sections were evaluated as follows;

$$EI_{col.} = 2,400 \times \frac{1.125 \times 2.25^3}{12} = 2,363\ kips.inch^2$$

$$EI_{cell} = 29,000 \times (0.0625 \times \frac{1.5^3}{12} \times 2 + 0.0625 \times 1.5 \times 0.75^2 \times 2$$

$$= 4,078\ kips.inch^2)$$

$$\frac{EI_{cell}}{EI_{col.}} = 1.6$$

The properties of the analogous section shown in figure B.5 then become:

$$\text{Area (A)} = 0.858\ \frac{L}{EI}$$

$$\text{Inertia (I)} = \frac{L}{EI} \times (0.625 \times \frac{0.083^3}{12} + [\frac{0.403^3}{12} + 0.403 \times 1 \times 0.2985^2] \times 2)$$

$$= \frac{L^3}{12.084 \times EL}$$

The stiffness matrix coefficients of the instrumented column were computed as follows;

- For a unit displacement at node (1) (figure B.5.a), the straining actions on the analogous section are N = 0, and M = 1.0 Resulting in the following stiffness coefficients;

$$K_{12} = \quad K_{14} = \frac{M \times Y}{I} = \frac{L}{2} \times 12.084 \frac{EI}{L^3} = 6.042\ \frac{EI}{L^2}$$

$$K_{11} = -K_{13} = 2 \times 6.042 \frac{EI}{L^2} \times \frac{1}{L} \qquad = 12.084\ \frac{EI}{L^3}$$

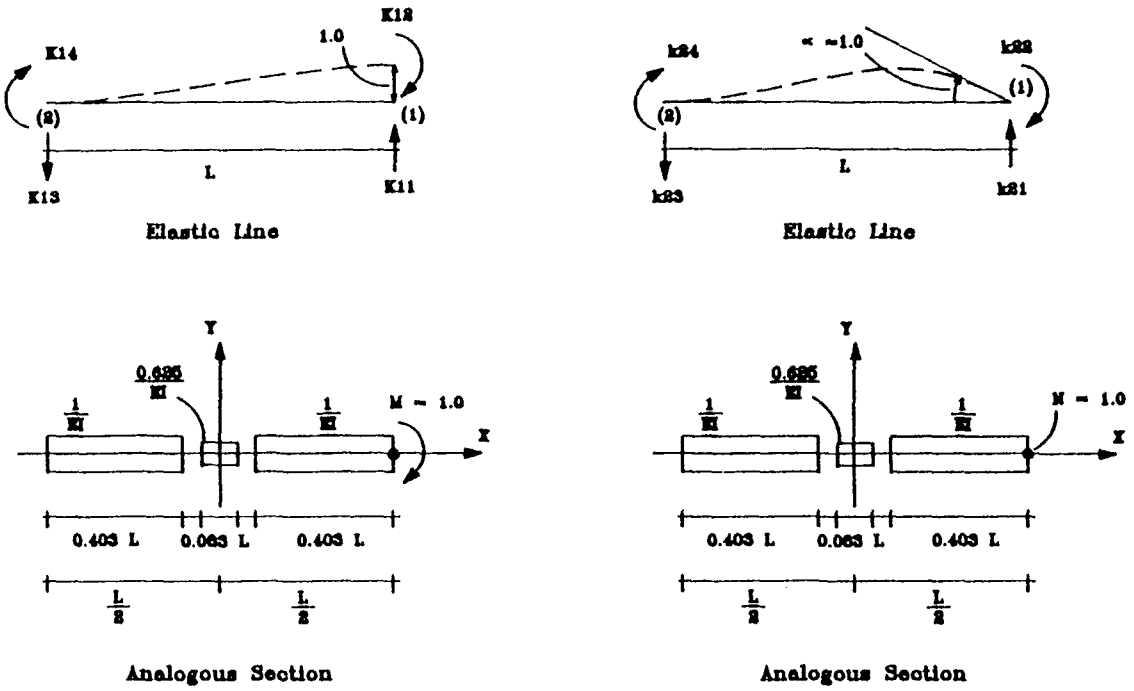


(a) Due to Unit Displacement at Node (1).

(b) Due to Unit Rotation at Node (1).

Figure B.5: Stiffness Matrix Coefficients of The Instrumented Column Using The Column Analogy Method.

- For a unit rotation at node (1) (figure B.5.b), the straining action on the analogous section become N = 1.0, and M = $\frac{L}{2}$ resulting in the following stiffness coefficients;

$$K_{22} = \frac{N}{A} + \frac{M \times Y}{I} = \frac{EI}{0.858L} + \frac{L}{2} \times \frac{L}{2} \times 12.084\frac{EI}{L^3} = 4.187\ \frac{EI}{L}$$

$$K_{24} = -\frac{N}{A} + \frac{M \times Y}{I} = -\frac{EI}{0.858L} + \frac{L}{2} \times \frac{L}{2} \times 12.084\frac{EI}{L^3} = 1.856\ \frac{EI}{L}$$

$$K_{21} = -K_{23} = \frac{1}{L} \times 4.187\frac{EI}{L} + 1.856\frac{EI}{L} = 6.042\ \frac{EI}{L^2}$$

The stiffness matrix of the column then becomes;

$$[K]_{4\times4} = \begin{bmatrix} k_{11} & k_{12} & k_{13} & k_{14} \\ k_{21} & k_{22} & k_{23} & k_{24} \\ k_{31} & k_{32} & k_{33} & k_{34} \\ k_{41} & k_{42} & k_{43} & k_{44} \end{bmatrix} = \frac{EI}{L} \begin{bmatrix} \frac{12.084}{L^2} & \frac{6.042}{L} & \frac{-12.084}{L^2} & \frac{6.042}{L} \\ \frac{6.042}{L} & 4.187 & \frac{-6.042}{L} & 1.856 \\ \frac{-12.084}{L^2} & \frac{-6.042}{L} & \frac{12.084}{L^2} & \frac{-6.042}{L} \\ \frac{6.042}{L} & 1.856 & \frac{-6.042}{L} & 4.187 \end{bmatrix}$$

It can be seen that the maximum difference between the instrumented column and the non-instrumnented column stiffness matrix coefficients does not exceed 8% (for $k_{24}$ case). Since previous experience at Cornell [2] with similar structures indicated that most of the nonlinear column response takes place near the joint region, it was decided that these differences are not significant.

### B.1.3 Electronic Design

The electronic design of the load cell was carried out in conjunction with the selected material and mechanical design of the cell. It included the selection of strain gages, bonding agent, configuration of the gages, and the circuity for each internal force channel. Each of these items will be discussed in the following paragraphs.

The selection of the strain gages was based on the following guide-lines;

- The size of the strain gages should be small enough to average the strains over a uniform strain field, and away from the strain turbulence at the wall edges.
- The size of the strain gages should also be large enough to facilitate accurate alignment and easy wiring.
- Fatigue life of the strain gages should be sufficient to resist the expected dynamic loading. This is of particular importance for small scale models,

where the model frequency will be much higher than that of the prototype structure.

- The strain gages should be self temperature compensating (STC) to match the test material expansion coefficient.
- Finally, the selected gages should be rugged and tough, especially when the load cell is designed for long term use.

The selected gages were Polyimide-encapsulated Constantan gages, with a grid size of 0.125" × 0.125" for the normal and bending gages , and 0.062" × 0.063" for the shear gages. More information about the strain gages can be found in reference [11] (catalog names are CEA-06-062UV-500, and CEA-06-125UT-350 for the normal/bending gages and the shear gages respectively). The bonding material was M-Bond 200 from the strain gages manufacturer.

The configuration of the strain gages for each channel is shown in figure B.2. The vertical strains in the two cell faces perpendicular to the direction of motion (defined as $\epsilon_a$ and $\epsilon_b$) were measured separately using four identical strain gages in Poisson's configuration. The normal strains and the bending strains were then obtained by averaging and subtracting $\epsilon_a$ and $\epsilon_b$ respectively. The shearing strains were sensed using four 45° oriented strain gages as shown in figure B.6.a.

### Calibration factors and cell sensitivity

The calibration factor and the cell sensitivity calculations for the case of shearing force only will be presented in this section. The computation of these parameters for the axial force and bending moment cases was conducted in a similar fashion.

For the full bridge shown in figure B.6.b, the bridge output $\delta$R can be obtained using the expression;

$$\frac{\delta E}{V} = \frac{S_g}{4} \sum_{i=1}^{4} \epsilon_i$$

where;

V = bridge excitation in volts.

$S_g$ = gage factor.

$\epsilon_i$ = shear strains = $\frac{Q}{E \times A_{web}}$

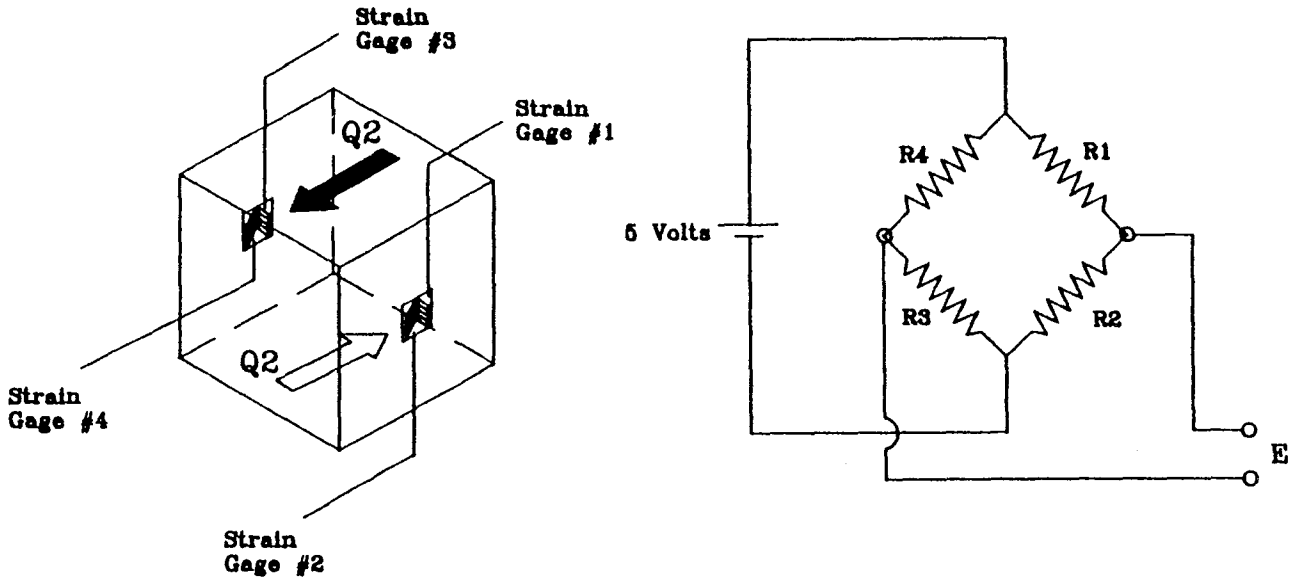


(a) Strain Gages Orientation. (b) Wiring Scheme.

Figure B.6: Shear Cell Strain Gaging and Wiring Scheme.

For an excitation of 5 Volts, a gage factor of 2.06, and an amplification of 1000, the bridge output will be equal to;

$$\delta E = 5 \times 2.06 \times 1000 \times \epsilon$$

$$= 10,300 \times \frac{Q}{2 \times 1.3125 \times 0.0625 \times 29,000} = 2.165\ Q$$

$$Q = 0.462\ \delta E$$

where;

$Q$ = shearing force in kips.

$\delta E$ = bridge output in Volts.

The average measured calibration factor in shear was 0.315, indicating that the calculated factor was about 1.47 times the measured one. This discrepancy arose due to the error in the analytical calculation of strains as opposed to the actual strain distribution measured by the strain gages [4]. Similar discrepancies were also observed in the cases of axial force and flexure.

The load cell sensitivity in shear was controlled by the resolution of the data aquisition card. For the current case, the cell could sense shearing fores as low as 1.54 lbs, which was considered satisfactory for the present purpose.

## B.2 Cell Calibration

Prior to calibration in a certain direction, the load cell was exposed to 30 full range reversible loading cycles in that direction. The calibration tests were then conducted at least twice to check the repeatability of the calibration results.

The load cell was calibrated under axial force by loading it in axial compression using the load set-up shown in figure B.7.a. This also provided a check for the cross-channel interference between axial force and shear and flexure. The same set-up was used for calibration under uniaxial bending at different eccentricities. Calibration under shear was conducted using the load set-up shown in figure B.7.b.

Results of cell #2 calibration tests are provided in figures B.8.a through B.8.d for the cases of axial force, bending moment, shearing force $Q_1$, and shearing force $Q_2$, respectively. It can be seen that the cell indicated very good linearity especially for the cases of flexure and shear. Cross channel interactions are shown in figures B.9.a through B.9.d, where it can be observed that some interaction between flexure and axial force channels was detected. This was also true for the shear and axial force channels. The major sources of these interactions were errors in the alignment of the strain gages and the non-uniformity of the wall thickness of the square section tube. Since these interferences were within a maximum value of 5%, it was decided that the cell response was satisfactory, and no further attempts to improve its performace were made.

## B.3 Cell Installation

The installation scheme of the load cell is illustrated in figure B.10, indicating that the column reinforcing bars were mechanically connected to the steel installation plates using two steel nuts for each bar. The spacing between the installation plates was maintained during construction using dummy load cells with the same dimensions of the actual instrumented cells.

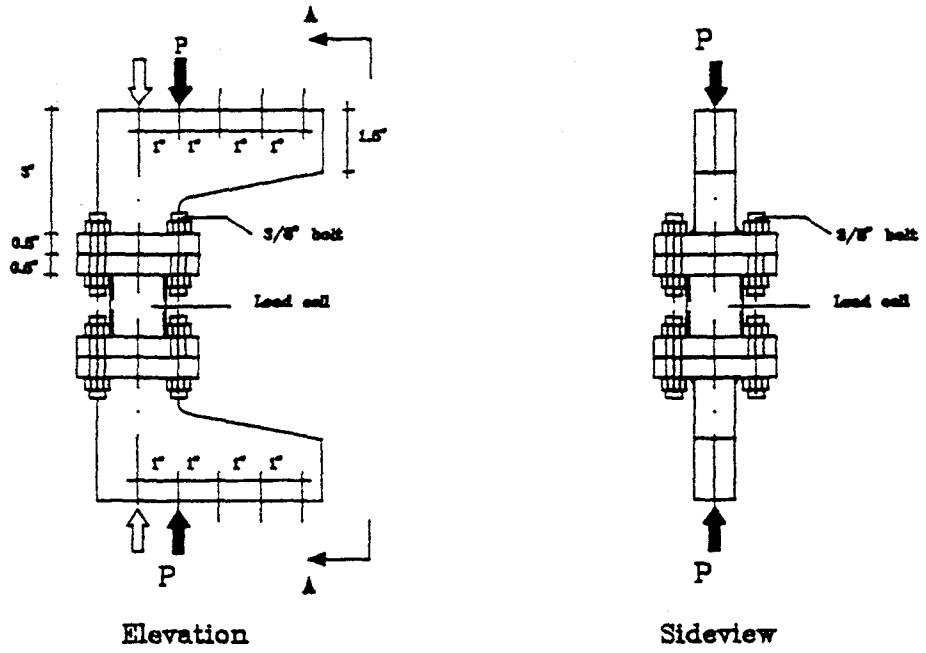


Elevation Sideview

(a) Calibration Under Combined Bending and Normal Force.

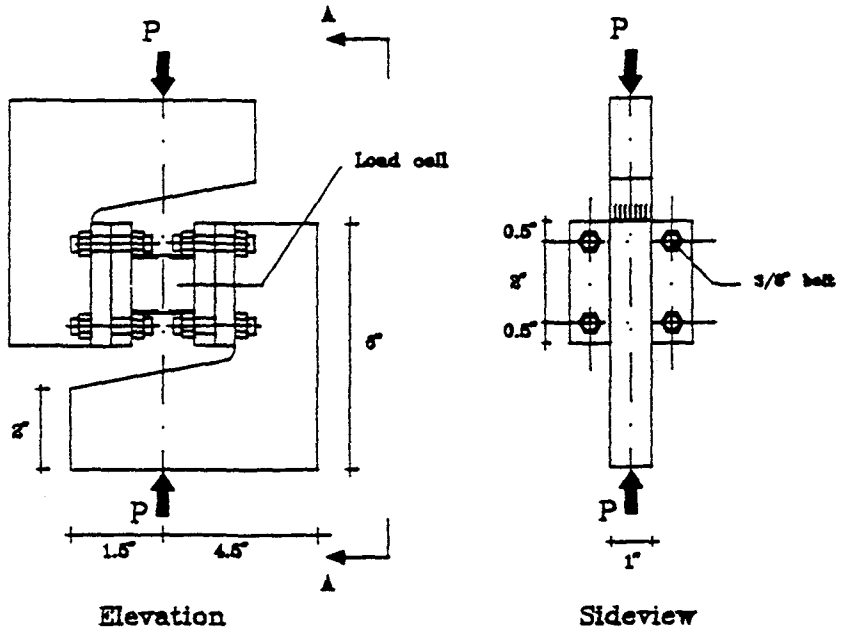


Elevation Sideview

(b) Calibration in Shear.

Figure B.7: Load Set-up for The Load Cell Calibration.

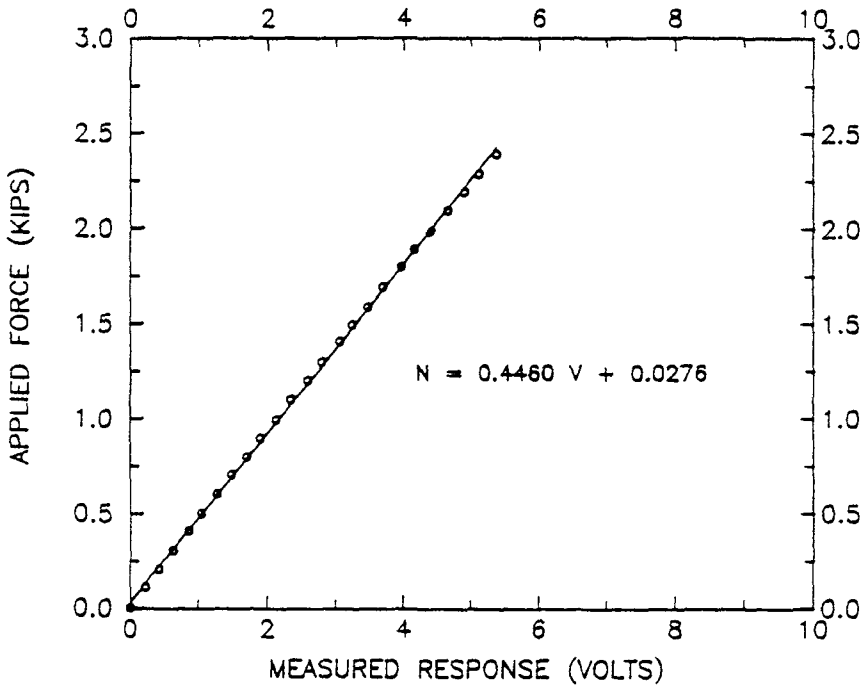


(a) CALIBRATION UNDER AXIAL FORCE FOR CELL #2

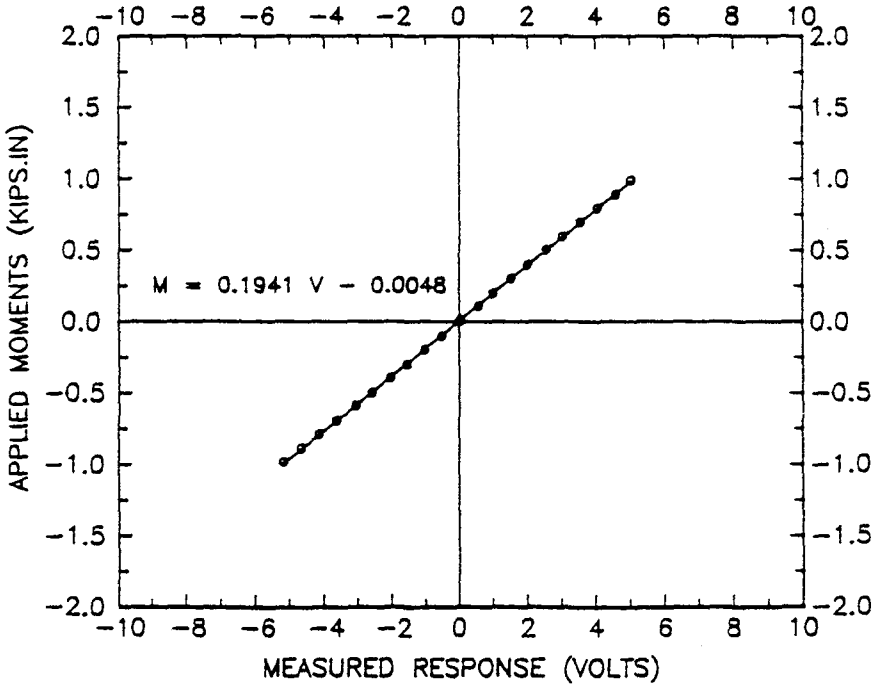


(b) CALIBRATION IN BENDING FOR CELL #2

Figure B.8: Load Cell Calibration.

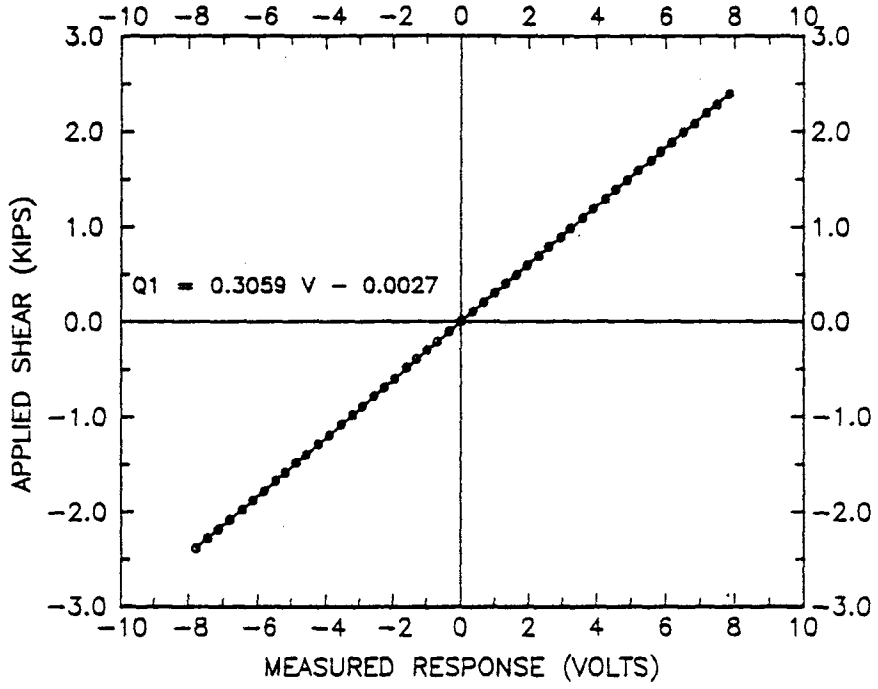


(c) CALIBRATION IN SHEAR Q1 FOR CELL #2

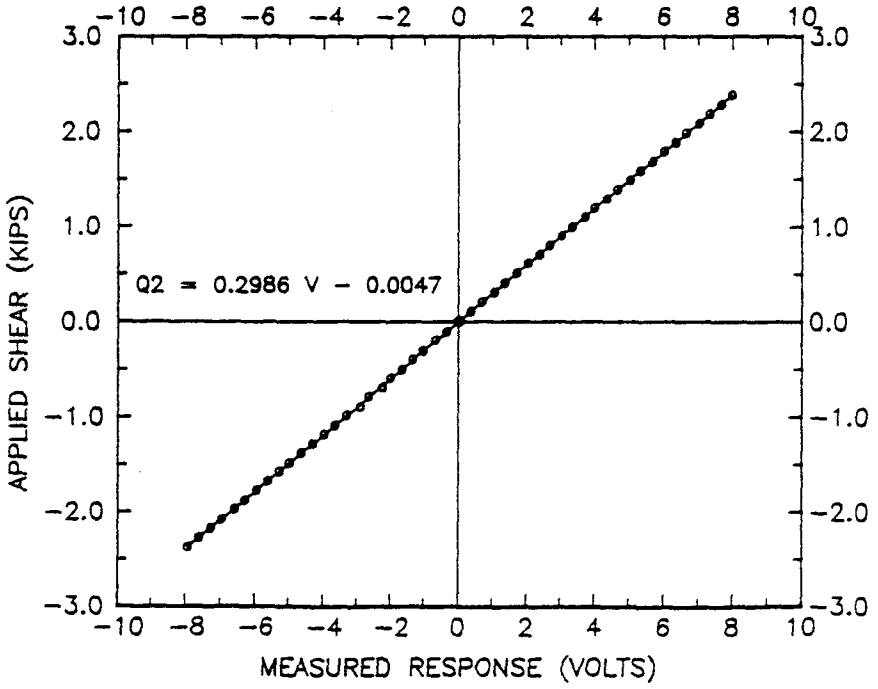


(d) CALIBRATION IN SHEAR Q2 FOR CELL #2

Figure B.8: Load Cell Calibration (Continued).

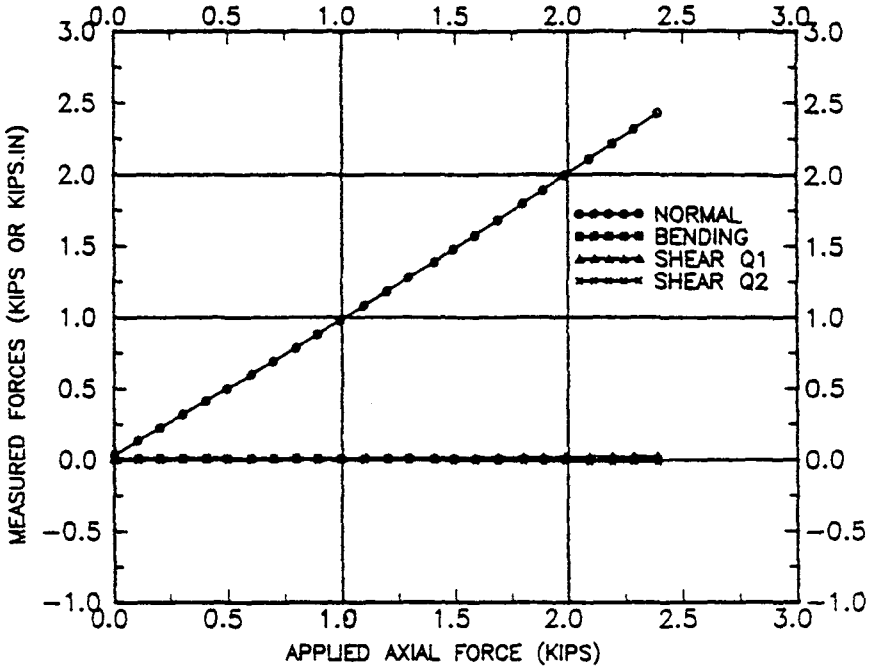


(a) INTERACTION BETWEEN NORMAL FORCE N1 AND M, Q1, AND Q2 FOR LOAD CELL #2

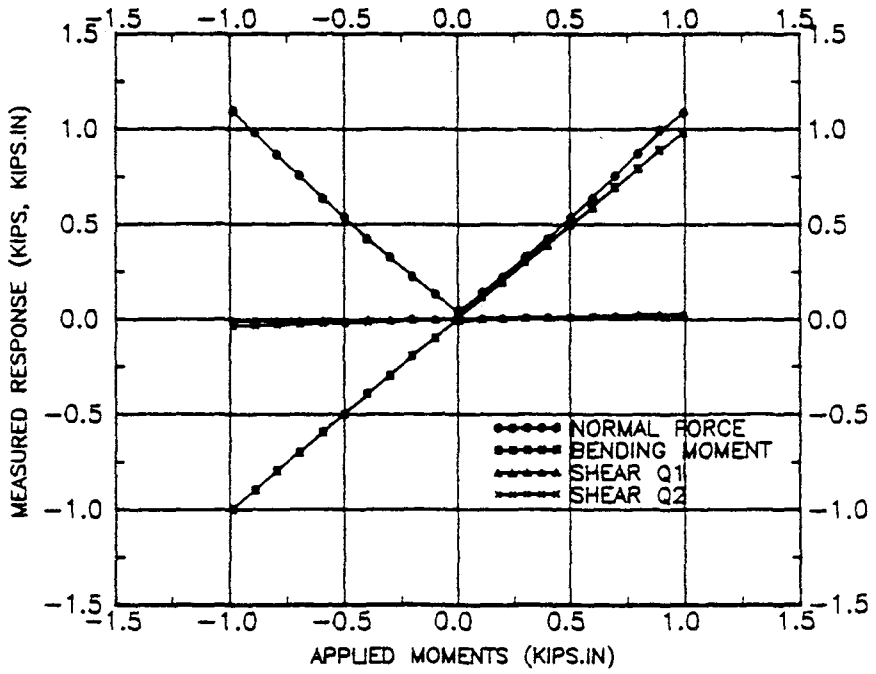


(b) INTERACTION BETWEEN MOMENT M AND N, Q1, AND Q2 FOR CELL #2

Figure B.9: Interaction Between Different Channels.

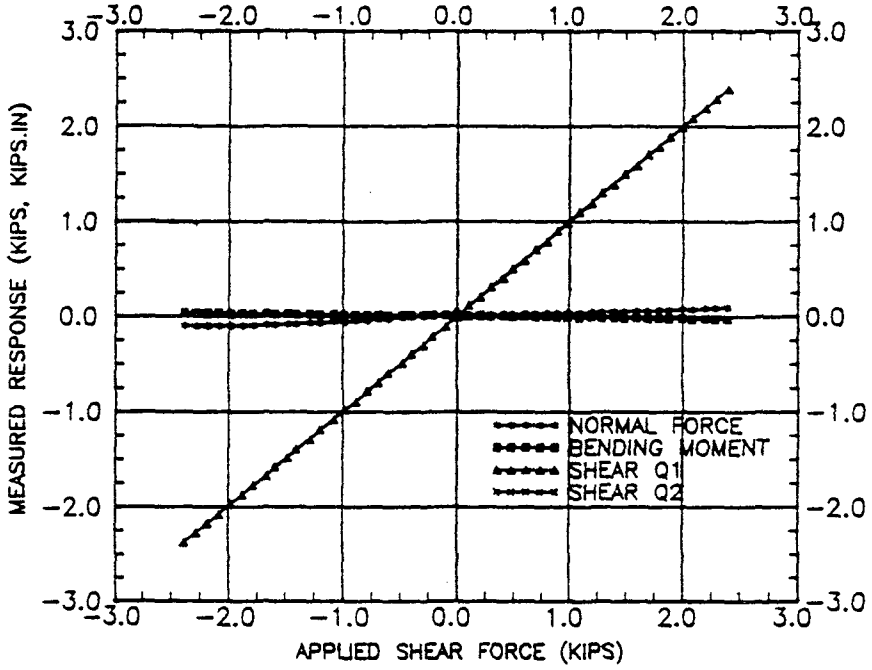


(c) INTERACTION BETWEEN SHEAR Q1 AND N, M, AND Q2 FOR CELL #2

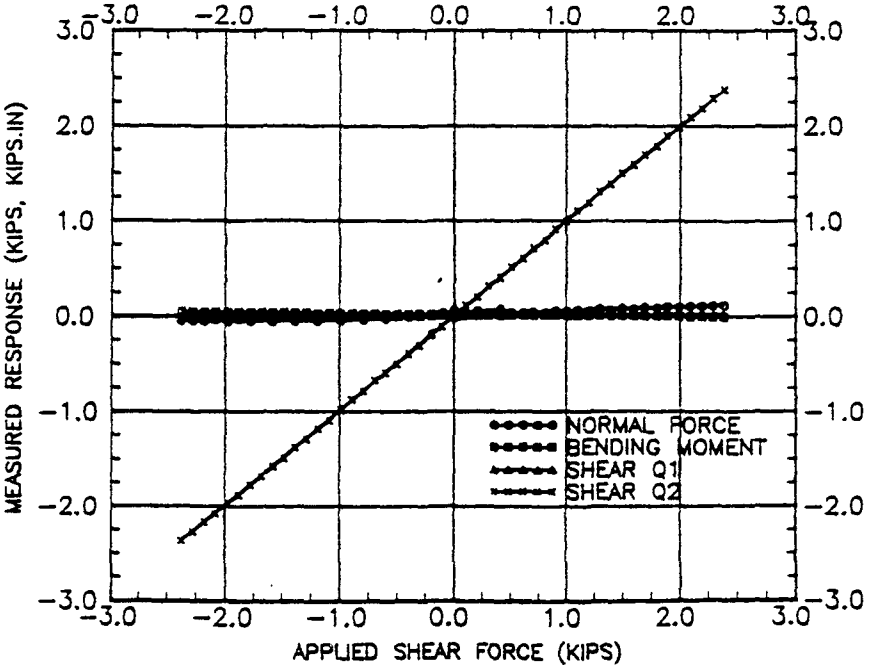


(d) INTERACTION BETWEEN SHEAR Q2 AND N, M, AND Q1 FOR CELL #2

Figure B.9: Interaction Between Different Channels (Continued).

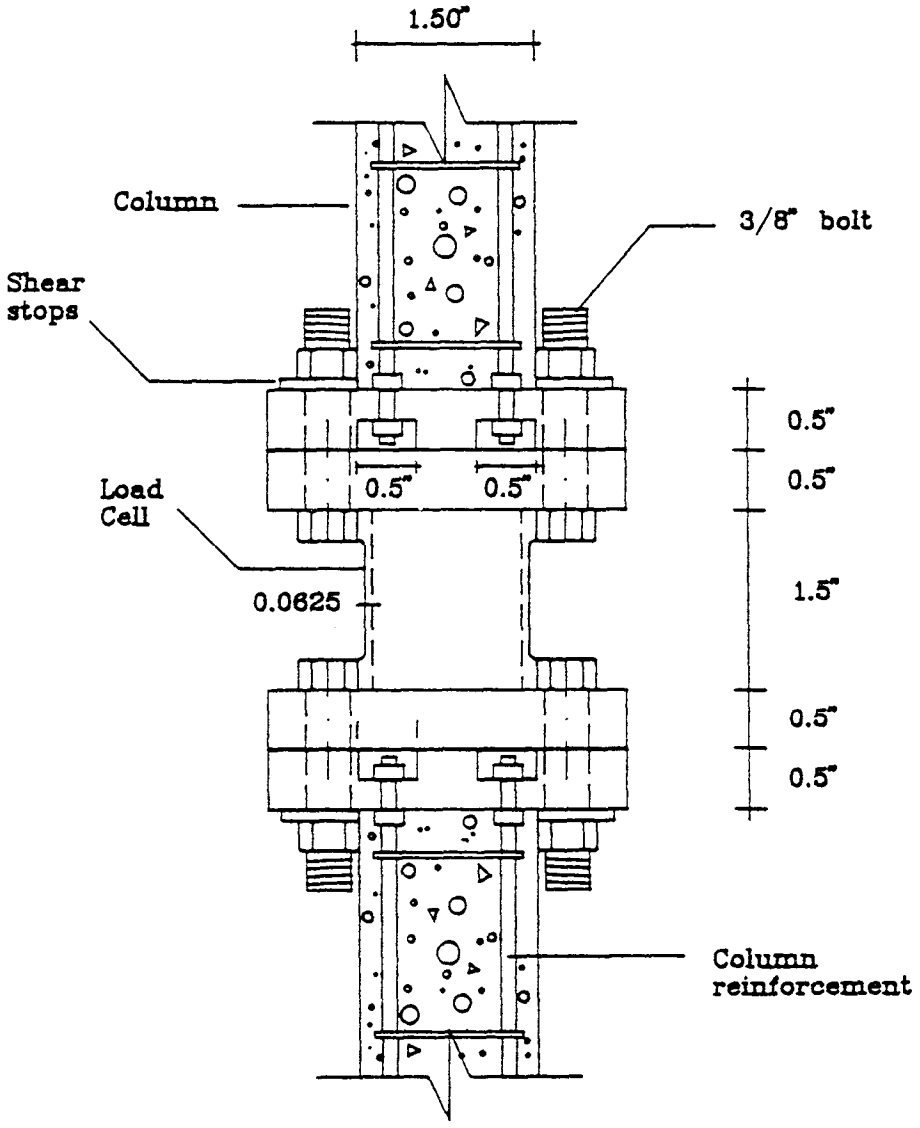


Figure B.10: Load Cell Installation Scheme.

After the model was constructed, the columns were braced and the installation of the load cells was carried out for one column at a time in the following manner. First, the bolts connecting the dummy cell to the installation plates were loosened, then the top plate was raised using a manual jack for a small distance (about .002"). The dummy cell was slid out and at the same time, the instrumented cell was slid in. The load cell was then aligned with the installation plates edges and the top plate was lowered. Four aluminum shear stops were used as washers to bolt the load cell to the installation plates. The spacing between the shear stops and the washers was filled with Hydrostone later. The same process was repeated for all eight columns. Only one frame was instrumented with active load cells. Dummy cells were used for the other frame to maintain symmetry of the model stiffness.

## NATIONAL CENTER FOR EARTHQUAKE ENGINEERING RESEARCH
## LIST OF TECHNICAL REPORTS

The National Center for Earthquake Engineering Research (NCEER) publishes technical reports on a variety of subjects related to earthquake engineering written by authors funded through NCEER. These reports are available from both NCEER's Publications Department and the National Technical Information Service (NTIS). Requests for reports should be directed to the Publications Department, National Center for Earthquake Engineering Research, State University of New York at Buffalo, Red Jacket Quadrangle, Buffalo, New York 14261. Reports can also be requested through NTIS, 5285 Port Royal Road, Springfield, Virginia 22161. NTIS accession numbers are shown in parenthesis, if available.

NCEER-87-0001 "First-Year Program in Research, Education and Technology Transfer," 3/5/87, (PB88-134275/AS).

NCEER-87-0002 "Experimental Evaluation of Instantaneous Optimal Algorithms for Structural Control," by R.C. Lin, T.T. Soong and A.M. Reinhorn, 4/20/87, (PB88-134341/AS).

NCEER-87-0003 "Experimentation Using the Earthquake Simulation Facilities at University at Buffalo," by A.M. Reinhorn and R.L. Ketter, to be published.

NCEER-87-0004 "The System Characteristics and Performance of a Shaking Table," by J.S. Hwang, K.C. Chang and G.C. Lee, 6/1/87, (PB88-134259/AS). This report is available only through NTIS (see address given above).

NCEER-87-0005 "A Finite Element Formulation for Nonlinear Viscoplastic Material Using a Q Model," by O. Gyebi and G. Dasgupta, 11/2/87, (PB88-213764/AS).

NCEER-87-0006 "Symbolic Manipulation Program (SMP) - Algebraic Codes for Two and Three Dimensional Finite Element Formulations," by X. Lee and G. Dasgupta, 11/9/87, (PB88-219522/AS).

NCEER-87-0007 "Instantaneous Optimal Control Laws for Tall Buildings Under Seismic Excitations," by J.N. Yang, A. Akbarpour and P. Ghaemmaghami, 6/10/87, (PB88-134333/AS).

NCEER-87-0008 "IDARC: Inelastic Damage Analysis of Reinforced Concrete Frame - Shear-Wall Structures," by Y.J. Park, A.M. Reinhorn and S.K. Kunnath, 7/20/87, (PB88-134325/AS).

NCEER-87-0009 "Liquefaction Potential for New York State: A Preliminary Report on Sites in Manhattan and Buffalo," by M. Budhu, V. Vijayakumar, R.F. Giese and L. Baumgras, 8/31/87, (PB88-163704/AS). This report is available only through NTIS (see address given above).

NCEER-87-0010 "Vertical and Torsional Vibration of Foundations in Inhomogeneous Media," by A.S. Veletsos and K.W. Dotson, 6/1/87, (PB88-134291/AS).

NCEER-87-0011 "Seismic Probabilistic Risk Assessment and Seismic Margins Studies for Nuclear Power Plants," by Howard H.M. Hwang, 6/15/87, (PB88-134267/AS).

NCEER-87-0012 "Parametric Studies of Frequency Response of Secondary Systems Under Ground-Acceleration Excitations," by Y. Yong and Y.K. Lin, 6/10/87, (PB88-134309/AS).

NCEER-87-0013 "Frequency Response of Secondary Systems Under Seismic Excitation," by J.A. HoLung, J. Cai and Y.K. Lin, 7/31/87, (PB88-134317/AS).

NCEER-87-0014 "Modelling Earthquake Ground Motions in Seismically Active Regions Using Parametric Time Series Methods," by G.W. Ellis and A.S. Cakmak, 8/25/87, (PB88-134283/AS).

NCEER-87-0015 "Detection and Assessment of Seismic Structural Damage," by E. DiPasquale and A.S. Cakmak, 8/25/87, (PB88-163712/AS).

NCEER-87-0016 "Pipeline Experiment at Parkfield, California," by J. Isenberg and E. Richardson, 9/15/87, (PB88-163720/AS). This report is available only through NTIS (see address given above).

NCEER-87-0017 "Digital Simulation of Seismic Ground Motion," by M. Shinozuka, G. Deodatis and T. Harada, 8/31/87, (PB88-155197/AS). This report is available only through NTIS (see address given above).

NCEER-87-0018 "Practical Considerations for Structural Control: System Uncertainty, System Time Delay and Truncation of Small Control Forces," J.N. Yang and A. Akbarpour, 8/10/87, (PB88-163738/AS).

NCEER-87-0019 "Modal Analysis of Nonclassically Damped Structural Systems Using Canonical Transformation," by J.N. Yang, S. Sarkani and F.X. Long, 9/27/87, (PB88-187851/AS).

NCEER-87-0020 "A Nonstationary Solution in Random Vibration Theory," by J.R. Red-Horse and P.D. Spanos, 11/3/87, (PB88-163746/AS).

NCEER-87-0021 "Horizontal Impedances for Radially Inhomogeneous Viscoelastic Soil Layers," by A.S. Veletsos and K.W. Dotson, 10/15/87, (PB88-150859/AS).

NCEER-87-0022 "Seismic Damage Assessment of Reinforced Concrete Members," by Y.S. Chung, C. Meyer and M. Shinozuka, 10/9/87, (PB88-150867/AS). This report is available only through NTIS (see address given above).

NCEER-87-0023 "Active Structural Control in Civil Engineering," by T.T. Soong, 11/11/87, (PB88-187778/AS).

NCEER-87-0024 "Vertical and Torsional Impedances for Radially Inhomogeneous Viscoelastic Soil Layers," by K.W. Dotson and A.S. Veletsos, 12/87, (PB88-187786/AS).

NCEER-87-0025 "Proceedings from the Symposium on Seismic Hazards, Ground Motions, Soil-Liquefaction and Engineering Practice in Eastern North America," October 20-22, 1987, edited by K.H. Jacob, 12/87, (PB88-188115/AS).

NCEER-87-0026 "Report on the Whittier-Narrows, California, Earthquake of October 1, 1987," by J. Pantelic and A. Reinhorn, 11/87, (PB88-187752/AS). This report is available only through NTIS (see address given above).

NCEER-87-0027 "Design of a Modular Program for Transient Nonlinear Analysis of Large 3-D Building Structures," by S. Srivastav and J.F. Abel, 12/30/87, (PB88-187950/AS).

NCEER-87-0028 "Second-Year Program in Research, Education and Technology Transfer," 3/8/88, (PB88-219480/AS).

NCEER-88-0001 "Workshop on Seismic Computer Analysis and Design of Buildings With Interactive Graphics," by W. McGuire, J.F. Abel and C.H. Conley, 1/18/88, (PB88-187760/AS).

NCEER-88-0002 "Optimal Control of Nonlinear Flexible Structures," by J.N. Yang, F.X. Long and D. Wong, 1/22/88, (PB88-213772/AS).

NCEER-88-0003 "Substructuring Techniques in the Time Domain for Primary-Secondary Structural Systems," by G.D. Manolis and G. Juhn, 2/10/88, (PB88-213780/AS).

NCEER-88-0004 "Iterative Seismic Analysis of Primary-Secondary Systems," by A. Singhal, L.D. Lutes and P.D. Spanos, 2/23/88, (PB88-213798/AS).

NCEER-88-0005 "Stochastic Finite Element Expansion for Random Media," by P.D. Spanos and R. Ghanem, 3/14/88, (PB88-213806/AS).

NCEER-88-0006 "Combining Structural Optimization and Structural Control," by F.Y. Cheng and C.P. Pantelides, 1/10/88, (PB88-213814/AS).

NCEER-88-0007 "Seismic Performance Assessment of Code-Designed Structures," by H.H-M. Hwang, J-W. Jaw and H-J. Shau, 3/20/88, (PB88-219423/AS).

NCEER-88-0008 "Reliability Analysis of Code-Designed Structures Under Natural Hazards," by H.H-M. Hwang, H. Ushiba and M. Shinozuka, 2/29/88, (PB88-229471/AS).

NCEER-88-0009 "Seismic Fragility Analysis of Shear Wall Structures," by J-W Jaw and H.H-M. Hwang, 4/30/88, (PB89-102867/AS).

NCEER-88-0010 "Base Isolation of a Multi-Story Building Under a Harmonic Ground Motion - A Comparison of Performances of Various Systems," by F-G Fan, G. Ahmadi and I.G. Tadjbakhsh, 5/18/88, (PB89-122238/AS).

NCEER-88-0011 "Seismic Floor Response Spectra for a Combined System by Green's Functions," by F.M. Lavelle, L.A. Bergman and P.D. Spanos, 5/1/88, (PB89-102875/AS).

NCEER-88-0012 "A New Solution Technique for Randomly Excited Hysteretic Structures," by G.Q. Cai and Y.K. Lin, 5/16/88, (PB89-102883/AS).

NCEER-88-0013 "A Study of Radiation Damping and Soil-Structure Interaction Effects in the Centrifuge," by K. Weissman, supervised by J.H. Prevost, 5/24/88, (PB89-144703/AS).

NCEER-88-0014 "Parameter Identification and Implementation of a Kinematic Plasticity Model for Frictional Soils," by J.H. Prevost and D.V. Griffiths, to be published.

NCEER-88-0015 "Two- and Three- Dimensional Dynamic Finite Element Analyses of the Long Valley Dam," by D.V. Griffiths and J.H. Prevost, 6/17/88, (PB89-144711/AS).

NCEER-88-0016 "Damage Assessment of Reinforced Concrete Structures in Eastern United States," by A.M. Reinhorn, M.J. Seidel, S.K. Kunnath and Y.J. Park, 6/15/88, (PB89-122220/AS).

NCEER-88-0017 "Dynamic Compliance of Vertically Loaded Strip Foundations in Multilayered Viscoelastic Soils," by S. Ahmad and A.S.M. Israil, 6/17/88, (PB89-102891/AS).

NCEER-88-0018 "An Experimental Study of Seismic Structural Response With Added Viscoelastic Dampers," by R.C. Lin, Z. Liang, T.T. Soong and R.H. Zhang, 6/30/88, (PB89-122212/AS). This report is available only through NTIS (see address given above).

NCEER-88-0019 "Experimental Investigation of Primary - Secondary System Interaction," by G.D. Manolis, G. Juhn and A.M. Reinhorn, 5/27/88, (PB89-122204/AS).

NCEER-88-0020 "A Response Spectrum Approach For Analysis of Nonclassically Damped Structures," by J.N. Yang, S. Sarkani and F.X. Long, 4/22/88, (PB89-102909/AS).

NCEER-88-0021 "Seismic Interaction of Structures and Soils: Stochastic Approach," by A.S. Veletsos and A.M. Prasad, 7/21/88, (PB89-122196/AS).

NCEER-88-0022 "Identification of the Serviceability Limit State and Detection of Seismic Structural Damage," by E. DiPasquale and A.S. Cakmak, 6/15/88, (PB89-122188/AS). This report is available only through NTIS (see address given above).

NCEER-88-0023 "Multi-Hazard Risk Analysis: Case of a Simple Offshore Structure," by B.K. Bhartia and E.H. Vanmarcke, 7/21/88, (PB89-145213/AS).

NCEER-88-0024 "Automated Seismic Design of Reinforced Concrete Buildings," by Y.S. Chung, C. Meyer and M. Shinozuka, 7/5/88, (PB89-122170/AS). This report is available only through NTIS (see address given above).

NCEER-88-0025 "Experimental Study of Active Control of MDOF Structures Under Seismic Excitations," by L.L. Chung, R.C. Lin, T.T. Soong and A.M. Reinhorn, 7/10/88, (PB89-122600/AS).

NCEER-88-0026 "Earthquake Simulation Tests of a Low-Rise Metal Structure," by J.S. Hwang, K.C. Chang, G.C. Lee and R.L. Ketter, 8/1/88, (PB89-102917/AS).

NCEER-88-0027 "Systems Study of Urban Response and Reconstruction Due to Catastrophic Earthquakes," by F. Kozin and H.K. Zhou, 9/22/88, (PB90-162348/AS).

NCEER-88-0028 "Seismic Fragility Analysis of Plane Frame Structures," by H.H-M. Hwang and Y.K. Low, 7/31/88, (PB89-131445/AS).

NCEER-88-0029 "Response Analysis of Stochastic Structures," by A. Kardara, C. Bucher and M. Shinozuka, 9/22/88, (PB89-174429/AS).

NCEER-88-0030 "Nonnormal Accelerations Due to Yielding in a Primary Structure," by D.C.K. Chen and L.D. Lutes, 9/19/88, (PB89-131437/AS).

NCEER-88-0031 "Design Approaches for Soil-Structure Interaction," by A.S. Veletsos, A.M. Prasad and Y. Tang, 12/30/88, (PB89-174437/AS). This report is available only through NTIS (see address given above).

NCEER-88-0032 "A Re-evaluation of Design Spectra for Seismic Damage Control," by C.J. Turkstra and A.G. Tallin, 11/7/88, (PB89-145221/AS).

NCEER-88-0033 "The Behavior and Design of Noncontact Lap Splices Subjected to Repeated Inelastic Tensile Loading," by V.E. Sagan, P. Gergely and R.N. White, 12/8/88, (PB89-163737/AS).

NCEER-88-0034 "Seismic Response of Pile Foundations," by S.M. Mamoon, P.K. Banerjee and S. Ahmad, 11/1/88, (PB89-145239/AS).

NCEER-88-0035 "Modeling of R/C Building Structures With Flexible Floor Diaphragms (IDARC2)," by A.M. Reinhorn, S.K. Kunnath and N. Panahshahi, 9/7/88, (PB89-207153/AS).

NCEER-88-0036 "Solution of the Dam-Reservoir Interaction Problem Using a Combination of FEM, BEM with Particular Integrals, Modal Analysis, and Substructuring," by C-S. Tsai, G.C. Lee and R.L. Ketter, 12/31/88, (PB89-207146/AS).

NCEER-88-0037 "Optimal Placement of Actuators for Structural Control," by F.Y. Cheng and C.P. Pantelides, 8/15/88, (PB89-162846/AS).

NCEER-88-0038 "Teflon Bearings in Aseismic Base Isolation: Experimental Studies and Mathematical Modeling," by A. Mokha, M.C. Constantinou and A.M. Reinhorn, 12/5/88, (PB89-218457/AS). This report is available only through NTIS (see address given above).

NCEER-88-0039 "Seismic Behavior of Flat Slab High-Rise Buildings in the New York City Area," by P. Weidlinger and M. Ettouney, 10/15/88, (PB90-145681/AS).

NCEER-88-0040 "Evaluation of the Earthquake Resistance of Existing Buildings in New York City," by P. Weidlinger and M. Ettouney, 10/15/88, to be published.

NCEER-88-0041 "Small-Scale Modeling Techniques for Reinforced Concrete Structures Subjected to Seismic Loads," by W. Kim, A. El-Attar and R.N. White, 11/22/88, (PB89-189625/AS).

NCEER-88-0042 "Modeling Strong Ground Motion from Multiple Event Earthquakes," by G.W. Ellis and A.S. Cakmak, 10/15/88, (PB89-174445/AS).

NCEER-88-0043 "Nonstationary Models of Seismic Ground Acceleration," by M. Grigoriu, S.E. Ruiz and E. Rosenblueth, 7/15/88, (PB89-189617/AS).

NCEER-88-0044 "SARCF User's Guide: Seismic Analysis of Reinforced Concrete Frames," by Y.S. Chung, C. Meyer and M. Shinozuka, 11/9/88, (PB89-174452/AS).

NCEER-88-0045 "First Expert Panel Meeting on Disaster Research and Planning," edited by J. Pantelic and J. Stoyle, 9/15/88, (PB89-174460/AS).

NCEER-88-0046 "Preliminary Studies of the Effect of Degrading Infill Walls on the Nonlinear Seismic Response of Steel Frames," by C.Z. Chrysostomou, P. Gergely and J.F. Abel, 12/19/88, (PB89-208383/AS).

NCEER-88-0047 "Reinforced Concrete Frame Component Testing Facility - Design, Construction, Instrumentation and Operation," by S.P. Pessiki, C. Conley, T. Bond, P. Gergely and R.N. White, 12/16/88, (PB89-174478/AS).

NCEER-89-0001 "Effects of Protective Cushion and Soil Compliancy on the Response of Equipment Within a Seismically Excited Building," by J.A. HoLung, 2/16/89, (PB89-207179/AS).

NCEER-89-0002 "Statistical Evaluation of Response Modification Factors for Reinforced Concrete Structures," by H.H-M. Hwang and J-W. Jaw, 2/17/89, (PB89-207187/AS).

NCEER-89-0003 "Hysteretic Columns Under Random Excitation," by G-Q. Cai and Y.K. Lin, 1/9/89, (PB89-196513/AS).

NCEER-89-0004 "Experimental Study of 'Elephant Foot Bulge' Instability of Thin-Walled Metal Tanks," by Z-H. Jia and R.L. Ketter, 2/22/89, (PB89-207195/AS).

NCEER-89-0005 "Experiment on Performance of Buried Pipelines Across San Andreas Fault," by J. Isenberg, E. Richardson and T.D. O'Rourke, 3/10/89, (PB89-218440/AS).

NCEER-89-0006 "A Knowledge-Based Approach to Structural Design of Earthquake-Resistant Buildings," by M. Subramani, P. Gergely, C.H. Conley, J.F. Abel and A.H. Zaghw, 1/15/89, (PB89-218465/AS).

NCEER-89-0007 "Liquefaction Hazards and Their Effects on Buried Pipelines," by T.D. O'Rourke and P.A. Lane, 2/1/89, (PB89-218481).

NCEER-89-0008 "Fundamentals of System Identification in Structural Dynamics," by H. Imai, C-B. Yun, O. Maruyama and M. Shinozuka, 1/26/89, (PB89-207211/AS).

NCEER-89-0009 "Effects of the 1985 Michoacan Earthquake on Water Systems and Other Buried Lifelines in Mexico," by A.G. Ayala and M.J. O'Rourke, 3/8/89, (PB89-207229/AS).

NCEER-89-R010 "NCEER Bibliography of Earthquake Education Materials," by K.E.K. Ross, Second Revision, 9/1/89, (PB90-125352/AS).

NCEER-89-0011 "Inelastic Three-Dimensional Response Analysis of Reinforced Concrete Building Structures (IDARC-3D), Part I - Modeling," by S.K. Kunnath and A.M. Reinhorn, 4/17/89, (PB90-114612/AS).

NCEER-89-0012 "Recommended Modifications to ATC-14," by C.D. Poland and J.O. Malley, 4/12/89, (PB90-108648/AS).

NCEER-89-0013 "Repair and Strengthening of Beam-to-Column Connections Subjected to Earthquake Loading," by M. Corazao and A.J. Durrani, 2/28/89, (PB90-109885/AS).

NCEER-89-0014 "Program EXKAL2 for Identification of Structural Dynamic Systems," by O. Maruyama, C-B. Yun, M. Hoshiya and M. Shinozuka, 5/19/89, (PB90-109877/AS).

NCEER-89-0015 "Response of Frames With Bolted Semi-Rigid Connections, Part I - Experimental Study and Analytical Predictions," by P.J. DiCorso, A.M. Reinhorn, J.R. Dickerson, J.B. Radziminski and W.L. Harper, 6/1/89, to be published.

NCEER-89-0016 "ARMA Monte Carlo Simulation in Probabilistic Structural Analysis," by P.D. Spanos and M.P. Mignolet, 7/10/89, (PB90-109893/AS).

NCEER-89-P017 "Preliminary Proceedings from the Conference on Disaster Preparedness - The Place of Earthquake Education in Our Schools," Edited by K.E.K. Ross, 6/23/89.

NCEER-89-0017 "Proceedings from the Conference on Disaster Preparedness - The Place of Earthquake Education in Our Schools," Edited by K.E.K. Ross, 12/31/89, (PB90-207895). This report is available only through NTIS (see address given above).

NCEER-89-0018 "Multidimensional Models of Hysteretic Material Behavior for Vibration Analysis of Shape Memory Energy Absorbing Devices, by E.J. Graesser and F.A. Cozzarelli, 6/7/89, (PB90-164146/AS).

NCEER-89-0019 "Nonlinear Dynamic Analysis of Three-Dimensional Base Isolated Structures (3D-BASIS)," by S. Nagarajaiah, A.M. Reinhorn and M.C. Constantinou, 8/3/89, (PB90-161936/AS). This report is available only through NTIS (see address given above).

NCEER-89-0020 "Structural Control Considering Time-Rate of Control Forces and Control Rate Constraints," by F.Y. Cheng and C.P. Pantelides, 8/3/89, (PB90-120445/AS).

NCEER-89-0021 "Subsurface Conditions of Memphis and Shelby County," by K.W. Ng, T-S. Chang and H-H.M. Hwang, 7/26/89, (PB90-120437/AS).

NCEER-89-0022 "Seismic Wave Propagation Effects on Straight Jointed Buried Pipelines," by K. Elhmadi and M.J. O'Rourke, 8/24/89, (PB90-162322/AS).

NCEER-89-0023 "Workshop on Serviceability Analysis of Water Delivery Systems," edited by M. Grigoriu, 3/6/89, (PB90-127424/AS).

NCEER-89-0024 "Shaking Table Study of a 1/5 Scale Steel Frame Composed of Tapered Members," by K.C. Chang, J.S. Hwang and G.C. Lee, 9/18/89, (PB90-160169/AS).

NCEER-89-0025 "DYNA1D: A Computer Program for Nonlinear Seismic Site Response Analysis - Technical Documentation," by Jean H. Prevost, 9/14/89, (PB90-161944/AS). This report is available only through NTIS (see address given above).

NCEER-89-0026 "1:4 Scale Model Studies of Active Tendon Systems and Active Mass Dampers for Aseismic Protection," by A.M. Reinhorn, T.T. Soong, R.C. Lin, Y.P. Yang, Y. Fukao, H. Abe and M. Nakai, 9/15/89, (PB90-173246/AS).

NCEER-89-0027 "Scattering of Waves by Inclusions in a Nonhomogeneous Elastic Half Space Solved by Boundary Element Methods," by P.K. Hadley, A. Askar and A.S. Cakmak, 6/15/89, (PB90-145699/AS).

NCEER-89-0028 "Statistical Evaluation of Deflection Amplification Factors for Reinforced Concrete Structures," by H.H.M. Hwang, J-W. Jaw and A.L. Ch'ng, 8/31/89, (PB90-164633/AS).

NCEER-89-0029 "Bedrock Accelerations in Memphis Area Due to Large New Madrid Earthquakes," by H.H.M. Hwang, C.H.S. Chen and G. Yu, 11/7/89, (PB90-162330/AS).

NCEER-89-0030 "Seismic Behavior and Response Sensitivity of Secondary Structural Systems," by Y.Q. Chen and T.T. Soong, 10/23/89, (PB90-164658/AS).

NCEER-89-0031 "Random Vibration and Reliability Analysis of Primary-Secondary Structural Systems," by Y. Ibrahim, M. Grigoriu and T.T. Soong, 11/10/89, (PB90-161951/AS).

NCEER-89-0032 "Proceedings from the Second U.S. - Japan Workshop on Liquefaction, Large Ground Deformation and Their Effects on Lifelines, September 26-29, 1989," Edited by T.D. O'Rourke and M. Hamada, 12/1/89, (PB90-209388/AS).

NCEER-89-0033 "Deterministic Model for Seismic Damage Evaluation of Reinforced Concrete Structures," by J.M. Bracci, A.M. Reinhorn, J.B. Mander and S.K. Kunnath, 9/27/89.

NCEER-89-0034 "On the Relation Between Local and Global Damage Indices," by E. DiPasquale and A.S. Cakmak, 8/15/89, (PB90-173865).

NCEER-89-0035 "Cyclic Undrained Behavior of Nonplastic and Low Plasticity Silts," by A.J. Walker and H.E. Stewart, 7/26/89, (PB90-183518/AS).

NCEER-89-0036 "Liquefaction Potential of Surficial Deposits in the City of Buffalo, New York," by M. Budhu, R. Giese and L. Baumgrass, 1/17/89, (PB90-208455/AS).

NCEER-89-0037 "A Determinstic Assessment of Effects of Ground Motion Incoherence," by A.S. Veletsos and Y. Tang, 7/15/89, (PB90-164294/AS).

NCEER-89-0038 "Workshop on Ground Motion Parameters for Seismic Hazard Mapping," July 17-18, 1989, edited by R.V. Whitman, 12/1/89, (PB90-173923/AS).

NCEER-89-0039 "Seismic Effects on Elevated Transit Lines of the New York City Transit Authority," by C.J. Costantino, C.A. Miller and E. Heymsfield, 12/26/89, (PB90-207887/AS).

NCEER-89-0040 "Centrifugal Modeling of Dynamic Soil-Structure Interaction," by K. Weissman, Supervised by J.H. Prevost, 5/10/89, (PB90-207879/AS).

NCEER-89-0041 "Linearized Identification of Buildings With Cores for Seismic Vulnerability Assessment," by I-K. Ho and A.E. Aktan, 11/1/89, (PB90-251943/AS).

NCEER-90-0001 "Geotechnical and Lifeline Aspects of the October 17, 1989 Loma Prieta Earthquake in San Francisco," by T.D. O'Rourke, H.E. Stewart, F.T. Blackburn and T.S. Dickerman, 1/90, (PB90-208596/AS).

NCEER-90-0002 "Nonnormal Secondary Response Due to Yielding in a Primary Structure," by D.C.K. Chen and L.D. Lutes, 2/28/90, (PB90-251976/AS).

NCEER-90-0003 "Earthquake Education Materials for Grades K-12," by K.E.K. Ross, 4/16/90, (PB91-113415/AS).

NCEER-90-0004 "Catalog of Strong Motion Stations in Eastern North America," by R.W. Busby, 4/3/90, (PB90-251984)/AS.

NCEER-90-0005 "NCEER Strong-Motion Data Base: A User Manuel for the GeoBase Release (Version 1.0 for the Sun3)," by P. Friberg and K. Jacob, 3/31/90 (PB90-258062/AS).

NCEER-90-0006 "Seismic Hazard Along a Crude Oil Pipeline in the Event of an 1811-1812 Type New Madrid Earthquake," by H.H.M. Hwang and C-H.S. Chen, 4/16/90(PB90-258054).

NCEER-90-0007 "Site-Specific Response Spectra for Memphis Sheahan Pumping Station," by H.H.M. Hwang and C.S. Lee, 5/15/90, (PB91-108811/AS).

NCEER-90-0008 "Pilot Study on Seismic Vulnerability of Crude Oil Transmission Systems," by T. Ariman, R. Dobry, M. Grigoriu, F. Kozin, M. O'Rourke, T. O'Rourke and M. Shinozuka, 5/25/90, (PB91-108837/AS).

NCEER-90-0009 "A Program to Generate Site Dependent Time Histories: EQGEN," by G.W. Ellis, M. Srinivasan and A.S. Cakmak, 1/30/90, (PB91-108829/AS).

NCEER-90-0010 "Active Isolation for Seismic Protection of Operating Rooms," by M.E. Talbott, Supervised by M. Shinozuka, 6/8/9, (PB91-110205/AS).

NCEER-90-0011 "Program LINEARID for Identification of Linear Structural Dynamic Systems," by C-B. Yun and M. Shinozuka, 6/25/90, (PB91-110312/AS).

NCEER-90-0012 "Two-Dimensional Two-Phase Elasto-Plastic Seismic Response of Earth Dams," by A.N. Yiagos, Supervised by J.H. Prevost, 6/20/90, (PB91-110197/AS).

NCEER-90-0013 "Secondary Systems in Base-Isolated Structures: Experimental Investigation, Stochastic Response and Stochastic Sensitivity," by G.D. Manolis, G. Juhn, M.C. Constantinou and A.M. Reinhorn, 7/1/90, (PB91-110320/AS).

NCEER-90-0014 "Seismic Behavior of Lightly-Reinforced Concrete Column and Beam-Column Joint Details," by S.P. Pessiki, C.H. Conley, P. Gergely and R.N. White, 8/22/90, (PB91-108795/AS).

NCEER-90-0015 "Two Hybrid Control Systems for Building Structures Under Strong Earthquakes," by J.N. Yang and A. Danielians, 6/29/90, (PB91-125393/AS).

NCEER-90-0016 "Instantaneous Optimal Control with Acceleration and Velocity Feedback," by J.N. Yang and Z. Li, 6/29/90, (PB91-125401/AS).

NCEER-90-0017 "Reconnaissance Report on the Northern Iran Earthquake of June 21, 1990," by M. Mehrain, 10/4/90, (PB91-125377/AS).

NCEER-90-0018 "Evaluation of Liquefaction Potential in Memphis and Shelby County," by T.S. Chang, P.S. Tang, C.S. Lee and H. Hwang, 8/10/90, (PB91-125427/AS).

NCEER-90-0019 "Experimental and Analytical Study of a Combined Sliding Disc Bearing and Helical Steel Spring Isolation System," by M.C. Constantinou, A.S. Mokha and A.M. Reinhorn, 10/4/90, (PB91-125385/AS).

NCEER-90-0020 "Experimental Study and Analytical Prediction of Earthquake Response of a Sliding Isolation System with a Spherical Surface," by A.S. Mokha, M.C. Constantinou and A.M. Reinhorn, 10/11/90, (PB91-125419/AS).

NCEER-90-0021 "Dynamic Interaction Factors for Floating Pile Groups," by G. Gazetas, K. Fan, A. Kaynia and E. Kausel, 9/10/90, (PB91-170381/AS).

NCEER-90-0022 "Evaluation of Seismic Damage Indices for Reinforced Concrete Structures," by S. Rodriguez-Gomez and A.S. Cakmak, 9/30/90, PB91-171322/AS).

NCEER-90-0023 "Study of Site Response at a Selected Memphis Site," by H. Desai, S. Ahmad, E.S. Gazetas and M.R. Oh, 10/11/90, (PB91-196857/AS).

NCEER-90-0024 "A User's Guide to Strongmo: Version 1.0 of NCEER's Strong-Motion Data Access Tool for PCs and Terminals," by P.A. Friberg and C.A.T. Susch, 11/15/90, (PB91-171272/AS).

NCEER-90-0025 "A Three-Dimensional Analytical Study of Spatial Variability of Seismic Ground Motions," by L-L. Hong and A.H.-S. Ang, 10/30/90, (PB91-170399/AS).

NCEER-90-0026 "MUMOID User's Guide - A Program for the Identification of Modal Parameters," by S. Rodriguez-Gomez and E. DiPasquale, 9/30/90, (PB91-171298/AS).

NCEER-90-0027 "SARCF-II User's Guide - Seismic Analysis of Reinforced Concrete Frames," by S. Rodriguez-Gomez, Y.S. Chung and C. Meyer, 9/30/90, (PB91-171280/AS).

NCEER-90-0028 "Viscous Dampers: Testing, Modeling and Application in Vibration and Seismic Isolation," by N. Makris and M.C. Constantinou, 12/20/90 (PB91-190561/AS).

NCEER-90-0029 "Soil Effects on Earthquake Ground Motions in the Memphis Area," by H. Hwang, C.S. Lee, K.W. Ng and T.S. Chang, 8/2/90, (PB91-190751/AS).

NCEER-91-0001 "Proceedings from the Third Japan-U.S. Workshop on Earthquake Resistant Design of Lifeline Facilities and Countermeasures for Soil Liquefaction, December 17-19, 1990," edited by T.D. O'Rourke and M. Hamada, 2/1/91, (PB91-179259/AS).

NCEER-91-0002 "Physical Space Solutions of Non-Proportionally Damped Systems," by M. Tong, Z. Liang and G.C. Lee, 1/15/91, (PB91-179242/AS).

NCEER-91-0003 "Seismic Response of Single Piles and Pile Groups," by K. Fan and G. Gazetas, 1/10/91, (PB92-174994/AS).

NCEER-91-0004 "Damping of Structures: Part 1 - Theory of Complex Damping," by Z. Liang and G. Lee, 10/10/91.

NCEER-91-0005 "3D-BASIS - Nonlinear Dynamic Analysis of Three Dimensional Base Isolated Structures: Part II," by S. Nagarajaiah, A.M. Reinhorn and M.C. Constantinou, 2/28/91, (PB91-190553/AS).

NCEER-91-0006 "A Multidimensional Hysteretic Model for Plasticity Deforming Metals in Energy Absorbing Devices," by E.J. Graesser and F.A. Cozzarelli, 4/9/91.

NCEER-91-0007 "A Framework for Customizable Knowledge-Based Expert Systems with an Application to a KBES for Evaluating the Seismic Resistance of Existing Buildings," by E.G. Ibarra-Anaya and S.J. Fenves, 4/9/91, (PB91-210930/AS).

NCEER-91-0008 "Nonlinear Analysis of Steel Frames with Semi-Rigid Connections Using the Capacity Spectrum Method," by G.G. Deierlein, S-H. Hsieh, Y-J. Shen and J.F. Abel, 7/2/91, (PB92-113828/AS).

NCEER-91-0009 "Earthquake Education Materials for Grades K-12," by K.E.K. Ross, 4/30/91, (PB91-212142/AS).

NCEER-91-0010 "Phase Wave Velocities and Displacement Phase Differences in a Harmonically Oscillating Pile," by N. Makris and G. Gazetas, 7/8/91, (PB92-108356/AS).

NCEER-91-0011 "Dynamic Characteristics of a Full-Sized Five-Story Steel Structure and a 2/5 Model," by K.C. Chang, G.C. Yao, G.C. Lee, D.S. Hao and Y.C. Yeh," 1/2/91, to be published.

NCEER-91-0012 "Seismic Response of a 2/5 Scale Steel Structure with Added Viscoelastic Dampers," by K.C. Chang, T.T. Soong, S-T. Oh and M.L. Lai, 5/17/91 (PB92-110816/AS).

NCEER-91-0013 "Earthquake Response of Retaining Walls; Full-Scale Testing and Computational Modeling," by S. Alampalli and A-W.M. Elgamal, 6/20/91, to be published.

NCEER-91-0014 "3D-BASIS-M: Nonlinear Dynamic Analysis of Multiple Building Base Isolated Structures," by P.C. Tsopelas, S. Nagarajaiah, M.C. Constantinou and A.M. Reinhorn, 5/28/91, (PB92-113885/AS).

NCEER-91-0015 "Evaluation of SEAOC Design Requirements for Sliding Isolated Structures," by D. Theodossiou and M.C. Constantinou, 6/10/91, (PB92-114602/AS).

NCEER-91-0016 "Closed-Loop Modal Testing of a 27-Story Reinforced Concrete Flat Plate-Core Building," by H.R. Somaprasad, T. Toksoy, H. Yoshiyuki and A.E. Aktan, 7/15/91, (PB92-129980/AS).

NCEER-91-0017 "Shake Table Test of a 1/6 Scale Two-Story Lightly Reinforced Concrete Building," by A.G. El-Attar, R.N. White and P. Gergely, 2/28/91.

NCEER-91-0018 "Shake Table Test of a 1/8 Scale Three-Story Lightly Reinforced Concrete Building," by A.G. El-Attar, R.N. White and P. Gergely, 2/28/91.